EXPERIMENTAL STUDY OF THE STABILITY AND FLOW CHARACTERISTICS OF FLOATING LIQUID COLUMNS CONFINED BETWEEN ROTATING DISKS

prepared for

NATIONAL AERONAUTICS AND SPACE ADMINISTRATION

WASHINGTON, D.C.

Arthur D. Little, Inc.

EXPERIMENTAL STUDY OF THE STABILITY AND FLOW CHARACTERISTICS OF FLOATING LIQUID COLUMNS CONFINED BETWEEN ROTATING DISKS

A.A. Fowle, L. Soto, P.F. Strong, and C.A. Wang

Prepared by

ARTHUR D. LITTLE, INC.
Cambridge, Massachusetts

for

NATIONAL AERONAUTICS AND SPACE ADMINISTRATION
Washington, D.C.

Contract No. NASW-3186
ADL REF. C-82435

February 1980

Arthur D Little, Inc.

FOREWORD

This investigation was sponsored by the Office of Materials Processing in Space, National Aeronautics and Space Administration, Washington, D.C. Work was carried out and is reported in two parts. Part I reports on the investigation of the stability of floating liquid columns confined between rotating disks. Part II reports on the development of a stereoptical-tracer particle technique for measuring velocity fields within transparent fluids and its application to these floating liquid column systems.

Dr. A.A. Fowle was the Director and Principal Investigator. Ms. C.A. Wang carried out the experiments, made the observations, and reduced and organized the data of Part I. Mr. L. Soto provided the same services for the Part II investigation and, in addition, was responsible for the apparatus design and test protocol used in the measurement of flow fields. Mr. P.F. Strong was the author of the theoretical analyses of resonance in axially vibrated cylindrical columns and for predicting the location of the tracer particles from stereo photographs.

PART I

TABLE OF CONTENTS – PART I

	Page
List of Tables and Figures	viii
FOREWORD	iii
I. INTRODUCTION	1
II. SUMMARY	2
III. THEORY	4
IV. REVIEW OF PRIOR TESTS	9
V. EXPERIMENTAL INVESTIGATION	12
VI. REFERENCES	18
APPENDIX – THE PREDICTION OF THE NORMAL VIBRATIONS OF A CYLINDER OF LIQUID	47

LIST OF TABLES AND FIGURES – PART I

Table No.		Page
1	Test Conditions	19
2	Fluid Properties	20
Figure No.		
1	Unstable Shapes of Rotating Liquid Zones	21
2	Theoretical Stability Criteria for Cylindrical Column	22
3	Experimental Apparatus Used for Floating Liquid Zone Studies by Plateau Simulation	23
4	Experimental Apparatus for Liquid Floating Zone Studies on Skylab IV	24
5	Experimental Apparatus Used for Floating Zone Studies by Low Bond Number Simulation	25
6	Comparison of Experiments and Theories on the Stability of Rotating Cylindrical Liquid Columns	26
7	Schematic of Experimental Apparatus Used for Axial Vibration of Cylindrical Liquid Columns	27
8	Cylindrical Water Column – Isorotation	28
9	Cylindrical Silicone Column – Isorotation	29
10	Cylindrical Water Column – Non-Parallel End-Faces, Isorotation	30
11	Cylindrical Water Column – Equal Counterrotation	31
12	Cylindrical Silicone Column – Equal Counterrotation	32
13	Cylindrical Water Column – Non-Parallel End-Faces, Equal Counterrotation	33
14	Cylindrical Water Column – Single-End Rotation	34
15	Cylindrical Silicone Column – Single-End Rotation	35
16	Cylindrical Water Column – Non-Parallel End-Faces, Single-End Rotation	36
17	Conical Water Column – Isorotation and Co-Rotation	37
18	Conical Water Column – Isorotation and Co-Rotation	38
19	Conical Water Column – Equal and Unequal Counterrotation	39
20	Conical Water Column – Equal and Unequal Counterrotation	40
21	Conical Water Column – Bottom-End Rotation	41
22	Conical Water Column – Top-End Rotation	42
23	Shapes of Cylindrical Zones Axially-Vibrated in First Two Modes of Resonance	43
24	Axially-Vibrated Cylindrical Columns of Water	44
25	Axially-Vibrated Cylindrical Columns of Silicone	45
26	Cylindrical Water Zone in C-Mode Deformation	46

EXPERIMENTAL STUDY OF THE STABILITY AND FLOW CHARACTERISTICS OF FLOATING LIQUID COLUMNS CONFINED BETWEEN ROTATING DISKS

ABSTRACT — Part I

A low Bond number simulation technique was used in conducting a number of experiments to establish the stability limits of cylindrical and conical floating liquid columns under conditions of isorotation, equal counter-rotation, rotation of one-end only, and parallel-axis offset. Tests which establish the conditions for resonance in cylindrical liquid columns perturbed by axial, sinusoidal vibration of one end-face are also reported. All tests were carried out under isothermal conditions with water and silicone fluids of various viscosities.

With few exceptions, test data for rotating columns show that the onset of instability is in the C-mode and is correlated very well by a theoretical prediction based on isorotation. The onset of instability for a cylindrical column of silicone fluid having a viscosity 100 times that of water under equal counter-rotation and single end-rotation is in the first axisymmetric mode. An explanation for the rather surprisingly simple C-mode correlation is provided by the results of flow visualization studies. The data on the resonance of cylindrical columns are correlated very well by a prediction based on a newly developed theory.

I. INTRODUCTION

The near-zero gravity environment of an orbiting space station offers unique opportunities for improving the process of growing crystals in high-temperature, floating molten zones. In such an environment, buoyancy-induced convection, which is difficult to predict and control, is greatly reduced, and constraints imposed by gravity on the dimensions of a floating zone are relieved. As the allowable stable length of a molten zone in a microgravity environment is greater than that on Earth, the problem of producing a temperature field within the melt that minimizes compositional variations and residual stresses in the growing crystal is eased.

Rotating the crystal and feedstock is a common way of effecting in-depth heating of the melt zone via forced convection currents and of reducing the azimuthal temperature gradients that would exist in its absence. Although rotation may be used to advantage to induce convective heat transport to the inner regions of the melt, unwanted temporal and spatial flow variations may occur, depending on the speed of rotation, and an upper speed limit is set by its stability.

As a general rule, then, in growing single crystals by the float-zone method, one may wish to employ rotation and the largest possible length-to-diameter ratio of the molten zone. The limits of possible length-to-diameter ratios and rotational rates are set by the stability of the liquid zone. Resonances due to vibrational disturbances are to be avoided also. It is within these limits that geometric and rotational variations are sought to produce crystals approaching perfection.

II. SUMMARY

A review of the literature containing information useful in determining the stability of liquid columns having geometries and operating under conditions typical of the classical float-zone, crystal-growing method is presented in this report. In addition, the test methods and the results of a number of experiments conducted to establish the stability limits of floating liquid columns of cylindrical and conical geometry under conditions of isorotation, equal counterrotation, rotation of one end-face only, and parallel axis offset are given. Investigation of the conditions for resonance in cylindrical liquid columns perturbed by axial, sinusoidal vibration of one end-face is also reported.

All experiments were carried out under isothermal conditions and employed liquid columns of small dimensions to make the Bond numbers appropriate to each liquid zone of the order one. Both distilled water and silicone oil of various viscosities were employed as test fluids.

The theories that have been advanced to predict the stability of the columns in various modes of excitation are presented in Section III, and predictions based on these theories are compared with the results of the experiments completed under this contract and with those published previously. In addition, a new theory has been developed to correlate the results of tests leading to resonance modes of cylindrical liquid columns under normal vibration.

In all but a few tests employing rotation, it was observed that the columns first encountered instability in the C-mode. This result was consistent with theoretical arguments which predicted that this was the most unstable mode, that is, it occurred at the lowest rotational speed for a given column geometry, but the rather surprising result was that these tests were correlated extremely well by the theoretical expressions derived for conical and cylindrical columns for the case of isorotation. This was true regardless of the type of rotation, offset, or magnitude of viscosity in the range of 1 to 10 centistokes. In some cases, the columns survived the first C-mode only to enter and fail in a second C-mode at a higher driving speed.

Flow visualization studies provided some insight into this result, if not a full understanding of it, up to the point of the onset of the first C-mode instability. For the equal counterrotational and single-end rotational cases, the typical Proudman-Taylor cellular structure persisted (modified by the appearance of surface vortices for the case of equal counterrotation at sufficiently high rotational speeds) up to incipient instability. At slightly higher rotational speeds, orbiting of the column commenced. The orbiting circumstance was induced when the rotational speed of either end-face corresponded to the Rayleigh condition of equality between the change in kinetic energy of the column in orbit and the change in potential energy due to surface distortion. This condition apparently prevailed irrespective of the circulation within the columns at incipient instability; that is, the superposition of fluid force effects held.

The exceptions to the onset of instability in the C-mode involved tests of cylindrical columns of 100-centistoke silicone under conditions of equal counterrotation and rotation of one end only. Here the C-mode was not observed and the columns first distorted and failed in their first axisymmetric instability mode. It was only in tests involving a viscosity 100 times that of water that this effect on stability became noteworthy and it acted to increase the stable range.

Agreement between the theory developed to predict the natural frequencies of cylindrical columns of water and 1-centistoke silicone under normal vibration and test results proved to be good. The natural frequencies of columns of silicone having viscosities of 10 and 100 centistokes were not evident, the system apparently being overcritically damped or sufficiently damped to avoid the observation of resonance.

III. THEORY

General

The system whose limits of stability are sought is an isothermal liquid column suspended between two rotating disks. It is characterized by low Bond numbers; that is, the dimensions of the liquid columns are made small to minimize the effects of gravity compared to capillary effects, thus simulating a microgravity environment. In the simplest configuration, the column is a right circular cylinder having a diameter equal to that of the end-disks, and the planes of the disks are perpendicular to their axes of rotation which are collinear.

Upon rotation of the disks, shear forces are generated at the end-faces of a column of viscous liquid which, in turn, induce circulation within the column. The surface of the column distorts in response to this circulation in an attempt to contain it. In general, the distorted shape of the column has a larger area and, hence, larger surface energy. Moreover, a constraint on the distorted shape of a stable column is set by continuity; that is, the volume of the distorted column must equal that of the undistorted column. The column is contained at rotational rates up to the limit where the change in the kinetic energy of the fluid equals the increase in potential energy represented by the increase in the product of the surface area and surface tension coefficient. At higher rotation rates the column becomes unstable and may fly apart.

Looked at from the standpoint of a force balance, the surface will distort such that its curvature divided into the surface tension coefficient of the liquid will equal the discontinuous pressure difference across the surface every place on the surface in order for stability to be maintained. In the general case, the flow field within the column is complex, and the curvature of the steamlines in both axial and radial planes contributes to the pressure at the surface. However, in most cases of interest, the tangential components give rise to the dominant centripetal forces which must be balanced by the surface tension forces. As these centripetal forces are proportional to the square of the angular velocities of the circulating liquid, a limit on the allowable angular velocities of the end-faces exists wherein the distortion of a given column can provide the surface tension force required to contain in the liquid and still meet continuity requirements.

Another form of instability arises when disturbances to the column give rise to capillary waves on the surface. The amplitude of these waves is enhanced at resonance modes having frequencies occurring when the column length corresponds to an integer number of half-wave lengths of the capillary wave.

Resonances occurring due to normal vibration of the end-faces represent another circumstance of interest. The conditions to be met by resonant modes are that the volume of the fluid in the distorted column be constant and that the change in surface energy and the change in kinetic energy of the fluid volume be equal.

The application of dimensional analyses provides insight into the form of the solutions to the stability problems under investigation. Equation (1) represents the general form of all

solutions under the conditions postulated and where, in addition, viscous forces are insignificant. This equation follows from application of standard procedures of dimensional analysis:

$$\frac{\sigma}{\rho a_1^3 \omega_1^2} \geq f\left(\frac{\ell}{a_1}, \frac{\omega_1}{\omega_2}, \frac{a_1}{a_2}\right) \qquad (1)$$

where

σ = surface tension coefficient of the liquid in its surroundings (dyne/cm),
ρ = density of the liquid (g/cm^3),
ω_1 = angular velocity of disk at one end-face (rad/sec),
ω_2 = angular velocity of disk at other end-face (rad/sec),
ℓ = length of liquid column (cm),
a_1 = radius of liquid column at one end-face (cm), and
a_2 = radius of liquid column at the other end-face (cm).

The term $\frac{\sigma}{\rho a^3 \omega_1^2}$ represents the ratio of surface tension to inertia forces, and is the inverse of the Weber number. The physical reasoning cited above provides the basis of the inequality sign for stability. The equal sign sets the stability limit.

In any real system, deviations from the ideal geometry are present, depending on the precision of the construction of the assembly. The axes of rotation may be parallel but not collinear (offset), or the axes may be non-parallel. In either case, the end-faces may not be precisely perpendicular to the rotational axes. In principle, these dimensional variables enter as additional dimensionless indices in Equation (1).

The theories that have been published do not give solutions for stability in the general case of a cylindrical liquid column under eccentric or non-parallel conditions, or even to Equation (1), when ω_1 and ω_2 differ in magnitude and sign. However, solutions of simpler cases which provide guidance to the design and operational parameters necessary for stable behavior do exist. Fortunately, in most cases, practical designs can reduce the effects of machine tolerance to insignificance, as will be demonstrated by test results to be presented. The results of analyses pertinent to the major instability problems of practical interest are presented in the following paragraphs.

C-Mode Instability

Figure 1a shows the configuration of a distorted liquid column excited in its lowest order "C" mode. The C-mode is descriptive of its distorted shape. For steady-state conditions, where the end-faces are isorotational, the column rotates as a solid body. In the ideal case of no eccentricity and parallel end-faces, the lowest order condition for stability, as developed in Reference 1, is given by

$$\phi_C = \frac{\sigma}{\rho a^3 \omega^2} \geq \left(\frac{\ell}{\pi a}\right)^2 \qquad (2)$$

As before, the equal sign substitutes for the inequality sign at the stability limit.

The criterion represented by Equation (2) is plotted in Figure 2. Stable conditions of operation are those represented by the region above and to the left of the line, ϕ_C. Unstable conditions are represented in the region below and to the right of this line.

Equation (2) establishes the maximum rotation rate for a column of given geometry; i.e., a right circular cylinder for stable operation under isorotational conditions. In many cases of interest the assumed conditions may not be present. The effect of some variations of practical interest as determined by experiment will be presented in a following section.

An approximate expression for the C-mode instability for a conical zone in isorotation is:

$$\frac{\sigma}{\rho a_2^3 \omega^2} > \left[\frac{0.572\alpha^2 + 0.856\alpha + 0.572}{(\alpha + 1)}\right] \left(\frac{\ell}{\pi a_2}\right)^2 \qquad (3)$$

where

α = a_1/a_2,
a_1 = radius of smaller end of conical zone, and
a_2 = radius of larger end of conical zone.

This expression was derived in a manner similar to that described in Reference 1 for application to the case of a cylindrical zone. The maximum value of the bracketed term is 1.0 and occurs for a value of a_2/a_1 equal to unity. Therefore, the least stable configuration is a cylinder of radius a_2. The cone is increasing in stability as α becomes smaller, with the minimum value of the bracketed term approaching 0.572 as α approaches zero. Moreover, Equation (3) predicts that the stability of the cone is intermediate between a cylinder of radius a_1 and a_2, but nearer that of the larger cylinder.

Axisymmetrical Mode Instability

Figure 1b illustrates the distorted shape of the column excited in its lowest order axisymmetrical mode. Hocking[2] derives the stability criteria for this case from an analysis of infinitely long liquid columns rotating as a solid body and subjected to axisymmetric longitudinal disturbances of small amplitude induced by centripetal forces with the result:

$$\phi_{xs} = \frac{\sigma}{\rho a^3 \omega^2} \geq \frac{1}{\kappa^2 - 1} \qquad (4)$$

where

$$\kappa = \frac{2\pi a}{\lambda} = \frac{2\pi a n}{\ell},$$

a = radius, and
λ = wavelength of disturbance.

In the case of columns of finite length, ℓ, the instability disturbance must be a standing wave which does not alter its volume so that the wavelength must meet the condition $\pi\lambda = n\ell$, where n is an integer. Therefore, the lowest order condition for stability becomes, for n = 1:

$$\phi_{xs} = \frac{\sigma}{\rho a^3 \omega^2} \geq \frac{\left(\frac{\ell}{a}\right)^2}{4\pi^2 - \left(\frac{\ell}{a}\right)^2} \tag{5}$$

This criterion establishes the maximum rotation rate for a cylindrical column for stable operation under the conditions assumed, and it is illustrated in the curve of Figure 2. Coriell et al.[3] have analyzed the case of a cylindrical and conical column, including the effects of gravity, variant volume, and isorotation. The solution requires machine computation and the results of only a few cases have been published. Again, in many cases of interest, the condition of isorotation may not be imposed.

Capillary Wave Resonance

The generation of longitudinal capillary waves on the surface of a cylindrical column have resonant standing wave modes correlated by:

$$\phi_{cw} = \frac{\sigma}{a^3 \omega^2} = 2\left(\frac{\ell}{n\pi a}\right)^3 \tag{6}$$

or, in simpler form

$$\phi_{cw} = \frac{\sigma}{\ell^3 \omega^2} = \frac{2}{n^3 \pi^3}$$

Equation (6) represents the simplest version of the many standing wave modes that are possibly generated by a variety of disturbances. Here n is the number of half wavelengths in the distorted length ℓ and can take on values 2,3,4, . . . etc., corresponding to successively higher modes of resonance. A value of n equal to unity is excluded because it violates the condition of continuity of volume. Equation (6) with n set equal to 2, corresponding to the first natural frequency, is shown as a curve in Figure 2.

The capillary wave resonances do not involve rotation and consequence centripetal forces as a fundamental ingredient, thereby differing from the C-type and axisymmetric modes. Lamb[4] gives a classical discussion of the physical characteristics of capillary waves.

Column Resonance under Axial Vibration

The resonant frequencies of axially vibrated cylindrical columns have been predicted on the basis of a theoretical analysis developed in the Appendix. At resonance, the free surface is distorted by a standing wave containing an integer number of half wavelengths, n, in the

length, ℓ . A value of n equal to unity is excluded because it violates constraints set by the continuity of the distorted volume. For even values of n, the resonant modes are correlated by

$$\phi_{av} = \frac{\sigma}{\rho \ell^3 \omega^2} = u(p) \quad \frac{1}{n^3 \pi^3} \tag{7}$$

For odd values of n, the resonances are given by

$$\phi_{av} = \frac{\sigma}{\rho \ell^3 \omega^2} = v(p) \quad \frac{1}{n^3 \pi^3} \tag{8}$$

The expressions u(p) and v(p) are rather complex functions of $p = n\pi\alpha/\ell$ (involving Bessel functions) given in the Appendix.

Summary

The theory relating to the instability of cylindrical columns of liquid is extracted from a selection of those that appear in the literature. The scope of the survey has been established by its purpose which is to give guidance to the prediction and interpretation of instability phenomena occurring in systems of practical significance in crystal-growth processes carried out in a microgravity environment. The theoretical equations for the first C-mode [Equation (2)], axisymmetric mode [Equation (5)], and capillary wave [Equation (6)] instabilities are shown as curves on Figure 2. An obvious observation to be drawn from Figure 2 is that the C-mode instability is expected to be the first encountered (the most unstable), and systems designed to avoid this instability should, *a priori*, avoid the others. The theory developed for the natural frequencies of an axially vibrated cylindrical zone is believed to be original. In the following sections, experimental results are presented which test the validity of the stability theories given and their value as design criteria.

IV. REVIEW OF PRIOR TESTS

General

In this section, results of stability tests taken from three sources in the literature are reviewed and compared with the theories given previously. These sources are: the work of Carruthers and Grasso,[5] the experiments conducted in Skylab IV,[6] and the tests of Fowle et al.[11]

Experiments Using Plateau Simulation

Carruthers and Grasso used the Plateau method to investigate the stability of liquid columns. Their apparatus consisted of a vertical column of a mixture of water and ethanol suspended between vertical, rotatable end-support tubes immersed in mineral oil (Nujol) with which it is immiscible. The end-support tubes were hollow to facilitate the deployment of the columns. The composition of the vertical column was adjusted in density to equal that of the Nujol surroundings as close as practically possible to simulate operation at microgravity conditions. This apparatus is shown in Figure 3.

In this work, the investigators studied and reported on column stability under various rotational conditions with end-support tubes of equal diameter and different diameters (conical zones). The results of tests on the stability of spherical liquid zones, as well as flow visualization studies on cylindrical columns using dye tracers, were also reported.

In the tests on conical and cylindrical columns, isorotational conditions were imposed. The axisymmetric mode of instability was observed and correlated with Equation (5) for n in a range $1 \leq n \leq 2$ for cylindrical zones. Conical zones, formed by using tubes with unequal end-diameters, were also tested under co-rotation conditions. Results indicated that the onset of the axisymmetric instability occurred as if the conical zone behaved as a cylindrical zone, with the limit correlating with the diameter and speed corresponding to the end-face, resulting in the first appearing instability.

The Nujol surroundings suppressed the C-mode instability and prevented solid-body rotation within the zone, even under isorotational conditions, because the boundary conditions on the column were different from those of a column in the relatively inviscid surroundings common to float-zone crystal operations. The authors also reported an important influence on the tube boundary conditions, whether open or closed, for their Plateau method experiments.

Skylab IV Experiments

The apparatus used in the Skylab IV tests is illustrated in Figure 4. Liquid zones of water, water plus dye, soap solution, and soap foam were deployed between two aligned circular disks which were rotated in isorotation, equal counter-rotation, and single disk rotation only. This apparatus made ingenious use of the dedicated time of the astronaut and the limited equipment that were available.

The experiments were carried out in a microgravity environment in the range of 10^{-5} g, and direct visualization and camera observation of a columnar system with a scale in the order of centimeters were possible. The system was limited as regards the precision of its geometry, the control of rotational rates, the ability to determine the rotational rates of the fluid zone in the axisymmetric instability mode, and the time available in one operational sequence to reach steady state.

All the instability modes discussed in Section II — C-mode, axisymmetric, and capillary wave — were observed in the Skylab experiments. The axisymmetric modes were observed to be dominant under conditions when only one disk was rotated. The generation of these modes took place within a transient period, and no equipment was available to measure zone rotational rates. The rotational rates were estimated by equations based on the rate of transfer of momentum by shear forces along the axis of the fluid column. These estimates were only approximate. Nevertheless, the correlation with Equation (4) using the estimated zone rotational rate was good for engineering purposes.

The C-mode instability was observed to be dominant for ratios of ℓ/a in the range of 3 to 5, for both isorotation and equal counterrotation of the end-disks. The C-mode instability was not observed at an ℓ/a ratio of about 1.5. The observation of the C-mode instability was necessarily made under transient conditions only; however, because of its asymmetric nature, the zone rotation rate was clearly measurable.

No marked consistent differences in the instability limits attributable to the mode of rotation, no matter whether water-dye, soap solution, or soap foams were used, could be identified within the limits of these experiments. The C-mode instability was correlated using an analytical expression since determined to be in error.

Capillary waves were observed to be a dominant feature for an ℓ/a ratio near 1.5 for both isorotation and equal counter-rotation conditions. Again, observations were necessarily made under transient conditions. Correlation of the rotational rates at which capillary waves were observed with a theoretical prediction of first natural frequencies was made. However, the theoretical expression used for the comparisons has since been determined to be in error.

Experiments Using Low Bond Number Simulation

Fowle et al.[1] used a liquid column of small geometric scale to simulate stability conditions attendant to operation in a low-gravity environment. Figure 5 illustrates schematically the experimental apparatus used. The rotation of the end-faces of the column could be controlled and measured in magnitude and direction with precision, as well as the rotational rate of an unstable fluid zone. The length of the column and the offset of the parallel axes were controlled and measured by micrometer adjustments. The apparatus of Figure 5 was also built to accommodate flow visualization studies, hence its offset construction.

This test set-up had the advantages of duplicating the boundary conditions common to a true floating zone and the ability to control and measure system conditions with a relatively high degree of precision. Its main disadvantage was the fact that gravity forces were not negligible in respect to surface tension forces. The influence of gravity forces were tolerable in that they were

perpendicular to the centripetal forces, driving both the C-mode and axisymmetric mode of instability. The experiments were conducted at Bond numbers, $\rho g a \ell/\sigma$, in a range between 0.61 and 2.26.

Distilled water was suspended vertically between rods having parallel axes of rotation and end-faces perpendicular to these axes. The column was produced by introducing water from a hypodermic syringe in amounts which resulted in a shape approximating a right circular cylinder. The shape actually produced could be likened to a pear truncated at top and bottom, adjusted such that the cylindrical surface of the fluid column was tangent to the support rod at the top. The distortion from a true cylinder was due to gravity forces and, in degree, dependent on the length-to-diameter ratio of the column, with the shape approaching a cylinder at smaller ℓ/a ratios.

Tests under isorotational conditions were made. Only the C-mode instability was observed. The agreement between test results and the prediction of this instability limit by Equation (2, was excellent.

Summary

Experimental data from the reviewed literature have been organized in accordance with Equation (1) and are displayed in Figure 6. The theoretical equations for the first C-mode [Equation (2)], axisymmetric mode [Equation (5)], and capillary wave [Equation (6)] instabilities are shown as curves on this figure.

From this display it should be noted that the data from Reference 1 agree very well with the theoretical prediction of first occurring instability in the C-mode. The data of Reference 6 pertaining to isorotation also show tolerable agreement with this prediction, and the differences may well be due to the difficulties encountered in obtaining precise data under the circumstances of the Skylab tests. The Skylab tests for conditions of single-end rotation similarly show tolerable agreement with theory, and the differences may be similarly explained. It is also of interest to note here that the C-mode was not the first occurring instability observed in the case of single-end rotation.

The experimental data of Reference 5 do not agree well with the theoretical predictions of the first axisymmetric instability mode which was observed. This disparity is believed to be due to the presence of shear on the "free" surface of the rotating column imposed by the Nujol surroundings used in the Plateau simulation of zero gravity where the actual and theoretically assumed boundary condition is nearly shearless.

V. EXPERIMENTAL INVESTIGATION

Description of Experiments

Summary

The experimental apparatus and techniques reported in Reference 1 have been extended to investigate stability under a wider variety of conditions. These include equal counter-rotation of the end-faces, rotation of one end-face only, as well as rotation under conditions where the parallel axes are offset. Water and silicone fluids with viscosities ranging from 1 to 100 centistokes were used to determine the effects of viscosity on stability, if any. Cylindrical zones whose end-faces were not parallel were investigated for all of the above mentioned conditions of rotation. The stability of liquid zones of a conical geometry was investigated also. Finally, using a simple apparatus constructed for the purpose, cylindrical floating zones of water and silicone fluid were disturbed by the axial vibration of one end-face to determine conditions for resonance. A summary of the conditions tested is given in Table 1 while Table 2 summarizes the fluid properties used in the reduction of the experimental data. Further details regarding each type of experiment follow.

Rotation of Cylindrical and Conical Zones

The experimental apparatus (previously described in Section IV) used to determine the limits of stability of liquid columns for various conditions of rotation is shown schematically in Figure 5. Improvements in the experimental apparatus and technique previously used were implemented to enhance the accuracy and reduce the scatter of measured data.

In early runs, different degrees of wetting at the end-faces were observed. The wetting was caused by machine-made grooves in the surfaces of the Lucite rods. This problem was eliminated by lapping the end-faces against each other. Thereafter, liquid columns were produced with well-defined contact lines fixed by the edges of the end-faces of the Lucite rods.

Preliminary tests also showed that stability limits were influenced by the volume of liquid between the end-faces for a given spacing. Early failure (at lower rotational speeds) occurred for liquid zones whose volume was somewhat greater than that equal to a right circular cylinder, and extended stability was observed for liquid zones whose volume was somewhat less than this geometry. To minimize the scatter of data due to the uncertainty in the volume of the liquid zone, a micrometer syringe was used to inject the volume of liquid equal to that for a right circular cylinder with an accuracy estimated to be within 5%. Also to minimize the volume changes associated with evaporation of the liquid water zones, the zone was enclosed in a Lucite cell which contained a reservoir of water at its bottom. Finally, in an attempt to minimize the effect of contaminants on the surface tension of the liquids used, the end-faces were cleaned with copious amounts of propanol before the liquid zone was formed.

Cylindrical Zones — Liquid zones were formed with distilled water and Dow Corning 200 series silicone fluids. The viscosities of the silicone fluids were 1, 10, and 100 centistokes. The radius of the cylindrical liquid water zones was 0.4 cm and the length varied to give Bond numbers, $\rho g a l/\sigma$, in the range of 0.68 to 2.05. To achieve comparable Bond numbers for the silicone fluid zones (whose surface tension is about one-third that of water), the radius of the

cylindrical zone was reduced to 0.131 cm, giving Bond numbers in the range of 0.92 to 1.8. The Lucite rods were coated with an antimigration fluorocarbon resin (Minnesota Mining and Manufacturing's FC-721) to prevent the silicone fluids from creeping up along their sides.

The effect of offset on stability was investigated for the water zones. The parallel axes of rotation were offset by 0.05 cm, corresponding to a 20% radial offset.

To investigate the effect of non-parallel end-faces, a plexiglass disk, 0.254 cm radius and with one inclined face, was glued to the end-face of the bottom support rod. The normal to the non-parallel end-face was inclined 2.86 degrees to the axis of rotation. Distilled water was used in tests with non-parallel end-faces. The length of the column was varied to give Bond numbers in a range of 0.86 to 2.05.

Conical Zones — Conical liquid zones were formed by injecting distilled water in amounts equal to the appropriate theoretical volumes between the support rods whose end-faces had different diameters. The diameter of the bottom end-face was kept constant, $2a_2 = 0.507$ cm, and two diameters of the top end-face were used: $2a_1 = 0.165$ cm and $2a_1 = 0.254$ cm. The bottom-end-to-top-end radii ratios were, therefore, 3.07 and 2.0 for the two cases. Means for offset and non-parallel end-faces were also incorporated in the tests on conical zones.

Vibration

In addition to investigating the stability criteria for rotating liquid columns, cylindrical liquid columns were vibrated axially so that free-surface oscillations and resonant frequencies could be observed. The experimental apparatus which was used is shown schematically in Figure 7. The bottom support rod was positioned along the axis of the sonic vibrator, and the top support rod was rigid and coaxial. The support rods were made of machined brass or stainless-steel.

Distilled water or silicone fluid, 1 centistoke only, was injected between the two end-faces through a micrometer syringe in a volume appropriate to a right circular cylinder. To minimize volume changes due to evaporation, a water-filled Lucite cell enclosed the liquid water column and support rods as before. The axial vibrations were generated and controlled by a Hewlett-Packard wide-range oscillator and by a Krohn-Hite amplifier. The zone was observed in both full illumination and by stroboscopic lighting through a low-power binocular microscope.

A range of length-to-radius ratios of about 1 to 4 were investigated. The length of the zone was controlled by movement of the top support rod by a screw adjustment. Tests with cylindrical liquid zones of different radii were made to determine the dependence of resonant frequencies on the radius. For water, end-faces having three different radii were used: 0.666, 0.127, and 0.248 cm. For tests with silicone, the radii of the end-faces were 0.652, and 0.131 cm. The full amplitude of the vertical displacement of the driven end-face could be controlled and was kept in the range of 40-70 μm at all frequencies. The vertical displacement of the vibrating end-face was not altered by the present of the liquid zone.

Results

Rotation of Cylindrical and Conical Zones

The experimental data on the stability limits observed for cylindrical and conical liquid zones driven by their end-faces in various types of rotation have been reduced to the dimension-

less stability parameter, $\sigma/\rho a^3\omega^2$, and have been plotted as a function of ℓ/a in Figures 8 through 22. The theoretical prediction for the lowest order of instability, the first C-mode, is also illustrated in these figures.

Isorotation of Cylindrical Zones — The experimental results for the isorotation of cylindrical liquid zones of water and silicone fluid with and without offset are given in Figures 8, 9, and 10. As indicated, in all cases the first occurring instability was the C-mode and the test data are correlated very well by the theoretical prediction of Equation (2) (see curve ϕ_C). The lower limit of stability demonstrated by columns having length-to-radius ratios greater than 2 is probably due to the alteration of the shape of the stable column by gravity. The decreased stability of the longer columns is a common feature of all tests, regardless of the rotational circumstance.

On the whole, the first occurrence of instability was unaffected by offset isorotation, even though the radial offset was 20% ℓ. In some cases of offset rotation, however, the column survived the 1st C-mode distortion. As the rotation rate was increased beyond that of the first C-mode, the column returned to its cylindrical shape, but continued to rotate near to, but slower than, the frequency of this first mode. At some still higher speed of the end-faces, a second C-mode distortion occurred which resulted in the break-up of the column. The rotation rate of the support rods at which the second C-mode occurred was about 1.4 times that of the first C-mode, and the zone rotation rate at the second C-mode instability was one-half that of the end-faces.

The results of tests using silicone fluids having viscosities of 1, 10, and 100 centistokes are given in Figure 9. The results show that the first occurring dimensionless stability limits for the viscous fluids were only about 10% ℓ greater than those obtained for the water zones having comparable Bond numbers.

The effect of non-parallel end-faces on the stability of water columns in isorotation is illustrated in Figure 10. Non-parallelism, with or without offset, apparently has little influence on the occurrence of the first C-mode. However, the column never survived the first C-mode for rotation under these circumstances.

Equal Counter-rotation of Cylindrical Zones — The demonstrated instability of cylindrical zones of water and silicone, with and without offset and non-parallel end-faces, when acted upon by end-faces in equal counter-rotation, are illustrated in Figures 11, 12, and 13. In all cases, except one, the onset of instability is correlated very well by Equation (2) which was derived for the case of isorotation. An explanation of this rather surprising result is that the column, when rotated at speeds approaching that of the first C-mode, "locks-on" to one end-face and the zone rotates at the speed of this end-face, thereby duplicating closely its behavior in isorotation. This behavior was revealed by flow visualization studies which are described in more detail in a following section.

It should be noted that the stability of the column with counter-rotation of the end-faces is very similar to that with isorotation, including the relatively minor influences of offset and nonparallelism of the end-faces, although the ability of the column to survive the first C-mode was somewhat enhanced. Viscosity in the range of 1 to 10 centistokes has a minor influence on results, but at 100 centistokes, no C-mode distortion was observed The single point at 100 centistokes, shown in Figure 12, represented distortion and failure in the first axisymmetric (bottle-shaped) mode. The theoretical prediction for this mode is shown as a curve, ϕ_{xs}, in Figure 12.

Single-end Rotation of Cylindrical Zones — Test results on the stability of cylindrical zones of water and silicone, with and without offset and non-parallel end-faces, when driven by the rotation of one end face only, is illustrated in Figures 14, 15, and 16. Again, in all cases except those involving the use of 100-centistoke silicone, the onset of instability is in the C-mode and results are correlated very well by Equation (2).

The stability of the columns with single-end rotation proved to be very similar to those driven in isorotation or counter-rotation. The reason for this result was revealed by flow visualization. The column was shown to rotate pretty much as a solid body at the speed of the rotating end-face. Therefore, its first mode of instability was very nearly identical to that of a zone driven in isorotation. The relatively minor effects of viscosity (in the range of 1 to 10 centistokes), offset, and non-parallelism were again demonstrated. The somewhat enhanced ability of the columns to survive the first C-mode was similar to its behavior when driven by equal counter-rotating end-faces. The observation of the absence of the C-mode and of the oneset of instability and failure in the first axisymmetric mode for tests made with 100-centistoke silicone fluid was also similar.

This result is in variance with that observed in the Skylab tests[9] where the onset of instability under similar conditions was in the first axisymmetric mode (see Figure 6). The reason for this significant difference is not clear. However, it is noted that the Skylab tests were not carried out in steady state, and it may be that the system was rapidly accelerated through the 1st C-mode without failure which these tests show to be entirely possible.

Isorotation and Corotation of Conical Zones — The results of tests on conical water columns with isorotation and corotation of the end-faces are shown in Figures 17 and 18. With isorotation, the column failed at the first C-mode at a speed corresponding to the first critical based on the large end-face (bottom end). The results are correlated better by Equation (2) than by Equation (3); that is, the conical zones behaved as if they were a cylinder having the diameter of the larger end. The increased degree of stability predicted by Equation (3) did not manifest itself. The results of a few tests in which the rotating axes were offset do not alter this picture.

In corotation with a larger end-face rotating at a speed well below that corresponding to the first critical speed, the column was observed to distort in the C-mode when the speed of the smaller end-face (top end) reached the first critical speed corresponding to the larger end, but it did not fail. The column returned to its normal shape with increasing top-end speed up to the limit of the rotary speed of the motor, even though this speed might have been greater than the critical speed corresponding to a cylinder having the diameter of the top-end.

In corotation, with the larger end rotating at a speed relatively close (say, within 75%) to the first critical corresponding to this end, the first onset of stability could occur when the speed of the smaller end exceeded this critical. The zone rotation under these circumstances had a frequency intermediate between the speeds of the two ends above, but not far from, the first critical observed in the case of isorotation.

Equal and Unequal Counter-rotation of Conical Zones — The results of tests to demonstrate the stability of conical liquid zones when driven by end-faces in equal and unequal counter-rotation are shown in Figures 19 and 20. Water was used in these tests. The results were remarkably similar to those of isorotation and corotation, which suggests that the zone rotated

much as a solid body attached to the larger end when the speed of the larger end approached its first critical C-mode. Again, results correlate well with Equation (2).

Single-end Rotation of Conical Zones — Results of tests on the stability of conical zones of water with rotation of the larger (bottom) end-face and smaller (top) end-face are illustrated in Figures 21 and 22, respectively. With larger end rotation, the column behaves as it did in isorotation. When the column was driven by the smaller end, its stability limit was set by the first C-mode based on the larger end. Also, the column was a little more stable when driven by the smaller end. The onset of instability was a bit delayed and the column distorted, but did not fail as the speed was increased through this first critical. However, these differences were not very significant and the results are correlated well by Equation (2).

Axial Vibration of Cylindrical Zones

Resonant frequencies of axially vibrated liquid columns were observed as standing waves on the free surface. Observation under stroboscopic lighting revealed that there were several modes of resonance of increasing natural frequency. At resonance, the length of the free surface distorted to form a standing wave having an integer number of half wavelengths, with the exception of 1.0, which circumstance cannot meet the continuity of volume requirement. The shapes of the liquid zone for the first two modes are shown in the photographs of Figure 23.

The results of all data taken with water and a silicone fluid having a viscosity of 1 centistoke are shown plotted in Figures 24 and 25, respectively. The resonances were not obvious when silicone having viscosities of 10 and 100 centistokes were used. The data are plotted in accordance with the correlations suggested by the theories developed in the Appendix, and curves representing the theoretical predictions are superimposed.

The comparison between experiment and theory is, on the whole, useful if not precise. The differences, particularly in the case of the odd number modes, may well be attributable, in part, to the appreciable amplitude of the perturbation that was applied where the theory assumed an infinitesimal disturbance. The disparity may also be, in part, due to the influence of gravity, which plays a larger role in the cases involving the larger ℓ/a ratios. Nevertheless, the differences are not large when viewed from an engineering perspective, and the forms of the functions u(p) and v(p) are in good agreement with the observations.

Visual Observations

Method

As previously stated, the onset of instability was determined by visual observation of the shape of the liquid zones. These shapes were made evident by illumination from either a high-intensity, tungsten-halogen, incandescent lamp or a stroboscopic, xenon-flash light source. Figure 26a shows the distortion of the zone in the first C-mode and Figure 26b shows its shape just prior to failure.

A limited number of tests were also made to identify the circulation patterns within the liquid zones as they were rotated in the approach to their stability limits in order to provide better insight into the physical reasons for the observed results. For this purpose, nickel plated, hollow

glass spheres, 5 to 50 μm in diameter, were introduced into the column. These spheres were previously screened for neutral buoyancy by letting them settle in a column of water. All flow visualization tests were made on a cylindrical water column 0.254 cm in radius and 0.510 cm high. The motion of the tracer particles were observed with scattered light from a dark-field illumination system. The flow patterns in the liquid columns were observed under conditions of isorotation, counter-rotation, and single-end rotation.

Results

When the column was driven in isorotation it behaved like a solid body as expected. The tracer particles were observed to whirl in rings with no evident radial or axial velocity component. When the water column was rotated in equal counter-rotation at frequencies low in respect to the first C-mode critical, two Proudman-Taylor cells were generated, one on each side of an intermediate axial plane. As the rotational rate was increased, the bottom cell became larger, no doubt because of the influence of gravity on the shape of the zone. At all rotational speeds, the flow spiralled toward the disks in a central core, then spiralled radially outward at the end-faces, thence spiralled away from the disks in an annular layer next to the free surface, and completed the circuit by spiralling radially inward at an intermediate layer. The reversal of the tangential velocity component was accommodated in a relatively thin Ekman layer in an intermediate plane between the end-faces.

Another interesting feature of the circulating flow was also seen. At about 200 rpm, two or three vortex swirls, with radial vortex lines, appeared on the free surface at the joining region of the two Proudman-Taylor cells. These have been reported previously in Reference 1. These vortices moved upward to the top end as the speed was increased. Their centers moved in the direction of the top end-face with some small relative tangential velocity.

With single-end rotation approaching the critical speed, the bulk fluid circulated with a large Proudman-Taylor cell associated with the rotary speed of the driving end-face. Again the flow spiralled down the central core away from the rotating end and returned in a spiral path in an annular zone next to the free surface. No surface swirls were seen for this type of rotational drive. The radial inflow and the reversal of the tangential component of velocity took place in an Ekman layer next to the stationary end-face.

In all cases of single-end or counterrotation, the orbiting circumstance of the first C-mode was induced when the rotational speed of either end-face corresponded to the Rayleigh condition of equality between the change in kinetic energy of the column in orbit and the change in potential energy due to surface distortion.

VI. REFERENCES

1. Fowle, A.A., et al., "Float-Zone Processing in a Weightless Environment," NASA CR-2768, November 1976.

2. Hocking, L.M., "The Stability of a Rigidly Rotating Column of Liquid," Mathematika, Vol. 7, Part 1, June 1960.

3. Coriell, S.R., et al., "Stability of Liquid Zones," Journal of Colloid and Interface Science, Vol. 60, No. 1, June 1977.

4. Lamb, Sir H., *Hydrodynamics*, 6th Ed., Dover Publications, N.Y., 1945, p. 597.

5. Carruthers, J.R., and Grasso, M., "Studies of Floating Liquid Zones in Simulated Zero Gravity," Journal of Applied Physics, Vol. 43, No. 2, February 1972.

6. Carruthers, J.R., et al., "Studies of Rotating Liquid Floating Zones on Skylab IV," AIAA 10th Thermophysics Conference, May 1975.

TABLE 1

TEST CONDITIONS

Nominal Configuration	Fluid	Radius Range (cm)	Zone-Length-To-Radius Ratio Range	Dynamic Input	Rotational Rate Range (rpm)	Vibrational Rate Range (Hz)
Cylinder	Distilled water	0.254	0.978 – 2.73	Bottom end rotation	637 – 2669	–
Cylinder, axes 20% offset	Distilled water	0.254	1.07 – 2.93	Eccentric bottom-end rotation	552 – 2651	–
Cylinder	Distilled water	0.254	0.780 – 2.34	Isorotation	622 – 2602	–
Cylinder, axes 20% offset	Distilled water	0.254	1.07 – 2.34	Offset isorotation	777 – 2423	–
Cylinder	Distilled water	0.254	1.07 – 2.97	Equal counter-rotation	422 – 2688	–
Cylinder, axes 20% offset	Distilled water	0.254	1.07 – 2.73	Offset equal counter-rotation	722 – 2676	–
Cylinder	1, 10, and 100-centistoke silicone fluid	0.131	1.16 – 2.32	Bottom-end rotation	1163 – 2686	–
Cylinder	1, 10, and 100-centistoke silicone fluid	0.131	1.16 – 2.32	Isorotation	1080 – 2294	–
Cylinder	1, 10, and 100-centistoke silicone fluid	0.131	1.16 – 2.32	Equal counter-rotation	1055 – 2686	–
Cylinder	Distilled water	0.066 – 0.248	0.730 – 4.80	Axial vibration of bottom end-face	–	72 – 780
Cylinder	1-centistoke silicone fluid	0.0652 – 0.131	1.16 – 3.61	Axial vibration of bottom end-face	–	35 – 650
Cylinder, non-parallel end-faces	Distilled water	0.254	1.17 – 2.34	Bottom end rotation	779 – 2537	–
Cylinder, non-parallel end-faces, axes 20% offset	Distilled water	0.254	1.36 – 2.34	Offset bottom end rotation	754 – 2383	–
Cylinder, Non-parallel end-faces	Distilled water	0.254	0.974 – 2.34	Isorotation	749 – 1978	–
Cylinder, non-parallel end-faces, axes 20% offset	Distilled water	0.254	0.974 – 2.34	Offset isorotation	737 – 1974	–
Cylinder, non-parallel end-faces	Distilled water	0.254	1.36 – 2.34	Equal counter-rotation	772 – 2643	–
Cylinder, non-parallel end-faces, axes 20% offset	Distilled water	0.254	1.17 – 2.34	Offset equal counter-rotation	771 – 2646	–

		Large End Radius (cm)	Zone Large End To-Small End Radius Ratio Range	Zone Length-To-Large End Radius Ratio Range			
Cone	Distilled water	0.254	2.0 – 3.07	0.592 – 1.78	Top-end rotation	1213 – 2824	–
Cone, axes 20% large-end offset	Distilled water	0.254	3.07	0.986 – 1.58	Offset top-end rotation	1374 – 2826	–
Cone	Distilled water	0.254	2.0 – 3.07	0.592 – 1.77	Bottom-end rotation	1042 – 2679	–
Cone, axes 20% large-end offset	Distilled water	0.254	3.07	0.592 – 1.58	Offset bottom-end rotation	998 – 2681	–
Cone	Distilled water	0.254	2.0 – 3.07	0.592 – 1.77	Corotation	920 – 2829	–
Cone, axes 20% large-end offset	Distilled water	0.254	3.07	0.986 – 1.58	Offset corotation	1348 – 2003	–
Cone	Distilled water	0.254	2.0 – 3.07	0.787 – 1.77	Counter-rotation	1016 – 2828	–
Cone, axes 20% large-end offset	Distilled water	0.254	3.07	0.986 – 1.38	Offset counter-rotation	1204 – 2830	–

TABLE 2

FLUID PROPERTIES

Fluid	Density (gm/cc)	Viscosity		Surface Tension (dyne/cm)
		Kinematic (c.s.)	Dynamic (dyne-sec/cm^2)	
Water	1.00	1	0.010	72.6
Silicone Fluid	0.82	1	0.0082	17.4
	0.94	10	0.094	20.1
	0.97	100	0.970	20.9

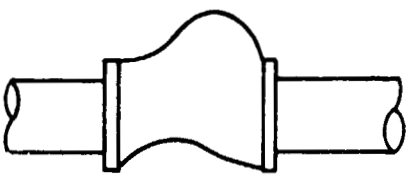

Figure 1a C-Mode Deformation

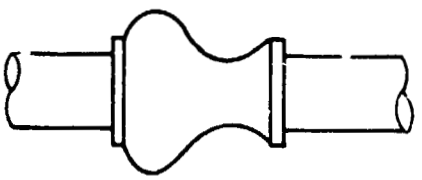

Figure 1b Axisymmetric Deformation

FIGURE 1 UNSTABLE SHAPES OF ROTATING LIQUID ZONES

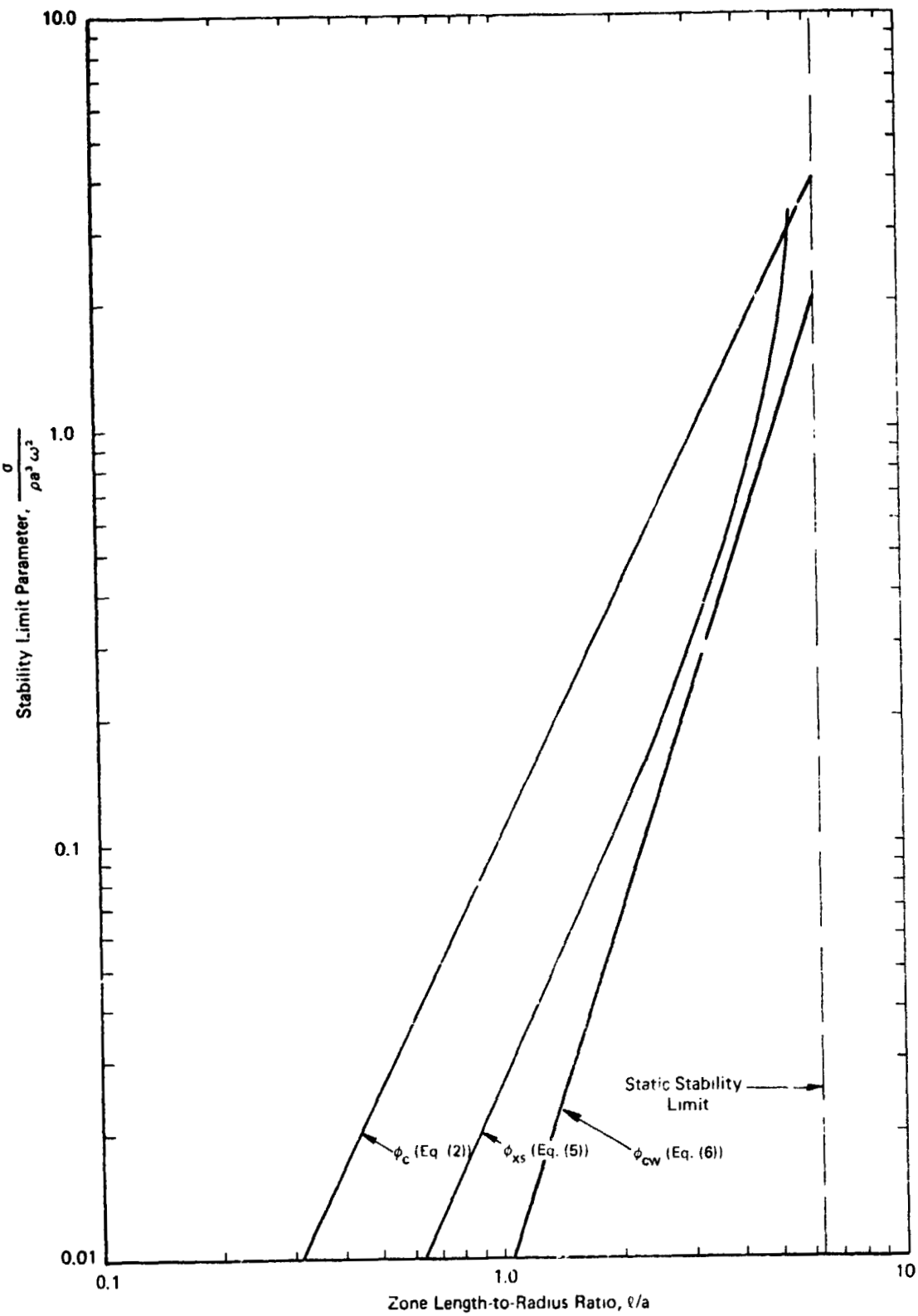

FIGURE 2 THEORETICAL STABILITY CRITERIA FOR CYLINDRICAL COLUMN

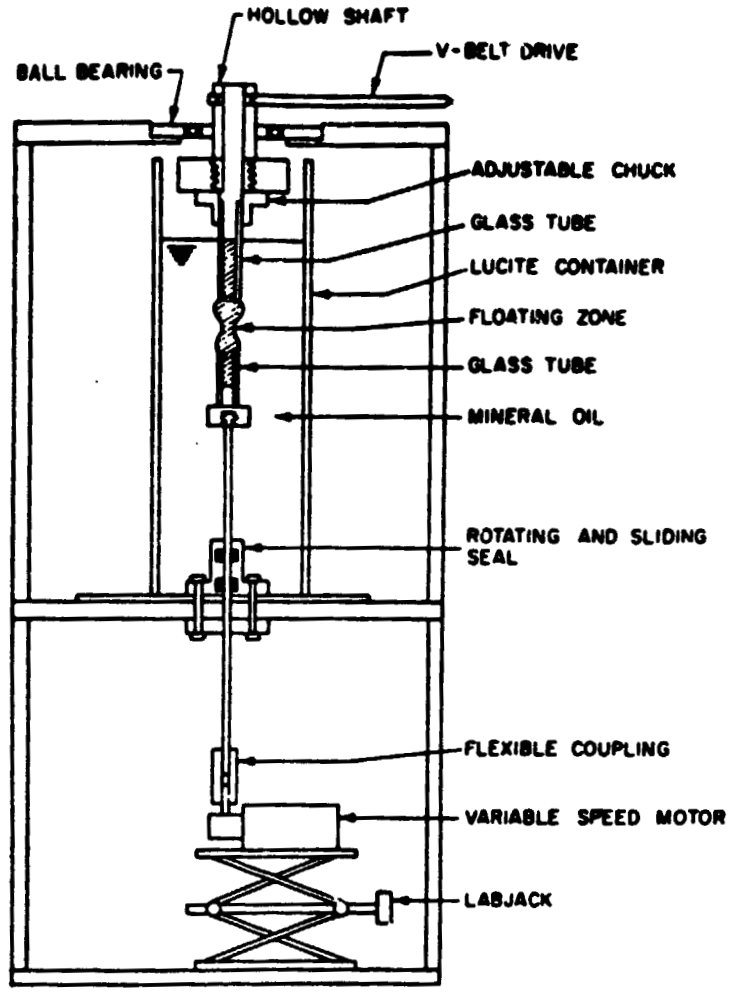

FIGURE 3 EXPERIMENTAL APPARATUS USED FOR FLOATING LIQUID ZONE STUDIES BY PLATEAU SIMULATION

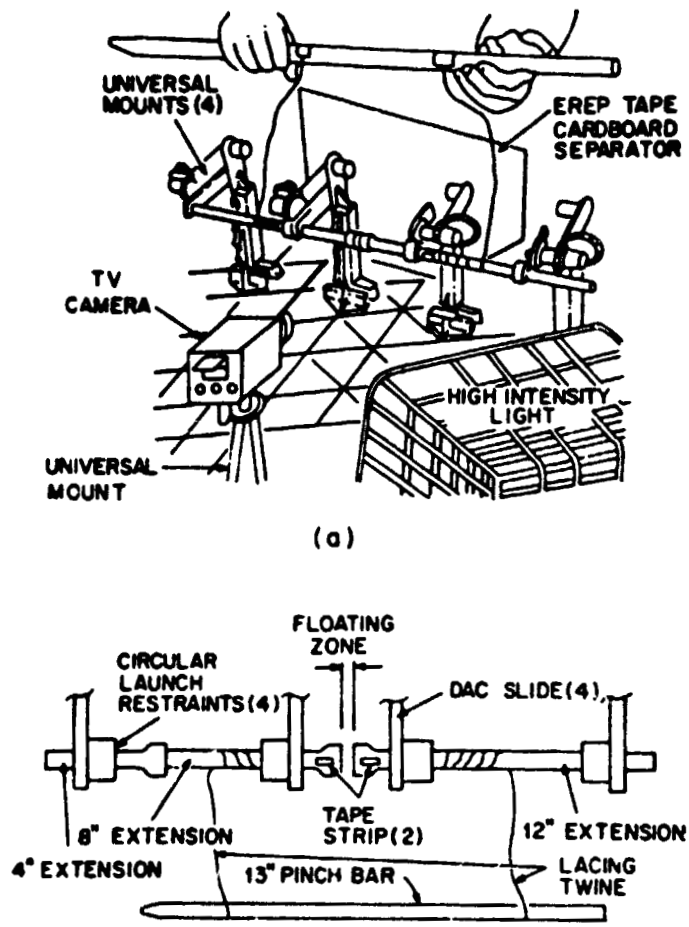

FIGURE 4 EXPERIMENTAL APPARATUS FOR LIQUID FLOATING ZONE STUDIES ON SKYLAB IV

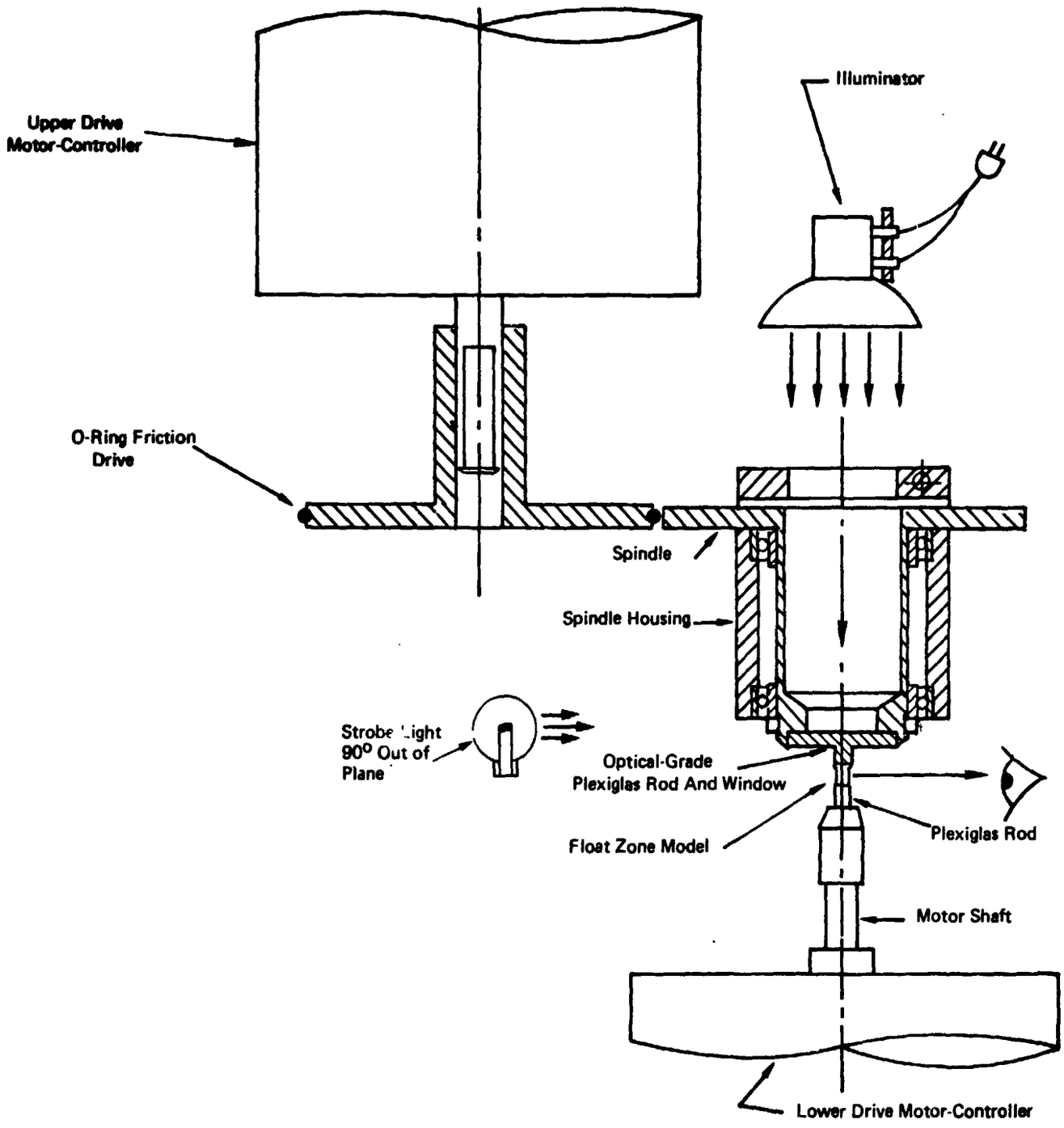

FIGURE 5 EXPERIMENTAL APPARATUS USED FOR FLOATING ZONE STUDIES BY LOW BOND NUMBER SIMULATION

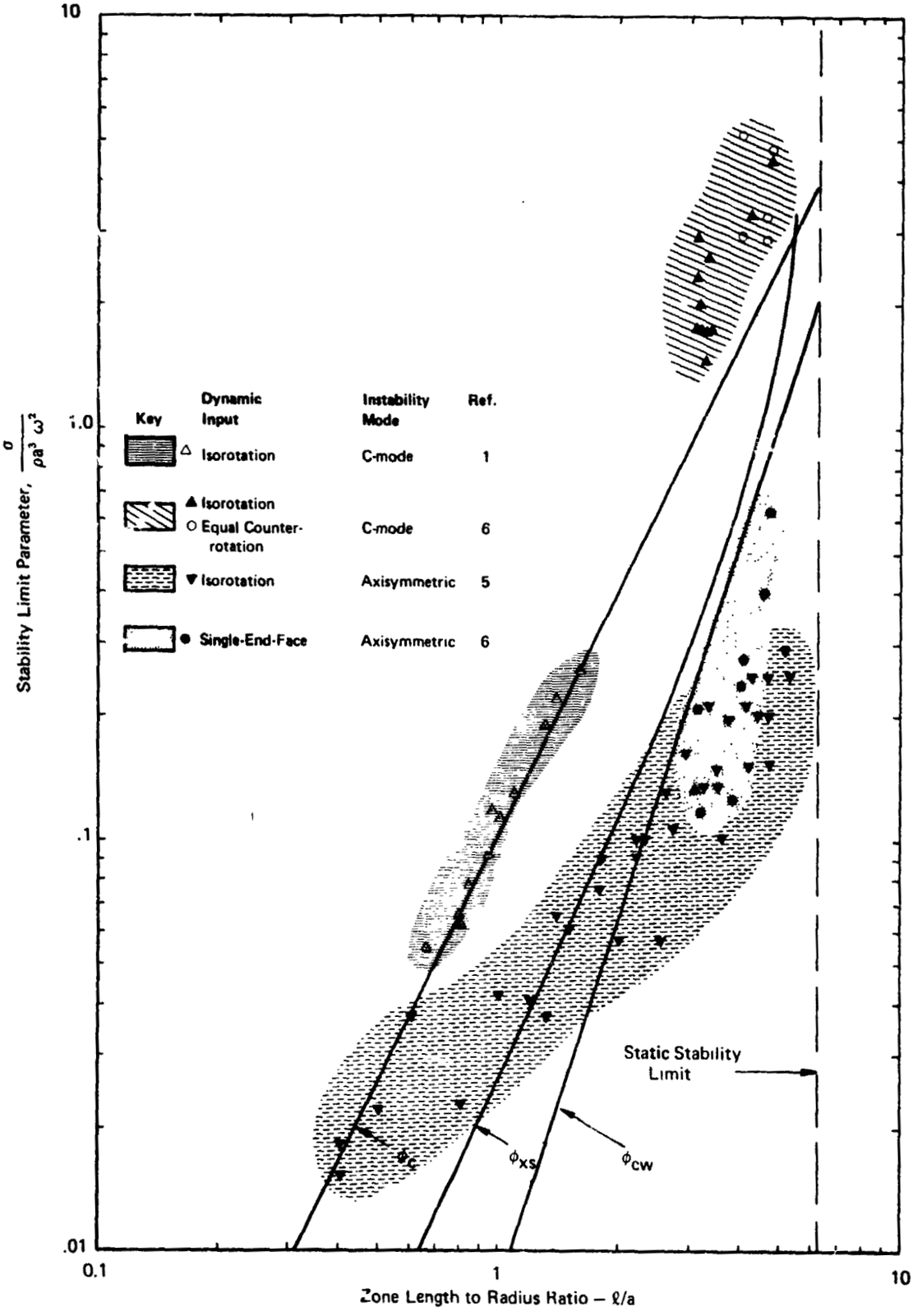

FIGURE 6 COMPARISON OF EXPERIMENTS AND THEORIES ON THE STABILITY OF ROTATING CYLINDRICAL LIQUID COLUMNS

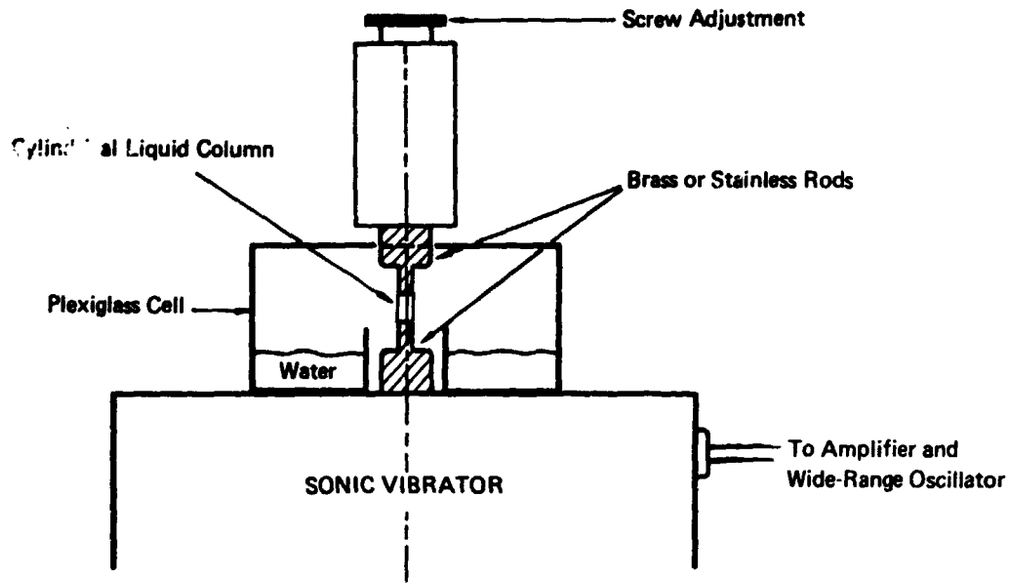

FIGURE 7 SCHEMATIC OF EXPERIMENTAL APPARATUS USED FOR AXIAL VIBRATION OF CYLINDRICAL LIQUID COLUMNS

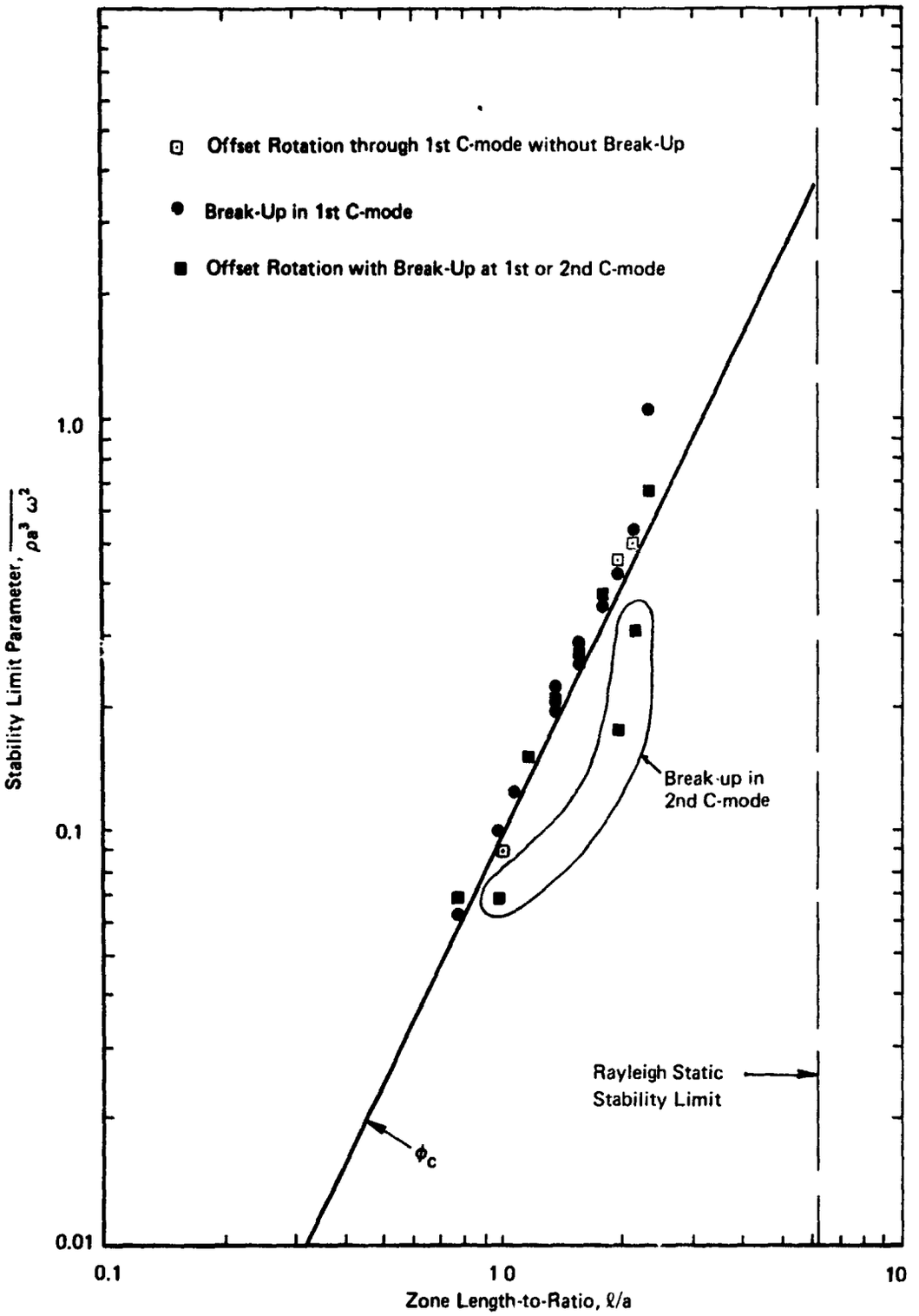

FIGURE 8 CYLINDRICAL WATER COLUMN – ISOROTATION

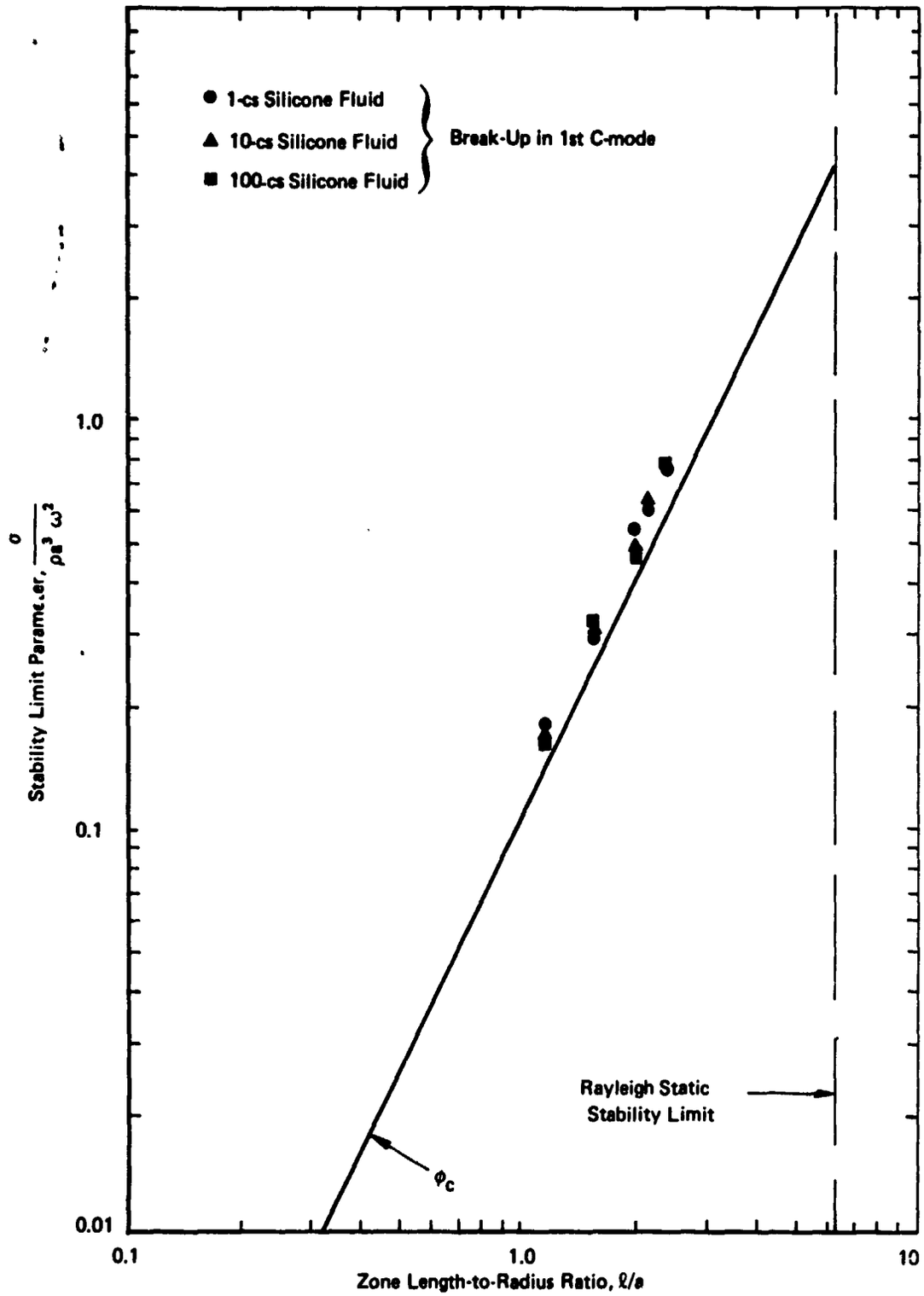

FIGURE 9 CYLINDRICAL SILICONE COLUMN – ISOROTATION

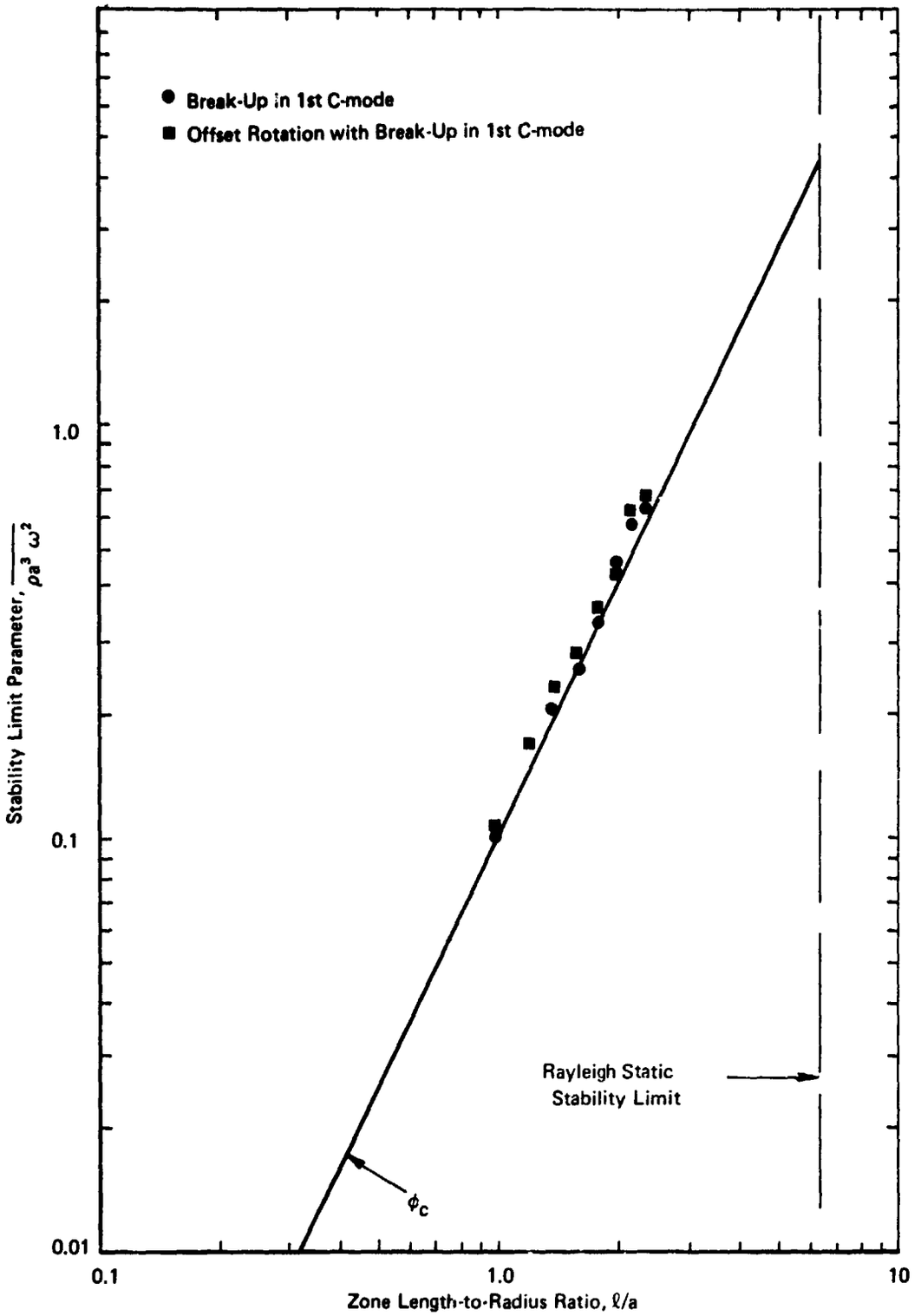

FIGURE 10 CYLINDRICAL WATER COLUMN – NON-PARALLEL END-FACES, ISOROTATION

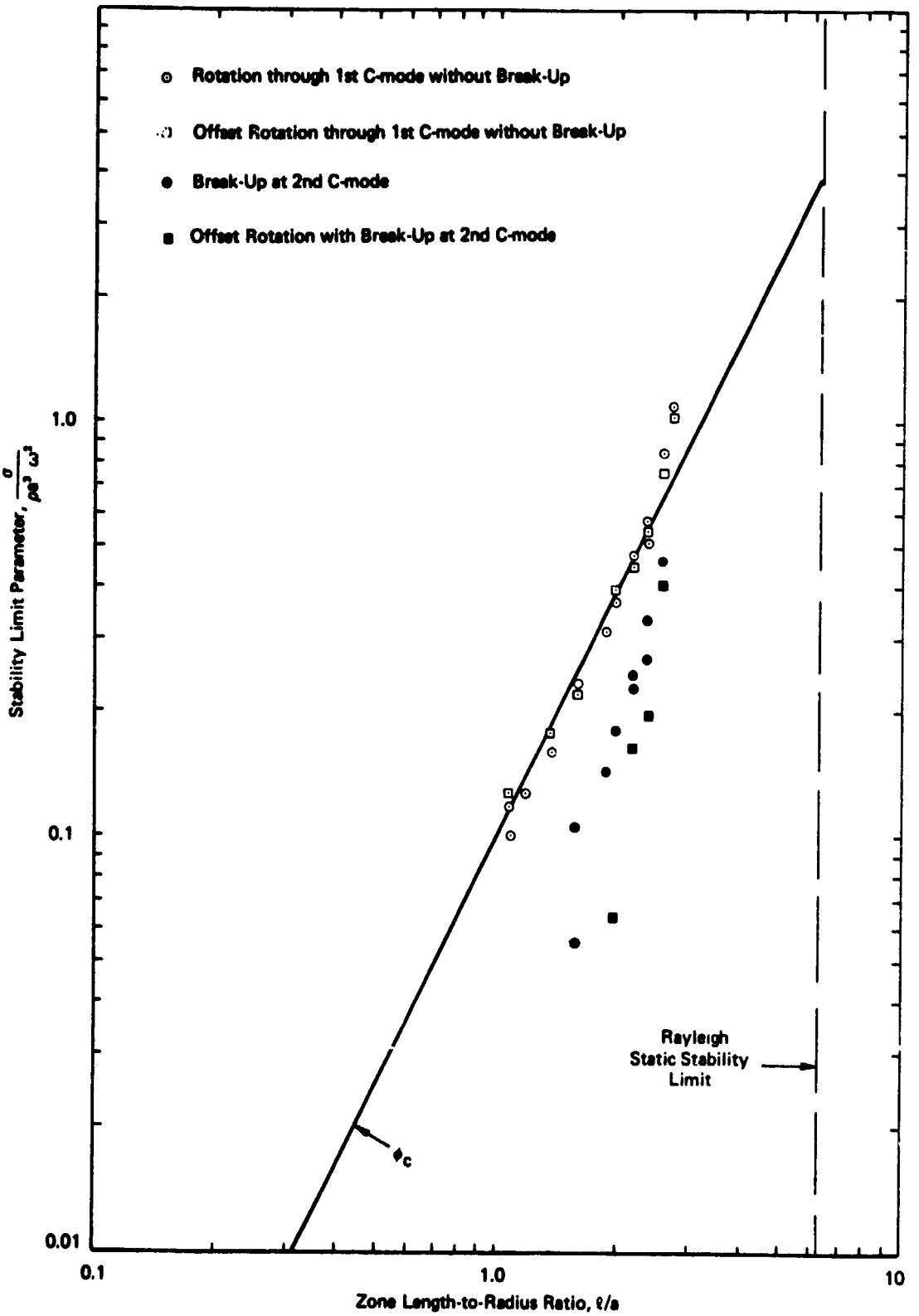

FIGURE 11 CYCLINDRICAL WATER COLUMN – EQUAL COUNTER-ROTATION

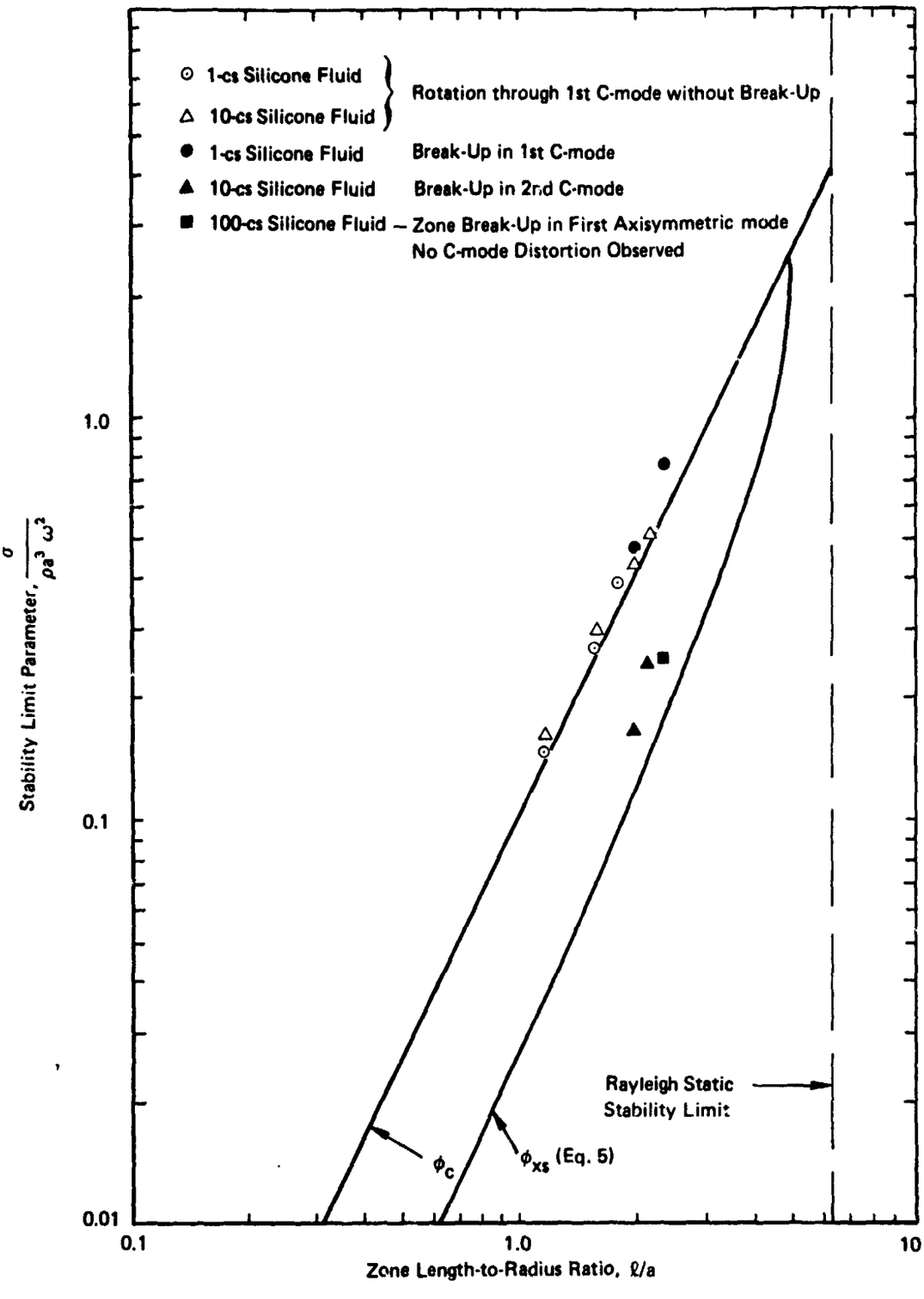

FIGURE 12 CYLINDRICAL SILICONE COLUMN – EQUAL COUNTER-ROTATION

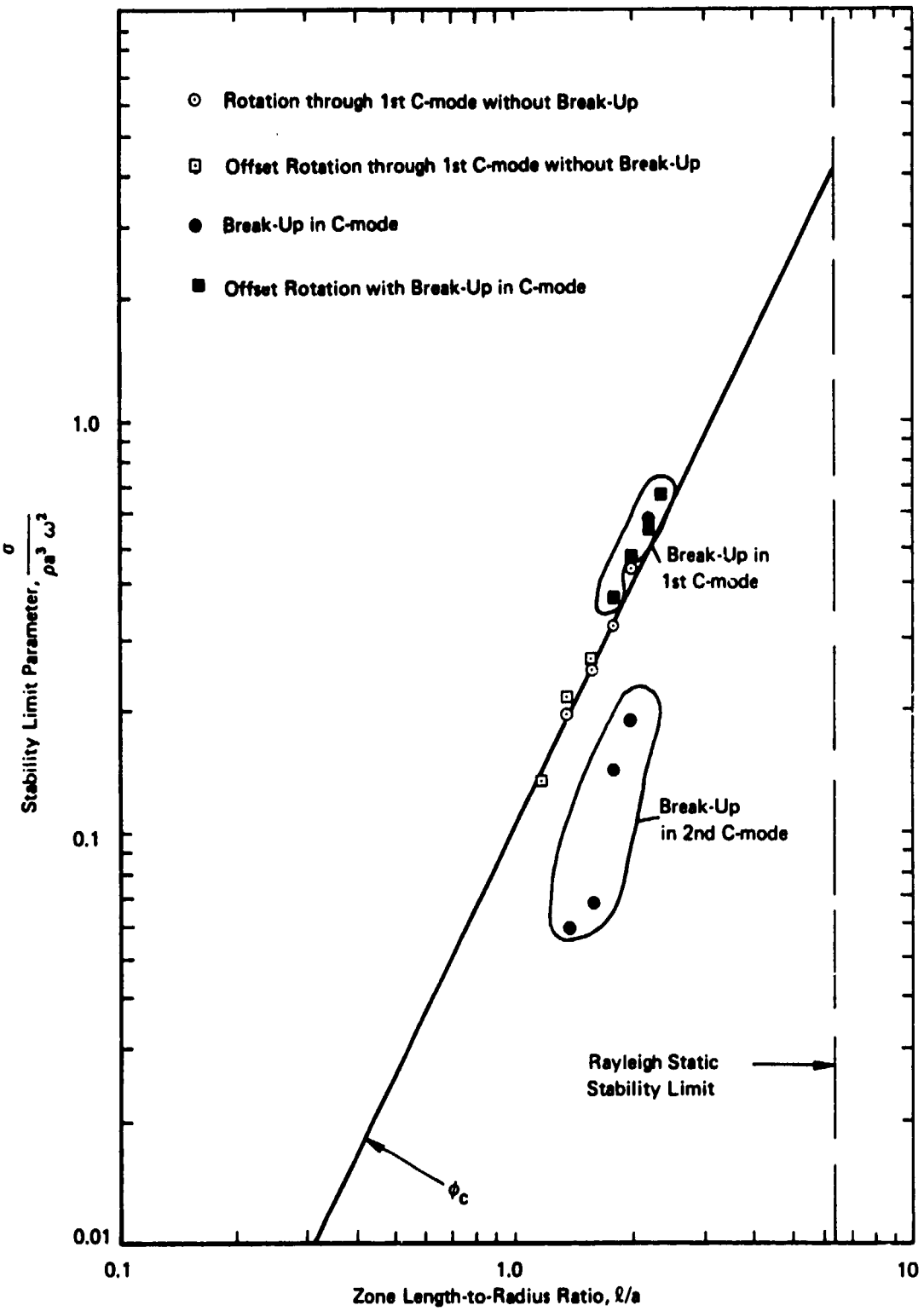

FIGURE 13 CYLINDRICAL WATER COLUMN – NON-PARALLEL END-FACES, EQUAL COUNTERROTATION

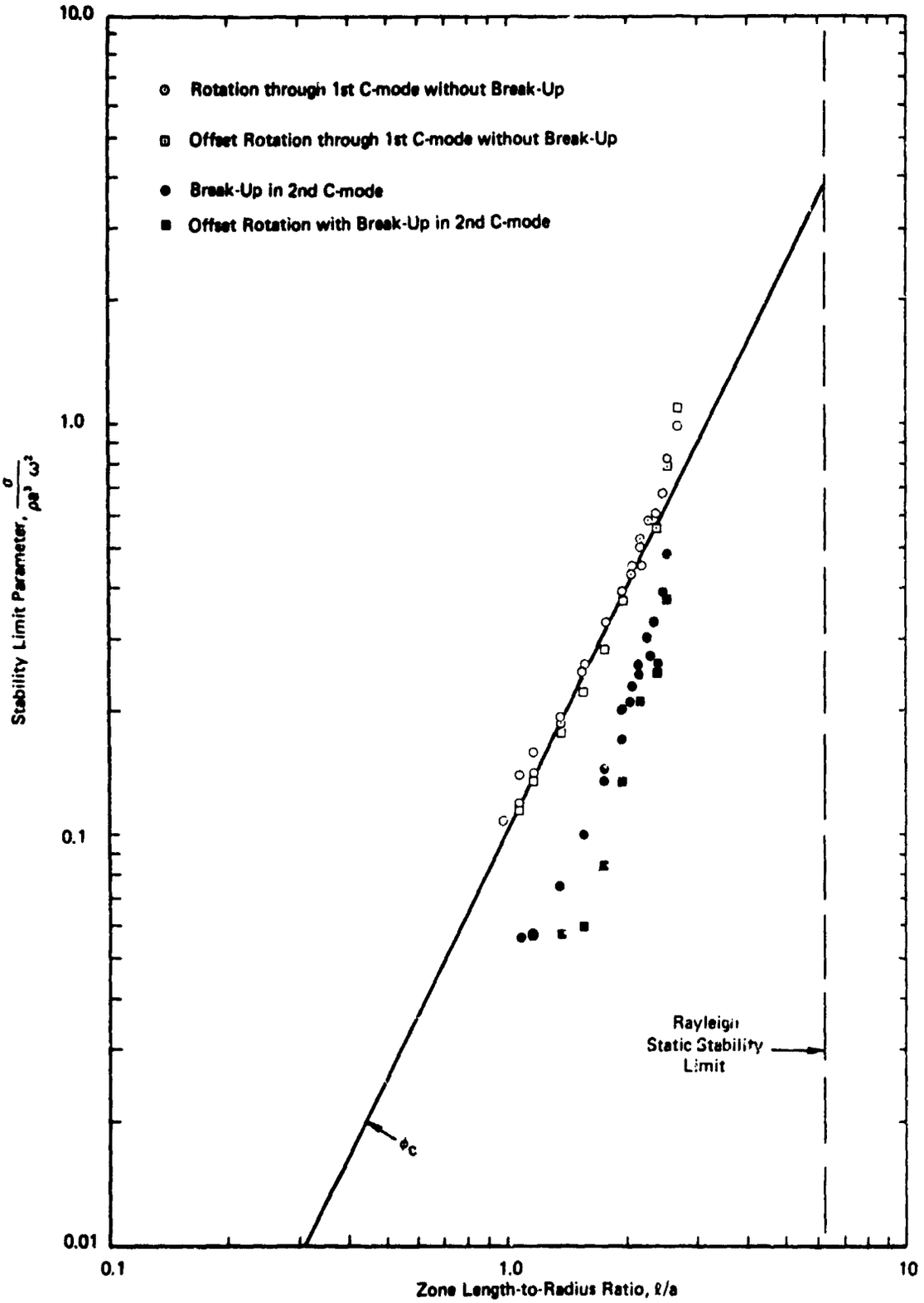

FIGURE 14 CYLINDRICAL WATER COLUMN – SINGLE-END ROTATION

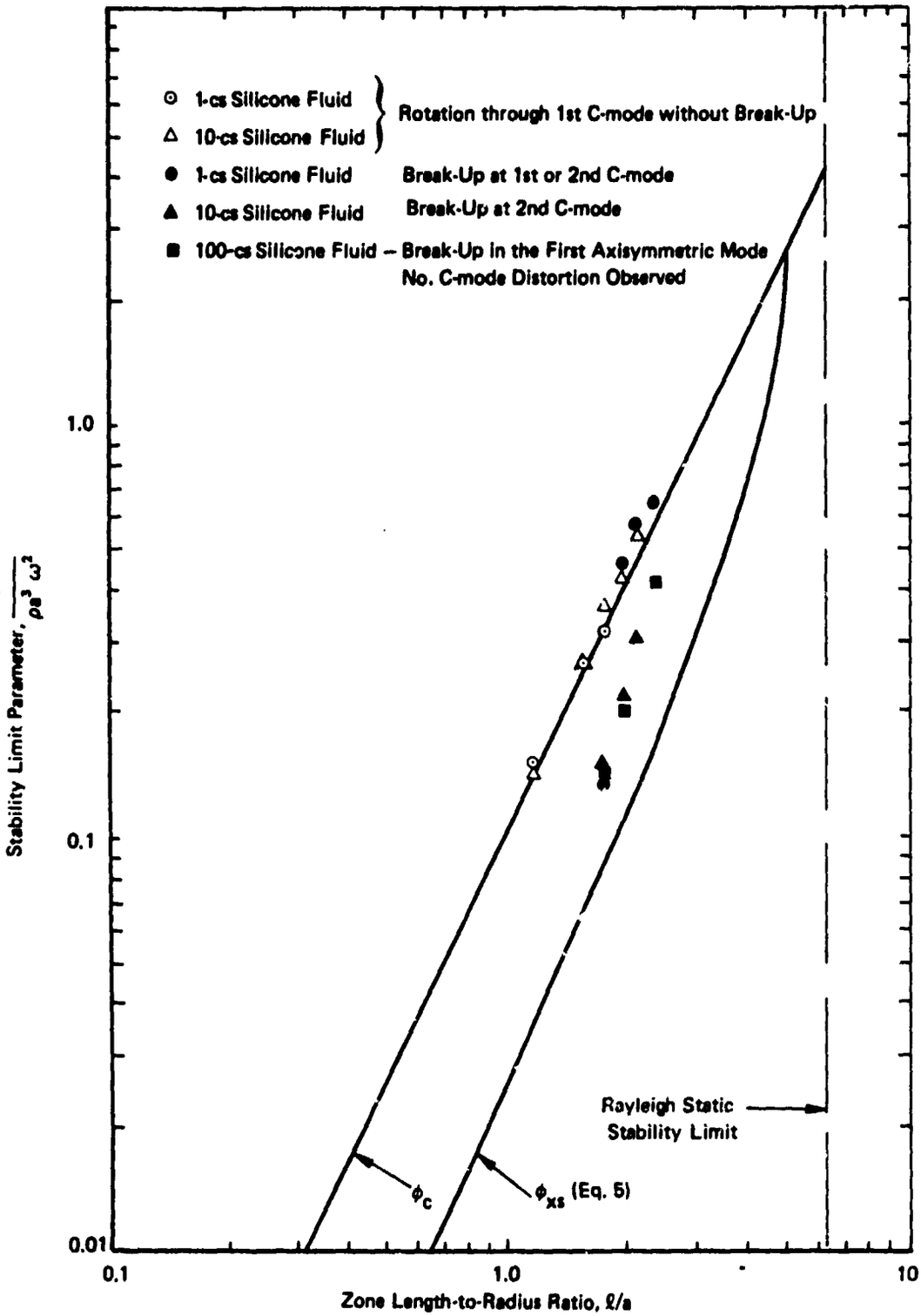

FIGURE 15 CYLINDRICAL SILICONE COLUMN – SINGLE-END ROTATION

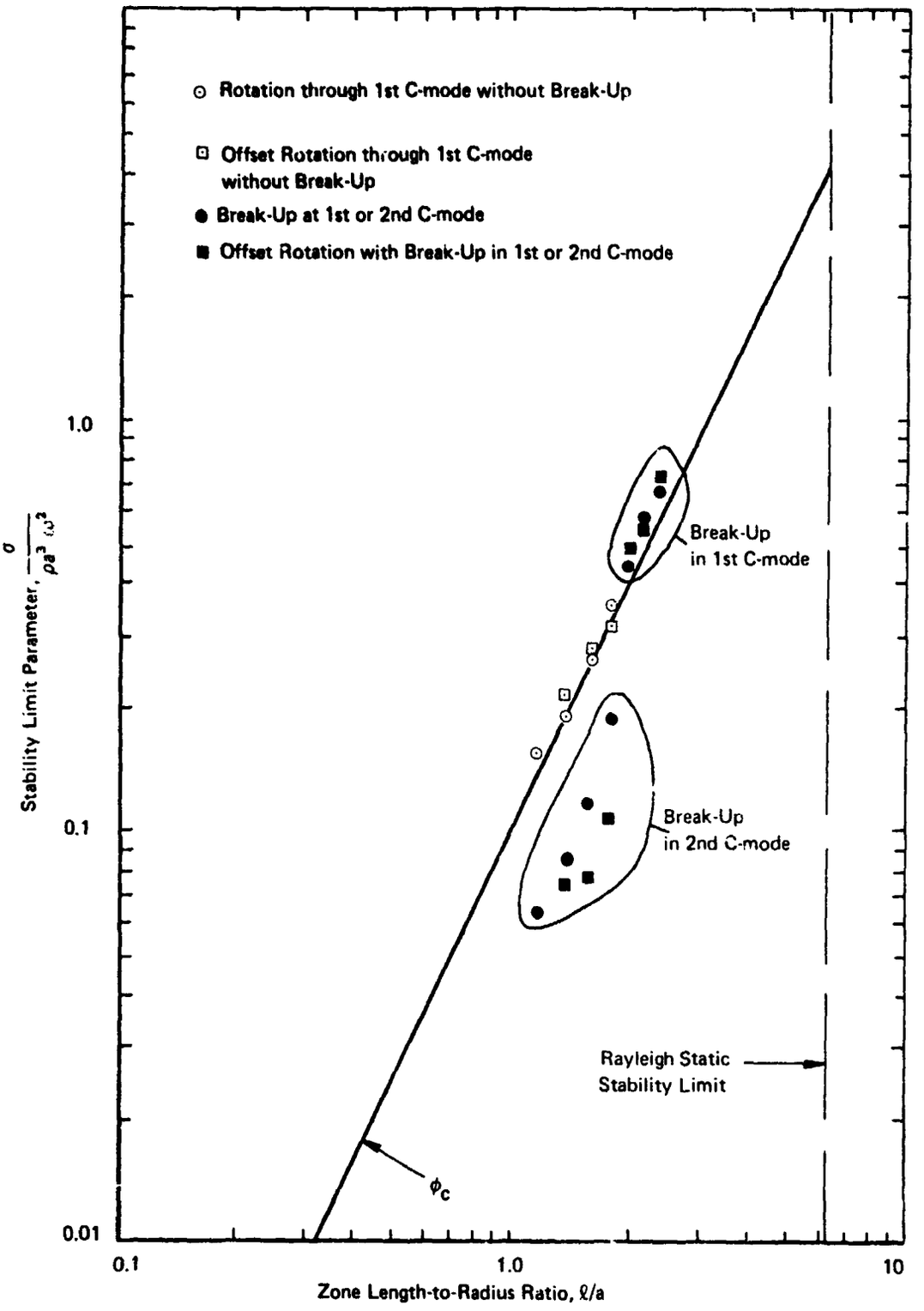

FIGURE 16 CYLINDRICAL WATER COLUMN – NON PARALLEL END-FACES, SINGLE-END ROTATION

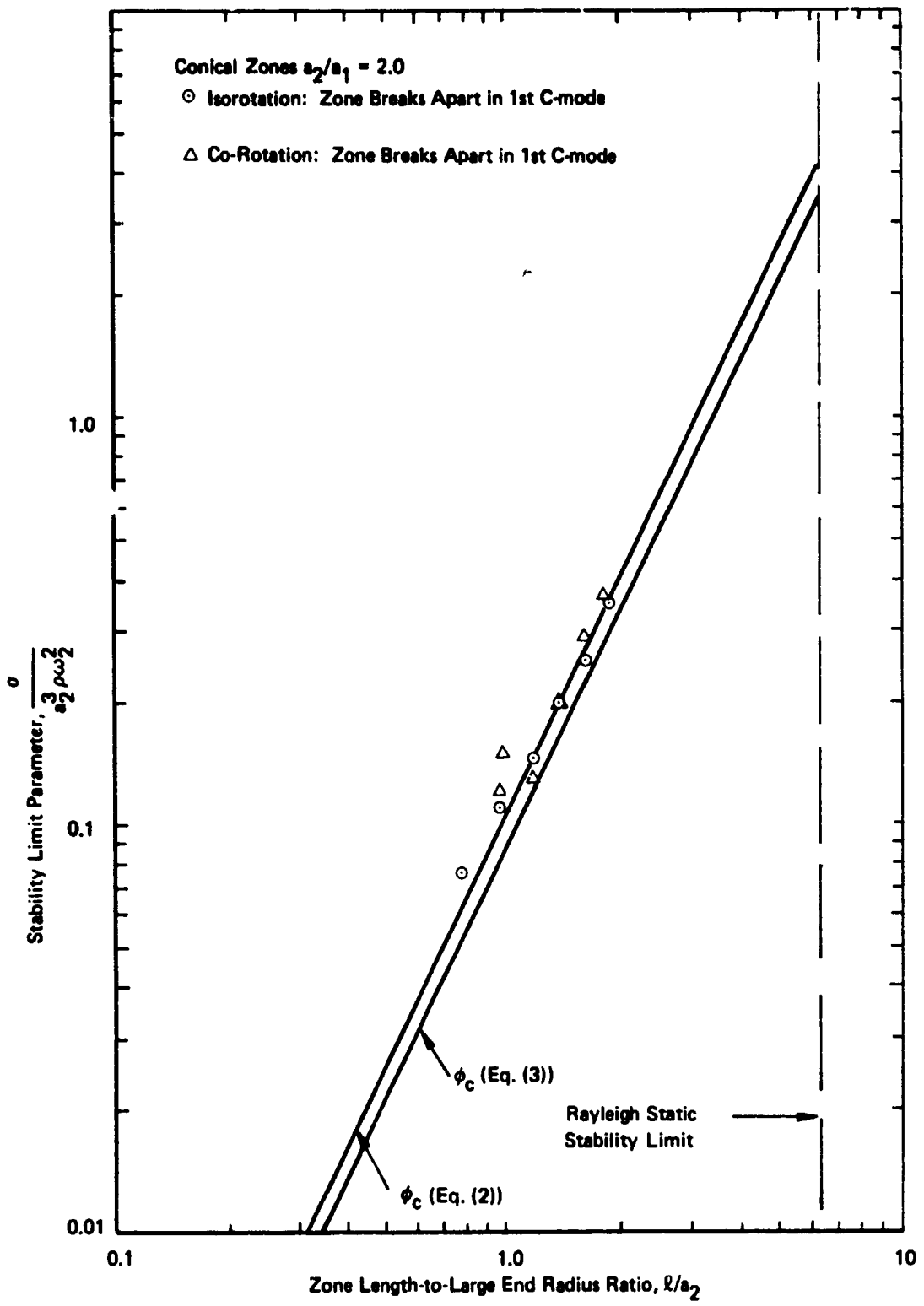

FIGURE 17 CONICAL WATER COLUMN – ISOROTATION AND CO-ROTATION

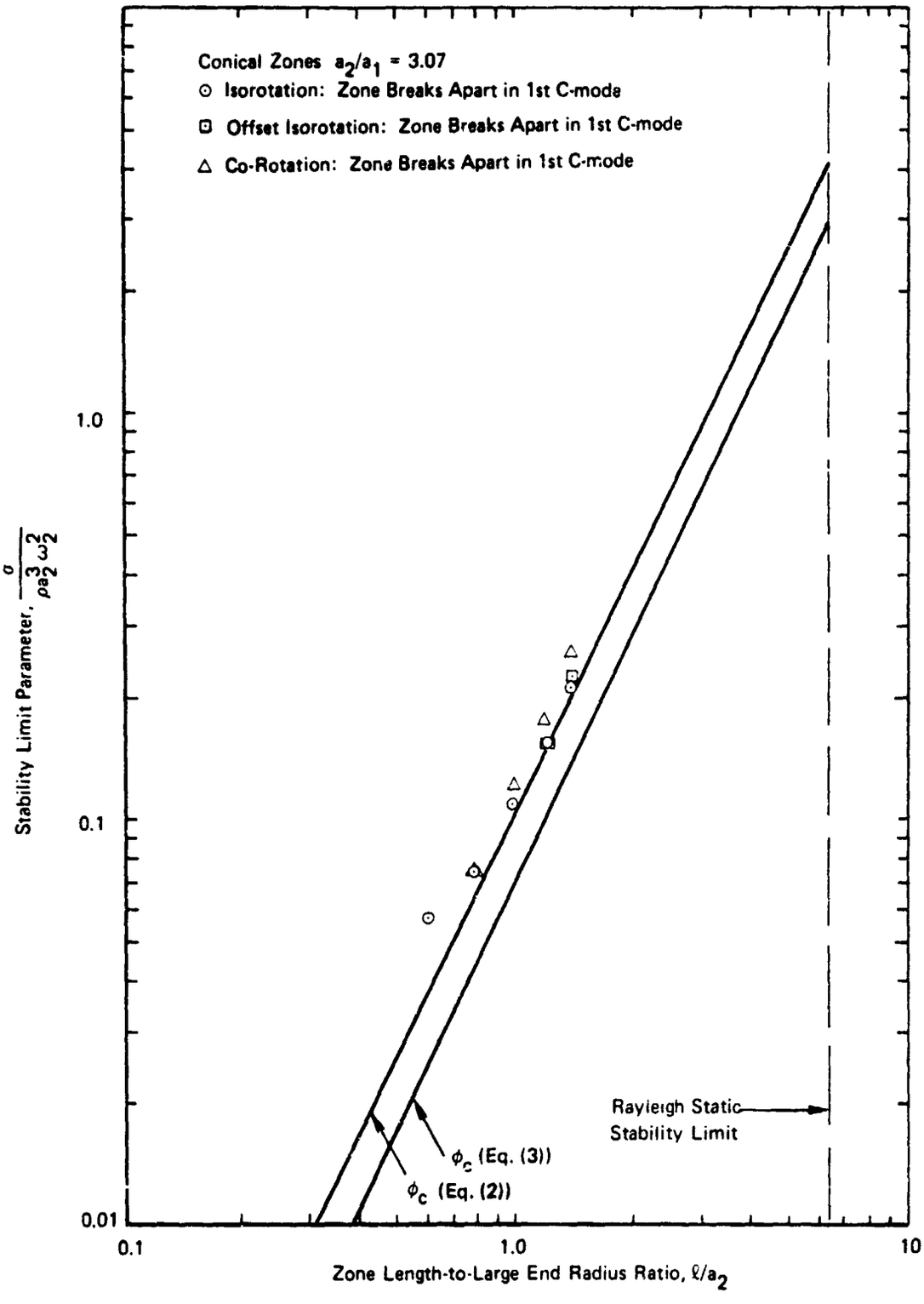

FIGURE 18 CONICAL WATER COLUMN – ISOROTATION AND CO-ROTATION

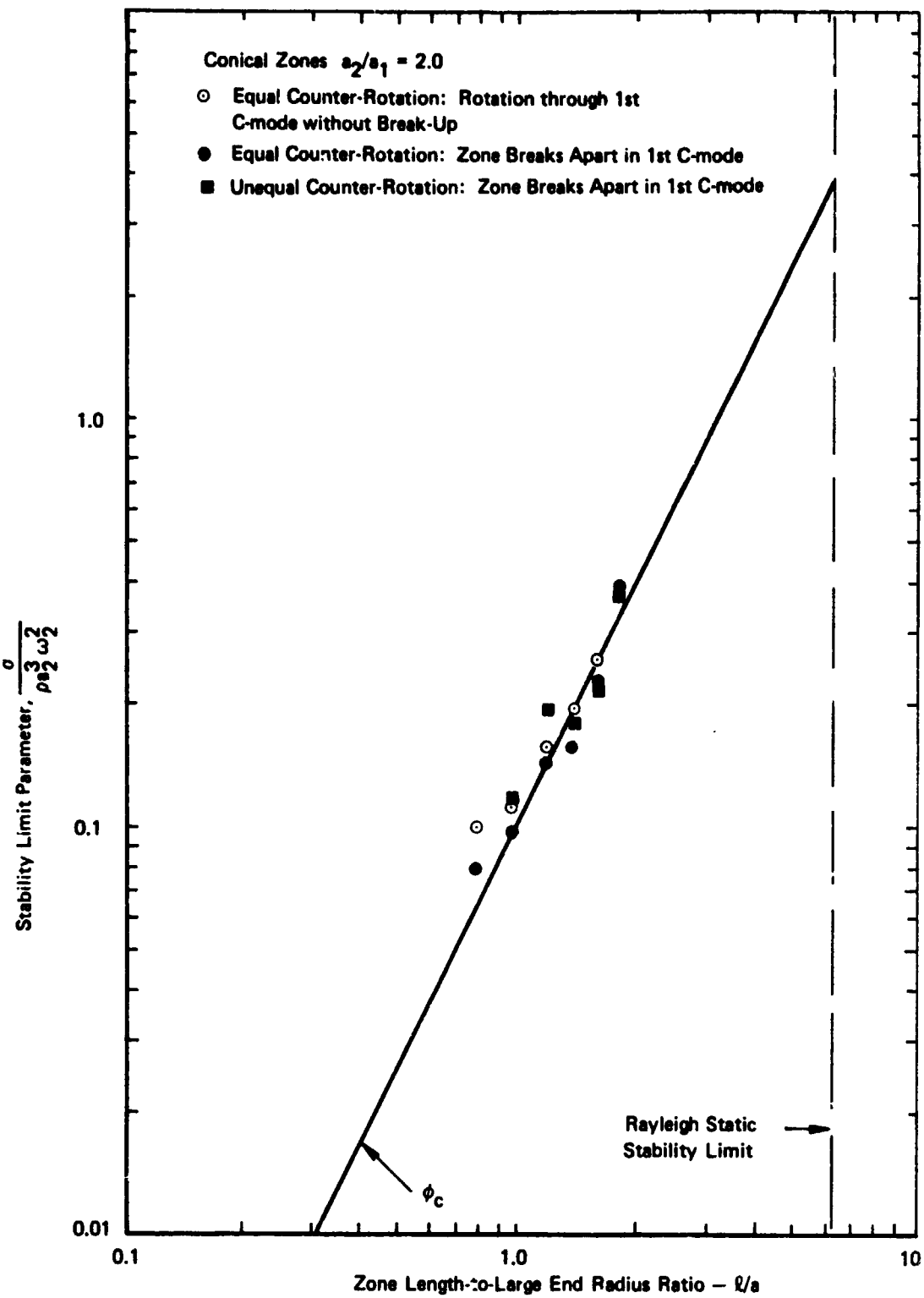

FIGURE 19 CONICAL WATER COLUMN -- EQUAL AND UNEQUAL COUNTER-ROTATION

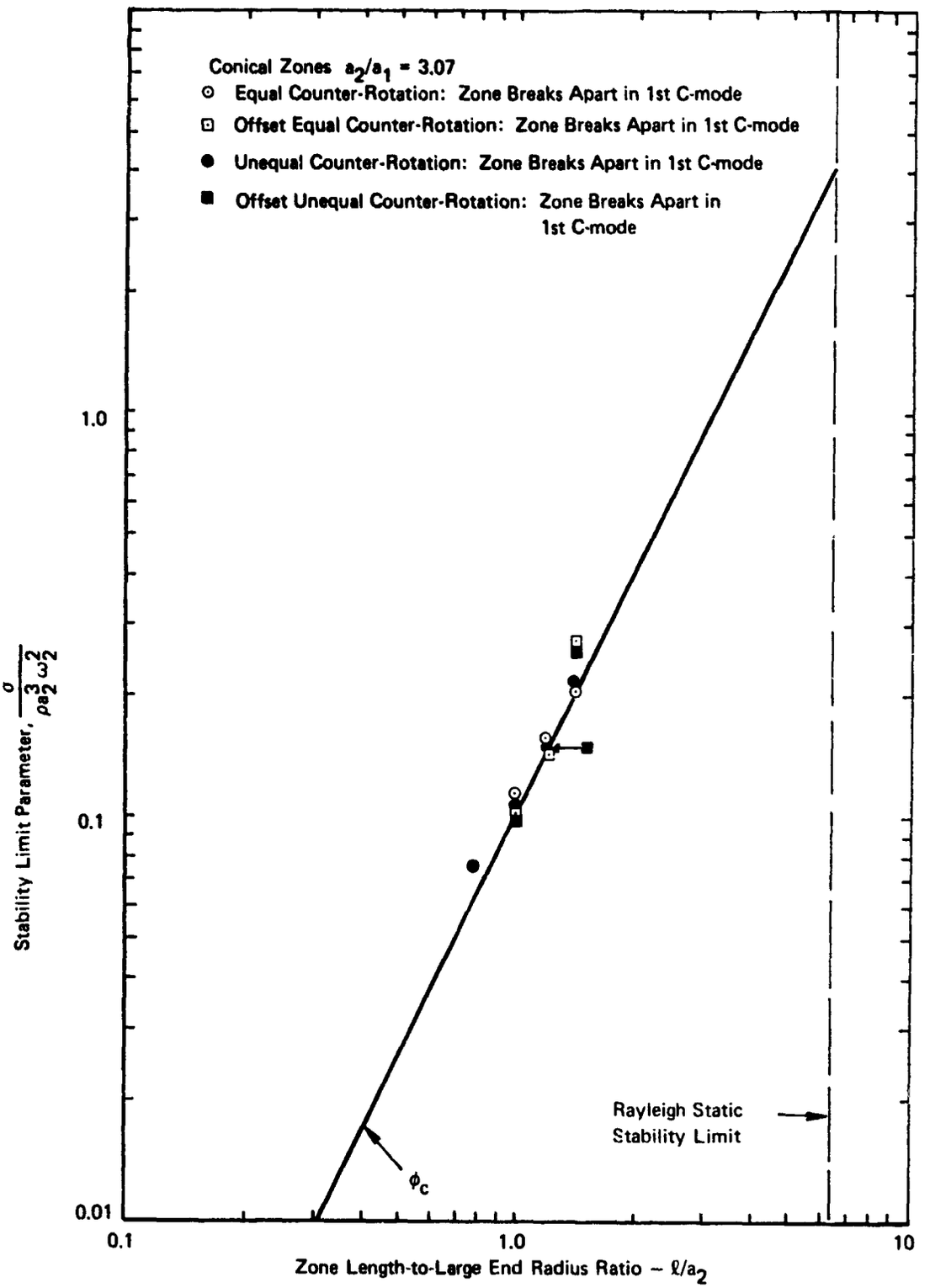

FIGURE 20 CONICAL WATER COLUMN – EQUAL AND UNEQUAL COUNTER-ROTATION

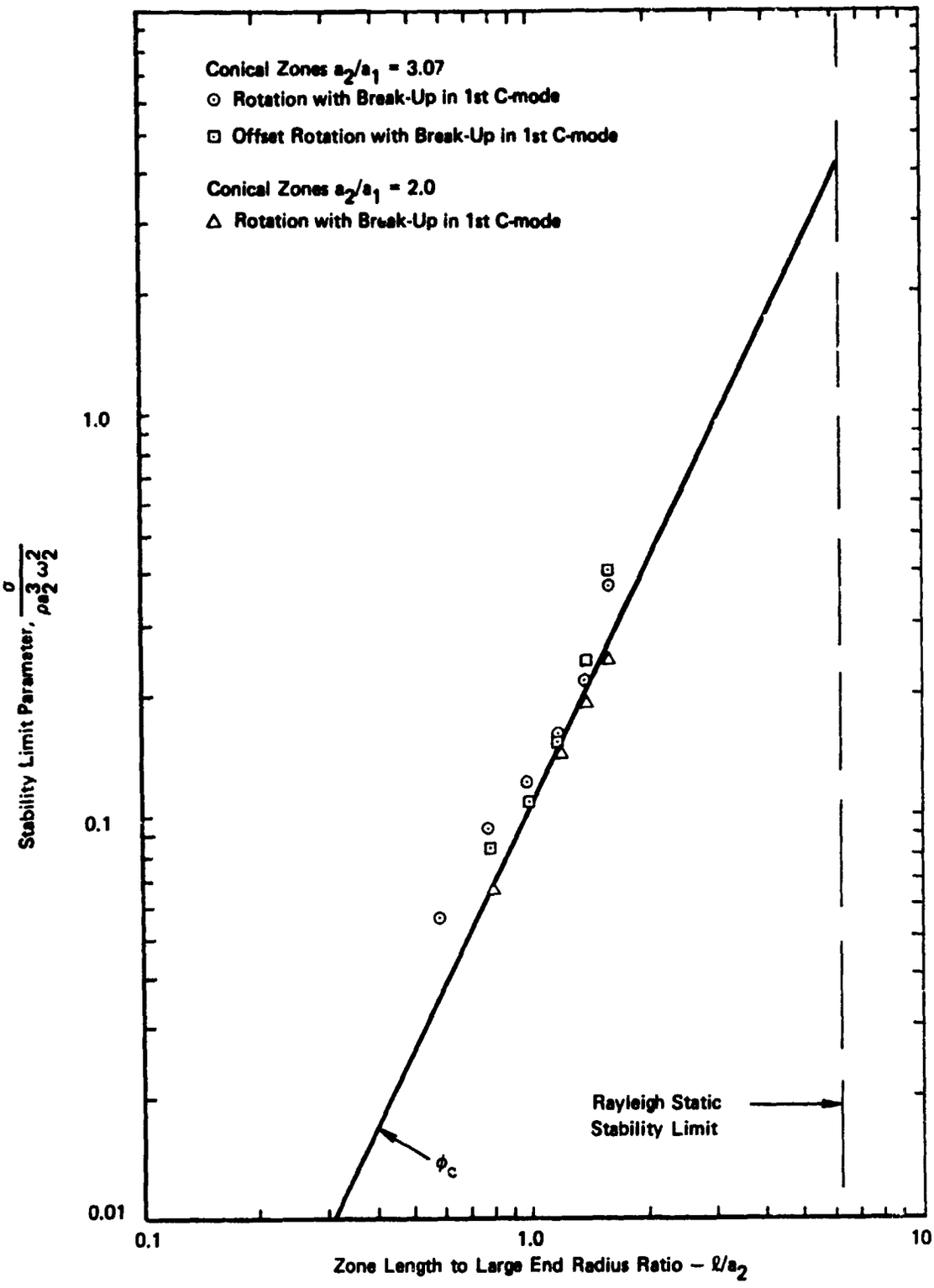

FIGURE 21 CONICAL WATER COLUMN – BOTTON-END ROTATION

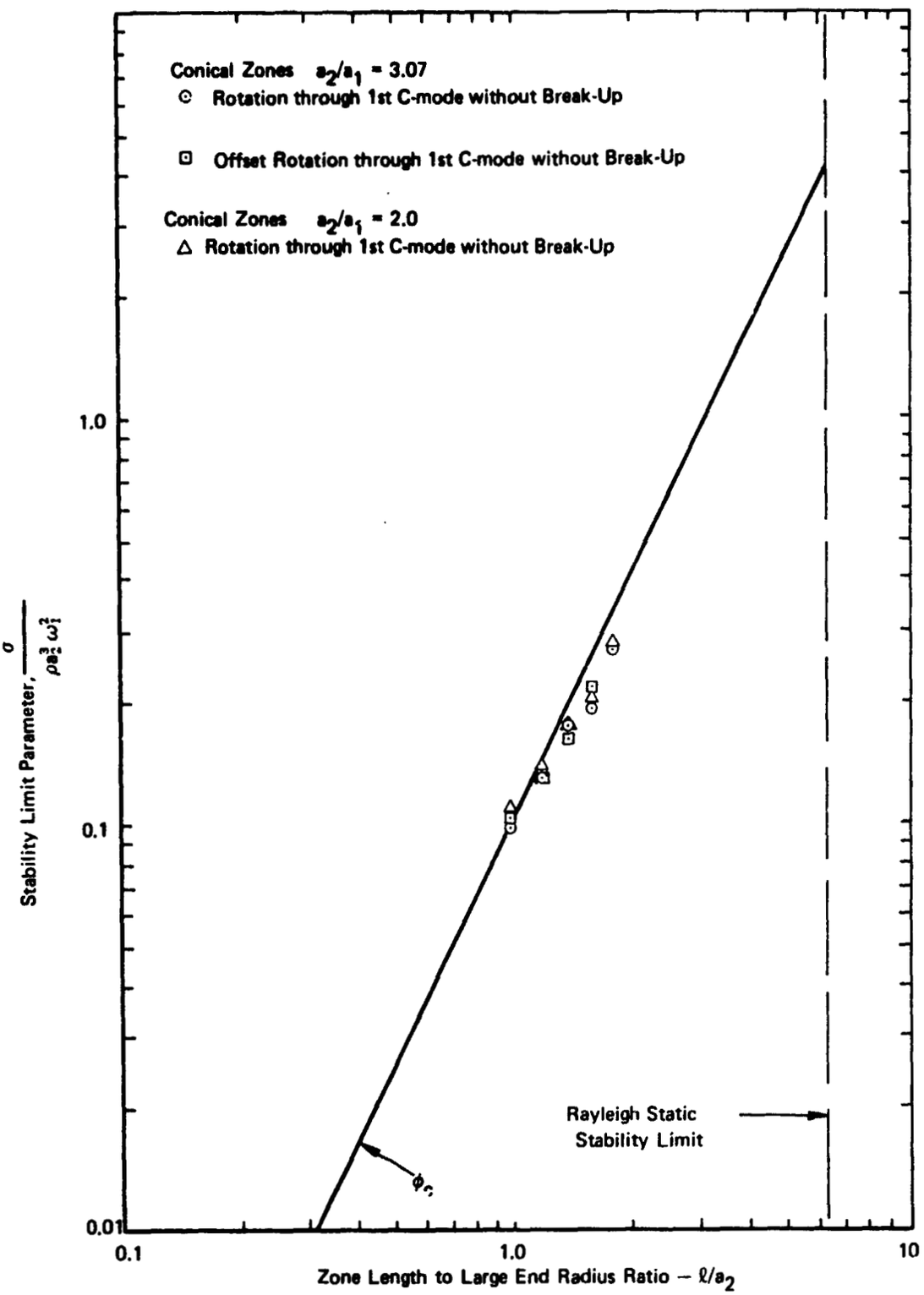

FIGURE 22 CONICAL WATER COLUMN – TOP-END ROTATION

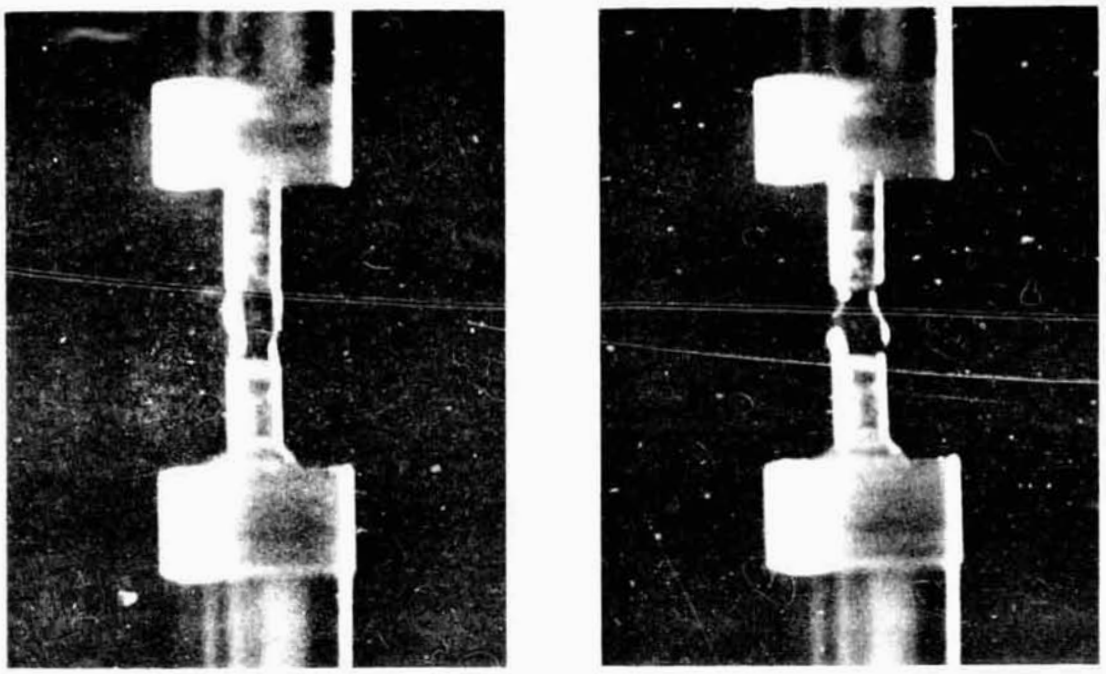

First Mode (n = 2)

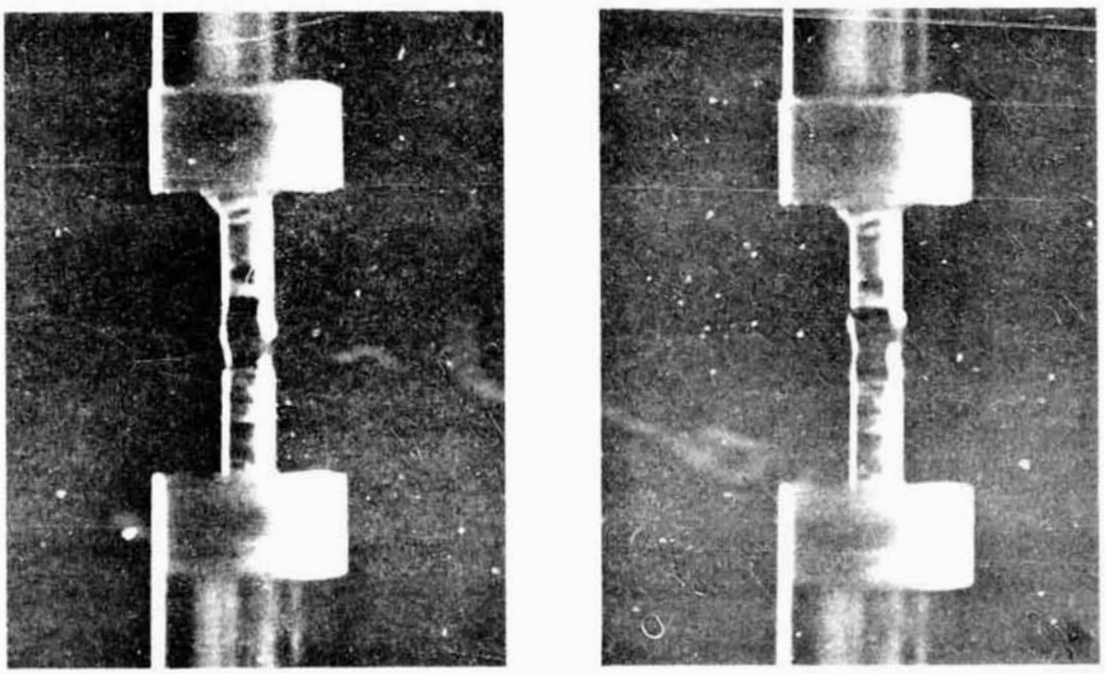

Second Mode (n = 3)

FIGURE 23 **SHAPES OF CYLINDRICAL ZONES AXIALLY VIBRATED IN FIRST TWO MODES OF RESONANCE**

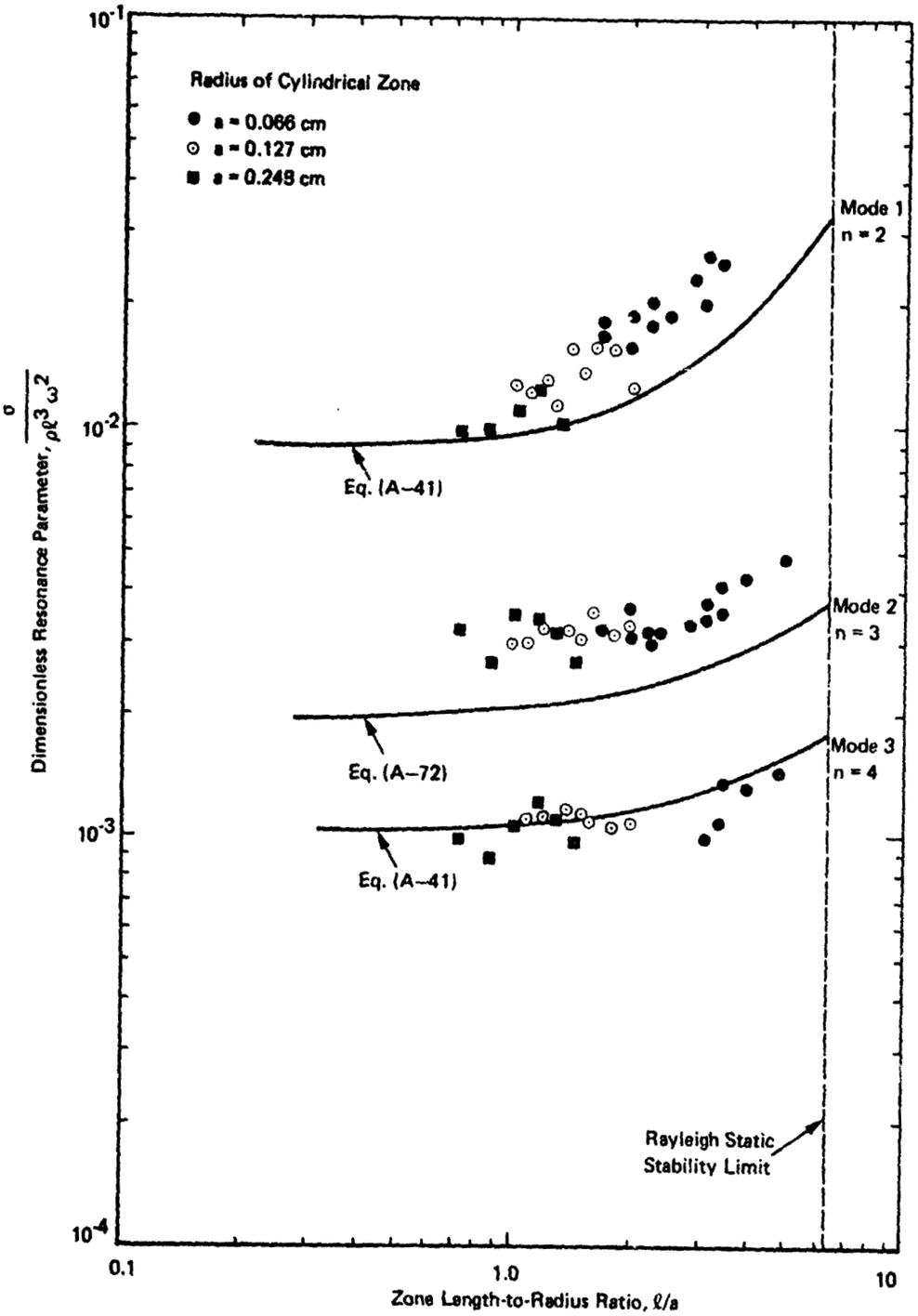

FIGURE 24 AXIALLY-VIBRATED CYLINDRICAL COLUMNS OF WATER

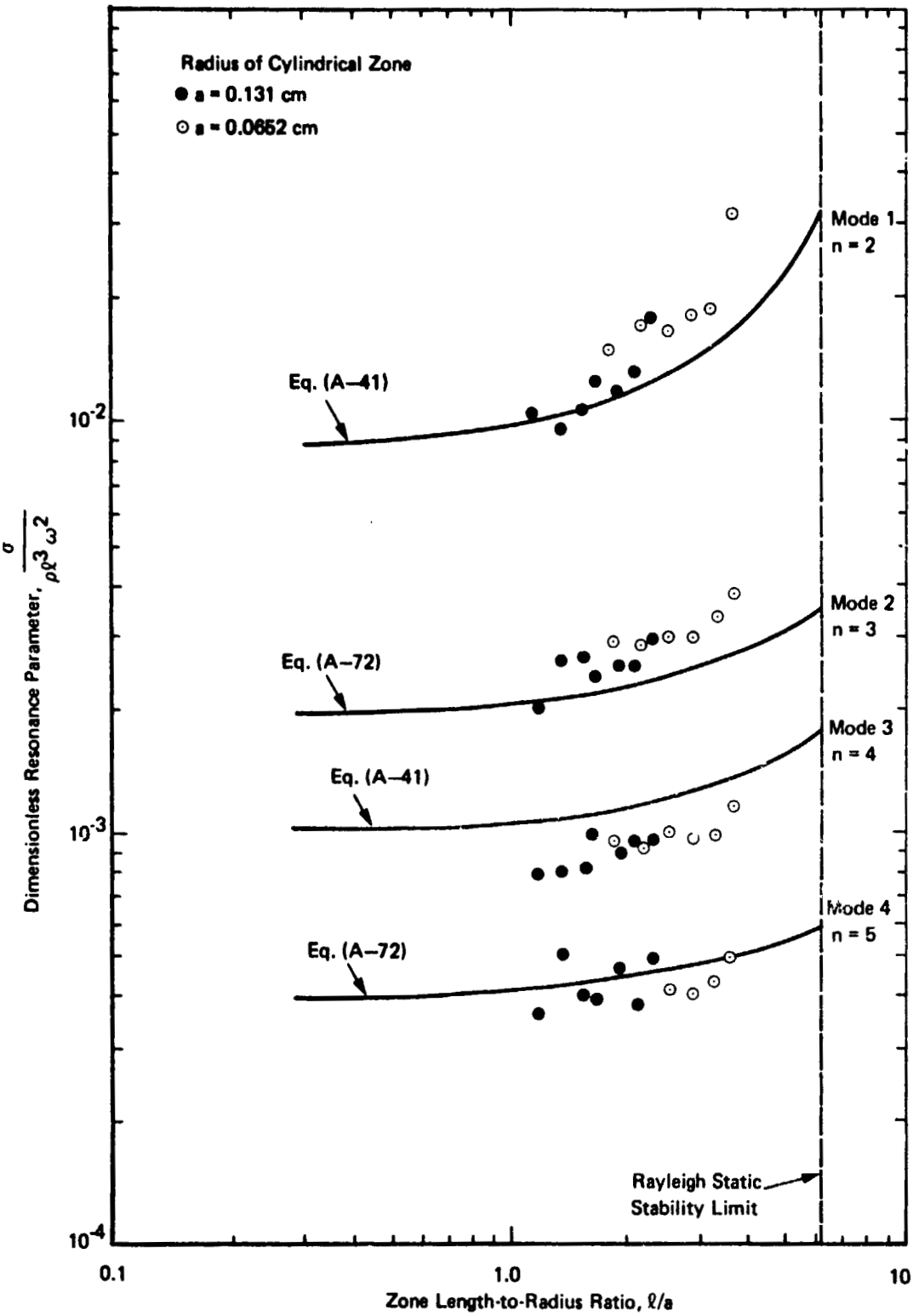

FIGURE 26 AXIALLY-VIBRATED CYLINDRICAL COLUMNS OF SILICONE

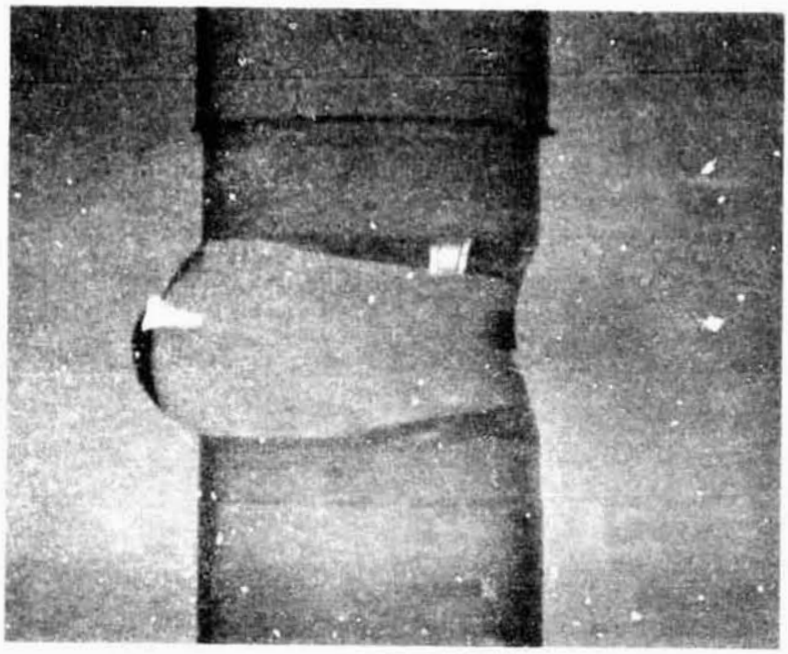

a) Liquid Zone Rotates in C-Mode Deformation

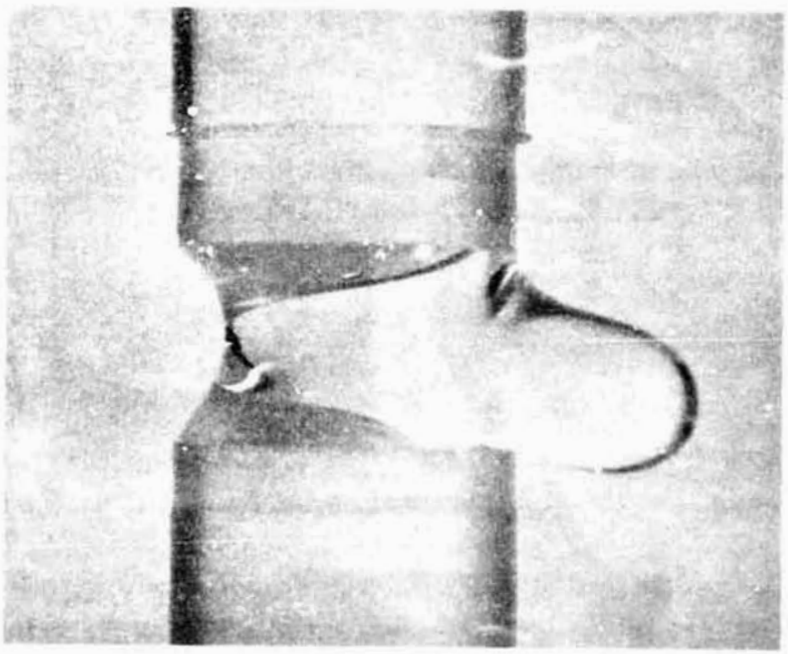

b) Liquid Zone Failure in C-Mode

FIGURE 26 CYLINDRICAL WATER ZONE IN C-MODE DEFORMATION

APPENDIX

THE PREDICTION OF THE NORMAL VIBRATIONS OF A CYLINDER OF LIQUID

The Normal Vibrations of a Cylinder of Fluid

In Figure A-1 we show a circular cylinder of fluid suspended by capillary forces between two rigid circular plates. The fluid represents the molten zone in a crystal-growing process, and the circular plates represent the ends of the feed rod and growing crystal. We assume that the effects of gravity can be ignored, either because of the small size of the fluid zone or because the experiment is performed in a weightless environment.

In Figure A-2 we show a mode (characterized by mode number n=1) which is not possible to realize in the case of a cylinder of fluid because the volume is not conserved. Because this mode would be allowed in the case, say, of an elastic membrane stretched between two rings to form a hollow cylinder, we give it mode number n=1, although it is suppressed. As will be seen later, higher odd modes are present.

In Figure A-3, we show the mode n=2. The perturbed radius is taken to be

$$r = a + \alpha \sin \frac{2\pi z}{\ell} \tag{A-1}$$

where α is small compared to a. The volume is

$$V = \int_0^{\ell} \pi r^2 dz = \pi a^2 \ell + 2\pi a\alpha \int_0^{\ell} \sin \frac{2\pi z}{\ell} dz + 0(\alpha^2) \tag{A-2}$$

Since the integral is zero, the volume is conserved at least to first order. For the even modes, in general, we may write the perturbed radius as

$$r = a + \alpha \sin \frac{n\pi z}{\ell}, \; n = 2, 4, 6, \text{etc.} \tag{A-3}$$

Next we calculate the potential energy, P, due to the increase of surface area S and the surface tension σ. The surface area is given by the integral

$$S = \int 2\pi r ds \tag{A-4}$$

where ds is an element of arc as shown in Figure A-3. Now

$$ds = (dz^2 + dr^2)^{1/2} = \left[1 + \left(\frac{dr}{dz}\right)^2\right]^{1/2} dz \qquad \text{(A-5)}$$

so, approximately,

$$ds = \left[1 + \tfrac{1}{2}\left(\frac{dr}{dz}\right)^2\right] dz \quad . \qquad \text{(A-6)}$$

Therefore the surface area is seen to be

$$S = 2\pi \int_0^{\ell} \left(a + \alpha \sin \frac{n\pi z}{\ell}\right)\left(1 + \frac{n^2\pi^2\alpha^2}{2\ell^2} \cos^2 \frac{n\pi z}{\ell}\right) dz \quad . \qquad \text{(A-7)}$$

Of the four terms in Equation (A-7) obtained by multiplying the binomials, only two have averages different from zero. Thus the surface area of the distorted shape is seen to be

$$S = 2\pi a\ell + \frac{n^2\pi^3 a\alpha^2}{2\ell} \qquad \text{(A-8)}$$

Evidently the first term is the unperturbed area, so we let that correspond to the zero of potential energy and find the change about this reference

$$P = \frac{\sigma n^2 \pi^3 a}{2\ell} \alpha^2 \quad . \qquad \text{(A-9)}$$

The next phase of the problem is to calculate the kinetic energy associated with the vibration, and to do this we have to find the radial and axial velocities, v_r and v_z. To do this, we introduce a velocity potential in the form:

$$\varphi = \beta \sin \frac{n\pi z}{\ell} \; I_0\left(\frac{n\pi r}{\ell}\right) \qquad \text{(A-10)}$$

where I_0 is the Bessel function of imaginary argument.

This leads to velocities

$$v_r = \frac{\partial \varphi}{\partial r} = \frac{n\pi}{\ell} \beta \sin \frac{n\pi z}{\ell} \; I_1 \left(\frac{n\pi r}{\ell} \right) \qquad \text{(A-11)}$$

$$v_z = \frac{\partial \varphi}{\partial z} = \frac{n\pi}{\ell} \beta \cos \frac{n\pi z}{\ell} \; I_0 \left(\frac{n\pi r}{\ell} \right) \qquad \text{(A-12)}$$

From Equation (A-11) we see that the radial velocity is zero at the top and bottom (z=0 and z=ℓ) but from Equation (A-12) we see that v_z is not zero at z=0 and z=ℓ. Therefore, the vertical velocity is not consistent with the appropriate boundary conditions and is incorrect. Since the cosine is unity at z=0 and z=ℓ, we try the velocity:

$$v_z = \frac{n\pi}{\ell} \beta \left(\cos \frac{n\pi z}{\ell} - 1 \right) I_0 \left(\frac{n\pi r}{\ell} \right) \qquad \text{(A-13)}$$

in place of Equation (A-12), so the boundary conditions are met. The only condition we have to satisfy, then, is continuity. That is:

$$\text{div } v = 0 \qquad \text{(A-14)}$$

Since

$$\text{div } v = \frac{1}{r} \frac{\partial}{\partial r} (r v_r) + \frac{\partial v_z}{\partial z} \qquad \text{(A-15)}$$

and

$$\frac{1}{r} \frac{d}{dr} \left[r I_1 \left(\frac{n\pi r}{\ell} \right) \right] = \frac{n\pi}{\ell} I_0 \left(\frac{n\pi r}{\ell} \right) \qquad \text{(A-16)}$$

(which is Bessel's equation), we see that Equation (A-14) is satisfied by the velocity as determined by Equations (A-11) and (A-13). In fact, the velocity can be derived from the stream function

$$\psi = \beta I_1 \left(\frac{n\pi r}{\ell} \right) \left(\cos \frac{n\pi z}{\ell} - 1 \right) \qquad \text{(A-17)}$$

with

$$v_r = -\frac{\partial \psi}{\partial z} \qquad \text{(A-18)}$$

and

$$v_z = \frac{1}{r} \frac{\partial}{\partial r} (r\psi) \qquad \text{(A-19)}$$

Next we calculate the velocity at the free surface in two ways to identify the quantity β. To begin with, differentiate Equation (A-3) with respect to time:

$$v_r(a) = \dot{\alpha} \sin \frac{n\pi z}{\ell} \tag{A-20}$$

and next substitute r=a in Equation (A-11):

$$v_r(a) = \frac{n\pi\beta}{\ell} I_1\left(\frac{n\pi a}{\ell}\right) \sin \frac{n\pi z}{\ell} \tag{A-21}$$

Therefore we see that

$$\dot{\alpha} = \frac{n\pi\beta}{\ell} I_1\left(\frac{n\pi a}{\ell}\right) \tag{A-22}$$

or

$$\beta = \frac{\ell}{n\pi I_1\left(\frac{n\pi a}{\ell}\right)} \dot{\alpha} \tag{A-23}$$

The kinetic energy is given by the integral

$$K = \int \tfrac{1}{2} \rho (v_r^2 + v_z^2)\, dV \tag{A-24}$$

taken over the volume of the fluid; in Equation (A-24) ρ is the density and dV is an element of volume. Substitution of Equations (A-11) and (A-13) into Equation (A-24) leads to the expression

$$K = \frac{n^2\pi^2\beta^2\rho}{2\ell^2} \int_0^a \int_0^{\ell} \left\{ I_1^2\left(\frac{n\pi r}{\ell}\right) \sin^2 \frac{n\pi z}{\ell} + I_0^2\left(\frac{n\pi r}{\ell}\right)\left(\cos^2 \frac{n\pi z}{\ell} - 2\cos\frac{n\pi z}{\ell} + 1\right)\right\} 2\pi r\, dr\, dz \tag{A-25}$$

The integration with respect to z is quite simple and leads to the expression

$$K = \frac{n^2\pi^3\beta^2\rho}{2\ell} \int_0^a \left[3 I_0^2\left(\frac{n\pi r}{\ell}\right) + I_1^2\left(\frac{n\pi r}{\ell}\right)\right] r\, dr \tag{A-26}$$

Although the functions in the integrand above are less familiar than sines and cosines, the integrals are easily evaluated from the formulas

$$\int x\, I_0^2(x)\, dx = \frac{x^2}{2}\, [I_0^2(x) - I_1^2(x)] + C \qquad \text{(A-27)}$$

and

$$\int x\, I_1^2(x)\, dx = x\, I_0(x)\, I_1(x) - \frac{x^2}{2}\, [I_0^2(x) - I_1^2(x)] + C \quad . \qquad \text{(A-28)}$$

These formulas and a bit of tedious manipulation show that

$$K = \frac{n\,\pi^2\,\beta^2\,\rho\,a}{2} \left\{ I_0(p)\, I_1(p) + p\, [I_0^2(p) - I_1^2(p)] \right\} \qquad \text{(A-29)}$$

where we have written

$$p = \frac{n\pi a}{\ell} \qquad \text{(A-30)}$$

for short. After substituting the value of β from Equation (A-23) into the expression for kinetic energy, we find:

$$K = \frac{\rho\, a\, \ell^2}{2n} \left[\frac{I_0(p)}{I_1(p)} + p \left(\frac{I_0^2(p)}{I_1^2(p)} - 1 \right) \right] \dot{\alpha}^2 \qquad \text{(A-31)}$$

In order to obtain the resonance frequencies we set

$$\alpha = \tilde{\alpha}\, e^{i\omega t} \qquad \text{(A-32)}$$

and appeal to the conservation of energy:

$$P + K = \text{const.} \qquad \text{(A-33)}$$

whence, from Equations (A-9), (A-31) and (A-32):

$$\left[\frac{\sigma\, n^2 \pi^3\, a}{2\ell} - \frac{\omega^2 \rho\, a\, \ell^2}{2n}\, u\left(\frac{n\pi a}{\ell} \right) \right] \tilde{\alpha}^2\, e^{2i\omega t} = \text{const} \qquad \text{(A-34)}$$

where

$$u(p) = \frac{I_0(p)}{I_1(p)} + p\left(\frac{I_0^2(p)}{I_1^2(p)} - 1\right) \quad . \tag{A-35}$$

Equation (A-34) can be satisfied only if the coefficient of the time-dependent term is zero, so we obtain the result

$$\omega^2 = \frac{n^3\pi^3\sigma}{\rho\,\ell^3\,u\left(\frac{n\pi a}{\ell}\right)} \quad . \tag{A-36}$$

The function u(p) can be evaluated for moderate values of p by reference to tables of Bessel functions. Beyond that point the function can be evaluated approximately by means of asymptotic expansions of I_0 and I_1:

$$I_0(p) \sim \frac{e^p}{\sqrt{2\pi p}}\left(1 + \frac{1}{8p} + \frac{9}{128p^2} \cdots\right) \tag{A-37}$$

$$I_1(p) \sim \frac{e^p}{\sqrt{2\pi p}}\left(1 - \frac{3}{8p} - \frac{15}{128p^2} \cdots\right) \tag{A-38}$$

By long division we find

$$\frac{I_0(p)}{I_1(p)} \sim 1 + \frac{1}{2p} + \frac{3}{8p^2} \cdots \tag{A-39}$$

So we find

$$u(p) \sim 2 + \frac{3}{2p} \tag{A-40}$$

At p=10, for example, the exact value of u is 2.167 · · ·, while the asymptotic expression gives 2.150; the error is about 0.8%, i.e., it is in the order of $1/p^2$. Some useful values of u(p) are given in Table A-1.

Another way to put Equation (A-36) which corresponds to the manner in which the experimental results are organized is:

$$\frac{\sigma}{\rho \ell^3 \omega^2} = \frac{1}{n^3 \pi^3} \; u\left(\frac{n\pi a}{\ell}\right) \tag{A-41}$$

The analysis of the odd modes is not so easy as the analysis of the even modes because the mode shape cannot be simply sinusoidal or the volume would not be constant throughout the motion.

At this juncture it is best to redefine the z-coordinate so that the origin is at the center of the fluid zone, which now is limited at $z = \pm \ell/2$. As a result of this change, the roles of sines and cosines are reversed, but the additional symmetry makes the algebra significantly simpler.

In this case we may start with the stream function:

$$\psi = \beta I_1\left(\frac{n\pi r}{\ell}\right)\left(\mu \sin \frac{n\pi z}{\ell} + a_3 z^3 + a_1 z\right) . \tag{A-42}$$

Here the coefficients a_3 and a_1 are to be determined to satisfy the boundary conditions and conserve mass, while the coefficient μ is defined as follows:

$$\mu = +1 \quad \text{for} \quad n = 3, 7, 11. \ldots \tag{A-43}$$

$$\mu = -1 \quad \text{for} \quad n = 5, 9, 13, \ldots \tag{A-44}$$

This is done so that $\mu \sin \frac{n\pi}{2} = -1$ for all odd values of n; otherwise the two sets of odd numbers would have to be treated separately.

As before we take

$$v_r = -\frac{\partial \psi}{\partial z} = -\frac{n\pi\beta}{\ell} \; I_1\left(\frac{n\pi r}{\ell}\right) \left(\mu \cos \frac{n\pi z}{\ell} + \frac{3\ell a_3}{n\pi} z^2 + \frac{\ell a_1}{n\pi}\right) . \tag{A-45}$$

The boundary condition to be imposed is $v_r\left(z = \pm \frac{\ell}{2}\right) = 0$. Since $\cos \frac{n\pi}{2} = 0$, we must have

$$\frac{3\ell^3}{4n\pi} a_3 + \frac{\ell a_1}{n\pi} = 0 \quad , \tag{A-46}$$

or

$$a_1 = -\frac{3\ell^2 a_3}{4} \tag{A-47}$$

which result can be substituted into the stream function to yield

$$\psi = \beta I_1\left(\frac{n\pi r}{\ell}\right)\left(\mu \sin \frac{n\pi z}{\ell} + a_3 \left[z^3 - \frac{3\ell^2 z}{4}\right]\right) \quad . \tag{A-48}$$

Next we consider v_z:

$$v_z = \frac{1}{r} \frac{\partial}{\partial r} (r\psi) = \frac{n\pi\beta}{\ell} I_0\left(\frac{n\pi r}{\ell}\right)\left(\mu \sin \frac{n\pi z}{\ell} + a_3 \left[z^3 - \frac{3\ell^2 z}{4}\right]\right) \tag{A-49}$$

Again the boundary condition is such that $v_z \left(z = \pm \frac{\ell}{2}\right) = 0$. So we require that

$$-1 + a_3 \left[\frac{\ell^3}{8} - \frac{3\ell^3}{8}\right] = 0 \quad , \tag{A-50}$$

or

$$a_3 = -\frac{4}{\ell^3} \quad . \tag{A-51}$$

Finally, therefore, the stream function and components of velocity are found to be

$$\psi = \beta I_1 \left(\frac{n\pi r}{\ell}\right) \left(\mu \sin \frac{n\pi z}{\ell} - \frac{4z^3}{\ell^3} + \frac{3z}{\ell}\right) \tag{A-52}$$

$$v_r = -\frac{\partial \psi}{\partial z} = -\frac{n\pi\beta}{\ell} I_1\left(\frac{n\pi r}{\ell}\right)\left(\mu \cos\frac{n\pi z}{\ell} - \frac{12z^2}{n\pi\ell^2} + \frac{3}{n\pi}\right) \quad \text{(A-53)}$$

$$v_z = \frac{1}{r}\frac{\partial}{\partial r}(r\psi) = \frac{n\pi\beta}{\ell} I_0\left(\frac{n\pi r}{\ell}\right)\left(\mu \sin\frac{n\pi z}{\ell} - \frac{4z^3}{\ell^3} + \frac{3z}{\ell}\right) . \quad \text{(A-54)}$$

The mode shape must have the same dependence on z as v_r. Therefore we write the mode shape as

$$r = a + \alpha \left(\mu \cos\frac{n\pi z}{\ell} - \frac{12z^2}{n\pi\ell^2} + \frac{3}{n\pi}\right) \quad \text{(A-55)}$$

An illustration of the mode shape for n=3 is given in Figure A-4. The volume is then given by the integral

$$V = \int_{-\ell/2}^{\ell/2} \pi r^2 dz = \pi a^2 \ell + 4\pi a\alpha \int_0^{\ell/2} \left(\mu \cos\frac{n\pi z}{\ell} - \frac{12z^2}{n\pi\ell^2} + \frac{3}{n\pi}\right) dz . \quad \text{(A-56)}$$

But

$$\int_0^{\ell/2} \left(\mu \cos\frac{n\pi z}{\ell} - \frac{12z^2}{n\pi\ell^2} + \frac{3}{n\pi}\right) dz = \frac{\ell}{n\pi}\left[\mu \sin\frac{n\pi z}{\ell} - \frac{4z^3}{\ell^3} + \frac{3z}{\ell}\right]_0^{\ell/2} = 0 \quad \text{(A-57)}$$

so the volume is conserved, again to first order.

To compute the potential energy we start by calculating the change in surface area ΔS from the formula

$$\Delta S = \int_{-\ell/2}^{\ell/2} 2\pi r \left[1 + \frac{1}{2}\left(\frac{dr}{dz}\right)^2\right] dz - 2\pi a\ell \quad \text{(A-58)}$$

The term that is linear in α involves the same integral as in Equation (A-57) and is therefore zero. We see, then, that

$$\Delta S = 2\pi a \alpha^2 \int_0^{\ell/2} \left(\mu \frac{n\pi}{\ell} \sin \frac{n\pi z}{\ell} + \frac{24z}{n\pi \ell^2} \right)^2 dz \qquad \text{(A-59)}$$

or

$$\Delta S = \frac{2\pi a \alpha^2}{\ell} \left(\frac{n^2\pi^2}{4} - \frac{24}{n^2\pi^2} \right) \qquad \text{(A-60)}$$

which leads to the result that the potential energy P is:

$$P = \frac{n^2\pi^3 a \alpha^2 \sigma}{2\ell} \left(1 - \frac{96}{n^4\pi^4} \right) \qquad \text{(A-61)}$$

which is nearly the same as it was in the case of the even modes – see Equation (A-9).

The task of calculating the kinetic energy K is more formidable. We start from the basic definition

$$K = \int_0^a \int_{-\ell/2}^{\ell/2} \frac{1}{2} \rho \left(v_r^2 + v_z^2 \right) \cdot 2\pi r \, dr \, dz \quad . \qquad \text{(A-62)}$$

On account of the symmetry, we may write:

$$K = 2\pi\rho \int_0^a \int_0^{\ell/2} \left(v_r^2 + v_z^2 \right) r \, dr \, dz \qquad \text{(A-63)}$$

whence

$$K = \frac{2\pi\rho n^2\pi^2\beta^2}{\ell^2} \left\{ \int_0^a r I_1^2 \left(\frac{n\pi r}{\ell} \right) dr \cdot \int_0^{\ell/2} \left(\mu \cos \frac{n\pi z}{\ell} - \frac{12z^2}{n\pi\ell^2} + \frac{3}{n\pi} \right)^2 dz \right.$$

$$\left. + \int_0^a r I_0^2 \left(\frac{n\pi r}{\ell} \right) dr \cdot \int_0^{\ell/2} \left(\mu \sin \frac{n\pi z}{\ell} - \frac{4z^3}{\ell^3} + \frac{3z}{\ell} \right)^2 dz \right\} \quad . \qquad \text{(A-64)}$$

We perform the integrations with respect to z first and discovery, by much effort, that

$$K = \frac{n^2\pi^3\rho\beta^2}{2\ell}\left\{2\left(\frac{69}{70} - \frac{96}{n^4\pi^4}\right)\int_0^a r I_0^2\left(\frac{n\pi r}{\ell}\right)\,dr + \left(1 + \frac{48}{5n^2\pi^2} - \frac{192}{n^4\pi^4}\right)\int_0^a r I_1^2\left(\frac{n\pi r}{\ell}\right)\,dr\right\} . \quad \text{(A-65)}$$

It is instructive to compare this with Equation (A-26), which gives the kinetic energy for the even modes. In that case the coefficients of I_0^2 and I_1^2 are 3 and 1, respectively, whereas here they are approximately 2 and 1. The integrals of the Bessel functions can now be carried out just as in the previous case so we obtain the result:

$$K = \frac{n\pi^2\beta^2\rho a}{2}\left\{C_1 I_0(p)I_1(p) + \frac{C_2 p}{2}\left[I_0^2(p) - I_1^2(p)\right]\right\} \quad \text{(A-66)}$$

where $p = n\pi a/\ell$ as before and the constants C_1 and C_2 (both nearly unity) are:

$$C_1 = 1 + \frac{48}{5n^2\pi^2} - \frac{192}{n^4\pi^4} \quad \text{(A-67)}$$

$$C_2 = \frac{34}{35} - \frac{48}{5n^2\pi^2} . \quad \text{(A-68)}$$

The expression for β^2 is unchanged – see Equation (A-23) – and consequently

$$K = \frac{\rho a\ell^2}{2n}\left[C_1\frac{I_0(p)}{I_1(p)} + \frac{C_2 p}{2}\left(\frac{I_0^2(p)}{I_1^2(p)} - 1\right)\right]\dot{\alpha}^2 . \quad \text{(A-69)}$$

Finally, from the principle of conservation of energy, we obtain the resonance frequencies as

$$\omega^2 = \frac{n^3\pi^3\sigma}{\rho\ell^3 v\left(\frac{n\pi a}{\ell}\right)} \quad \text{(A-70)}$$

$$\text{where } v(p) = \frac{C_1 \frac{I_0(p)}{I_1(p)} + \frac{C_2 p}{2}\left[\frac{I_0^2(p)}{I_1^2(p)} - 1\right]}{1 - \frac{96}{n^4\pi^4}} \simeq \frac{I_0(p)}{I_1(p)} + \frac{p}{2}\left[\frac{I_0^2(p)}{I_1^2(p)} - 1\right] \qquad \text{(A-71)}$$

This result may be expressed in the alternative form

$$\frac{\sigma}{\rho \ell^3 \omega^2} = \frac{1}{n^3\pi^3} \; v\left(\frac{n\pi a}{\ell}\right) \quad . \qquad \text{(A-72)}$$

Table A-2 gives values of the function v(p) calculated from the approximate form of Equation (A-71).

TABLE A-1

p	u(p)
$\pi/2$	4.239
$2\pi/3$	3.432
π	2.751
$4\pi/3$	2.489
2π	2.287
4π	2.130
8π	$\sim$ 2.060

$$\text{The function } u(p) = \frac{I_0(p)}{I_1(p)} + p\left(\frac{I_0^2(p)}{I_1^2(p)} - 1\right)$$

TABLE A-2

p	v(p)
$\pi/2$	2.898
$2\pi/3$	2.396
π	1.979
2π	1.689
4π	1.586
8π	1.541

$$\text{The function } v(p) \simeq \frac{I_0(p)}{I_1(p)} + \frac{p}{2}\left(\frac{I_0^2(p)}{I_1^2(p)} - 1\right)$$

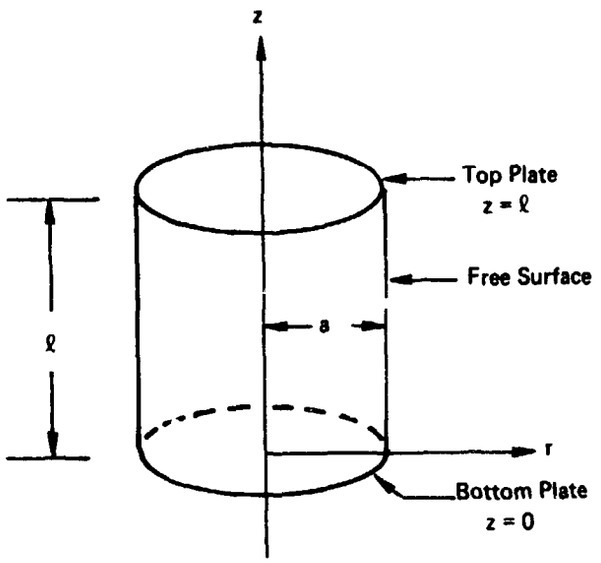

FIGURE A–1 CYLINDER OF FLUID SUSPENDED BETWEEN RIGID CIRCULAR PLATES

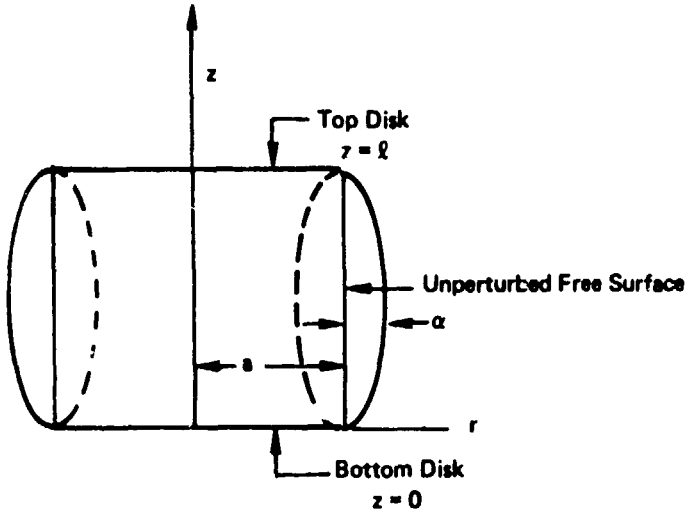

FIGURE A–2 THE SHAPE OF THE MODE n = 1 DOES NOT CONSERVE VOLUME

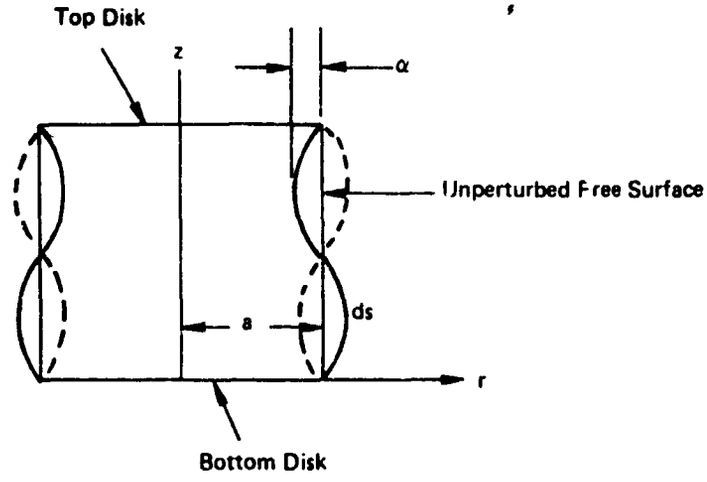

FIGURE A–3 THE SHAPE OF THE MODE CORRESPONDING TO n = 2

PART II

TABLE OF CONTENTS – PART II

		Page
List of Tables		68
List of Figures		69
ABSTRACT		71
I.	INTRODUCTION	72
II.	REVIEW OF PRIOR FLOW VISUALIZATION STUDIES	73
III.	DESCRIPTION OF EXPERIMENTS	74
IV.	RESULTS	77
V.	CONCLUSIONS AND RECOMMENDATIONS	83
REFERENCES		84
APPENDIX A –	DESIGN CONSIDERATIONS FOR A STEREOPTICAL SYSTEM AND A METHOD FOR TAKING VELOCITY MEASUREMENTS	103
APPENDIX B –	CALCULATION OF PARTICLE POSITION AND VELOCITY	113

LIST OF TABLES – PART II

Table No.		Page
1	Test Conditions for the Flow Survey	85
2	Properties of Fluids Used	86
3	Calculated Values of Particle Positions and Velocity for Isorotation at 2.0 Rev/Sec	86
4	Results of Error Analysis of Selected Particles, Based on a Value of the Maximum Uncertainty in the Position on the Negatives of ± .00038 cm	87
5	Calculated Values of Particle Positions and Velocity for Equal Counterrotation at 2.5 Rev/Sec	88

LIST OF FIGURES – PART II

Figure No.		Page
1	Experimental Set-up for Investigation of Flow Within Floating Zones	89
2	Effect of Fixed Angular Velocity on $\frac{\Delta}{h}$ as a Function of Angular Velocity Ratio	90
3	Reproducibility of the Measurement of $\frac{\Delta}{h}$ as a Function of Angular Velocity Ratio	91
4	Effect of Bond Number on $\frac{\Delta}{h}$ as a Function of Angular Velocity Ratio	92
5	Effect of Weber Number on $\frac{\Delta}{h}$ as a Function of Angular Velocity Ratio, at a Constant Reynolds Number	93
6	Effect of Reynolds Number on $\frac{\Delta}{h}$ as a Function of Angular Velocity Ratio, at a Constant Weber Number	94
7	$\frac{\Delta}{h}$ as a Function of Angular Velocity Ratio for Conditions Approaching the 1st C-Mode Instability	95
8	Plot of $\nabla .65$ as a Function of Reynolds and Weber Numbers for Tests 1, 2, 3, 4, 6, 7, 9, 10, 12, 13, 14, 15, 16, 20, 21, 22, 23, and 24	96
9	Plot of $\nabla .65$ as a Function of Reynolds and Weber Numbers for Tests 4, 5, 8, 11, 17, 18, 19, 20, 22, 23, and 24	97
10	One of a Stereopair of Photographs for Isorotation at 2.0 Rev/Sec	98
11	Photograph Used to Measure the Shape of the Free Surface of the Column	99
12	Plot of Calculated Values of Particle Position for Isorotation at 2.0 Rev/Sec	100
13	Plot of Calculated Values of Particle Position for Equal Counterrotation at 2.5 Rev/Sec	101

EXPERIMENTAL STUDY OF THE STABILITY AND FLOW CHARACTERISTICS OF FLOATING LIQUID COLUMNS CONFINED BETWEEN ROTATING DISKS

ABSTRACT — PART II

A technique for the quantitative measurement of stream velocity within a floating, isothermal, liquid column confined between rotatable disks has been developed. In the measurement, small, light-scattering particles were used as streamline markers in common arrangement, but the capability of the measurement was extended by use of a stereopair photography system to provide quantitative data. Results of velocity measurements made under a few selected conditions, which established the precision and accuracy of the technique, are reported. The general qualitative features of the isothermal flow patterns under various conditions of end-face rotation resulting from both still photography and motion pictures are reported. Also the outstanding qualitative features of the flow patterns for liquid columns at low Bond numbers under counter-rotational conditions, which may be of special interest to the development of a scientific understanding of the float-zone crystal-growth process, are examined in more detail.

I. INTRODUCTION

An accurate quantitative description of the mass, momentum, and heat transfer within the molten zone of a floating-zone, crystal-growth process is necessary to the full scientific understanding of this process. This understanding is a prerequisite for advancing the present technology which is based on a patchwork of empiricism and partial theory. In recent theoretical and experimental work, mainly under the sponsorship of United States and European space programs, this need has been recognized, and these programs have added greatly to the state of knowledge. However, there is now almost no quantitative test data on the behavior of floating zone systems of interest to the manufacturer of crystal materials, and a check between developing theory and experiment has yet to be accomplished.

The purpose of the work described in Part II of this study was to provide:

1. Experimental observations of the flow within floating zones of value to the quest for a better scientific understanding of the float zone process, and
2. A method for measuring velocity within floating zone configurations which can be used to obtain a data base against which developing predictive methods can be tested and improved.

The work simulates approximately the low-gravity condition by employing models of small geometric scale.

II. REVIEW OF PRIOR FLOW VISUALIZATION STUDIES

A number of investigators have carried out experiments especially devised to observe the flow within floating zones under conditions of interest to the materials processing community. Carruthers and Grasso[1] made qualitative observations of rotating liquid columns using dye markers in a plateau-type simulation of low-gravity conditions, as described in Part I. As noted, this method of simulation gave rise to a spurious viscous shear condition at the free surface of the column which significantly altered the observed circulation within the column from that which would be present with a typical liquid/gas boundary. Furthermore, the patterns observed were subject to distortion caused by refraction at the interface of the water-ethanol mixture and nujol, as well as the walls of the tank which made their interpretation imprecise.

Chun and Wuest[2][3][4] have reported a number of useful experiments in which they observed the flow patterns within small liquid columns of water, alcohol, and silicone oil with heating and end-face rotation using optical/particle tracer and low Bond number simulation techniques. They used an optical system which illuminated the meridian plane with a sheet of light. With this method, they obtained an uncomplicated picture of the axial and radial velocity field universal to the axi-symmetric case of rotation, but no information about the tangential components of velocity and inadequate information about possible velocity fields that do not have axial symmetry.

Schwabe et al.[5][6][7] have reported somewhat similar experiments in which they observed the flow patterns within small liquid columns of $NaNO_3$ made visible by the paths of bubbles induced at sufficiently low pressure. Only qualitative visual observations of the flow patterns were reported.

As a precursor to this work, Fowle et al.[8][9] also used low Bond number simulations to observe the behavior of floating liquid columns, using the apparatus described briefly in Part I. In this earlier work, dark field illumination of small, polystyrene tracer particles was used successfully for qualitative flow observations, but the low reflectivity of these particles limited their utility to observation of low particle velocities. Also the basic concept for making quantitative velocity measurements using a pulsed flash source and stereopair photography and the refinements necessary to develop it to a workable technique were defined.

III. DESCRIPTION OF EXPERIMENTS

Flow Survey

The experimental apparatus and techniques reported in Part I were used to survey the more general and obvious characteristics of the flow within a floating liquid column induced by counterrotating end-faces. One of the flow features which was extensively studied was the effect of the velocity ratio of the top and bottom end-faces on the position of the surface of separation between Proudman-Taylor cells associated with these end-faces, because this relatively obvious feature could provide a simple test of developing predictive analyses.

Tests were performed with distilled water and Dow Corning 200 series silicone fluids. The viscosities of the silicone fluids were 3, 5 and 10 centistokes. Nickel-coated, neutrally buoyant, hollow-glass spheres of 35-μm radius were used as flow-tracking particles. A binocular microscope with a calibrated eyepiece was used for observation and geometrical measurement.

The procedure used in making these measurements was to maintain the angular velocity of one of the end-faces constant, while increasing the angular velocity of the other end-face above that held constant. The minimum value of the velocity ratio for which data were obtained was the value for which the position of the plane of separation became indistinguishedly near to the slower end-face, at which point the C-mode instability first occurred, or when limited by the rotational speed of the motors.

As reported in Part I and in previous work,[6] surface swirls occur within cylindrical columns having end-faces that are counterrotating at sufficiently high rates. These vortices appear at the plane of separation between the Proudman-Taylor cells associated with the upper and lower end-faces and have vortex lines radially directed at the surface. Further observations of the flow circumstances resulting in these swirls were made, using water as a test fluid for columns having radii of 0.254 and 0.127 cm. Both nickel-coated, hollow glass spheres and lycopodium powder (Sargent Welch item no. SC13245-102) were used to decorate the swirls.

The position of the surface of separation of the Proudman-Taylor cells was identified with the location of a zero tangential component of velocity at the surface, as revealed by particle motion on the surface of the liquid column. For rotational conditions sufficiently high for surface swirls to occur, the position of the center of the surface swirls was used.

It is important to note that the identification of the plane of separation of the Proudman-Taylor cells, with a condition of zero tangential velocity at the surface, is not necessarily rigorous. This condition was chosen because it was visually obvious and apparently corresponded to the surface separating the cells, as revealed by the division between upward- and downward-directed axial velocity components. However, because of the uncertainties associated with the observation, it was not absolutely clear that the condition of zero tangential velocity at the surface corresponded identically with the condition of zero axial velocity, or even that the condition of zero axial velocity was precisely at a plane perpendicular to the rotational axis. This issue can be resolved by more tests using the quantitative technique for velocity field mapping described next.

The conditions tested are summarized in Table 1, and the fluid properties used in the reduction of the experimental data are summarized in Table 2.

Velocity Measurements

The primary objective of the velocity-measurement work was to improve the existing technique for flow visualization using tracer particles, to enable the quantitative measurement of position and velocity within rotating, floating liquid columns. To accomplish this, the following five tasks were undertaken:

1. The improvement of the light-scattering characteristic of the flow tracer particles. This was achieved by substituting nickel-plated, hollow glass spheres for the polystyrene spheres used in previous work. These particles were screened both for size and density. The particles were sieved to get a cut between 30- and 45-μm. Thereafter, this cut was screened for density by letting them settle in a column of water.

2. The modification of the design of the rods which serve as end-faces for the floating liquid column. The new design uses plexiglass rods, machined from optically polished plexiglass stock which has been inspected to ensure the parallelism of the two surfaces. This design allows for fine adjustment of the concentricity and perpendicularity of the rotating end-faces. Typical values of the total indicator readings for concentricity and perpendicularity are 0.0006 in. (0.0015 cm) and 0.00009 in. (0.0002 cm), respectively. These pieces can be easily changed and realigned in the event the end-faces get scratched.

3. Improvements in the electronic control of the stroboscopic xenon flash used to obtain successive exposures of the tracer particles. The xenon flash apparatus consisted of a modified General Radio Company Type 1531-A Strobotac. By means of external circuitry, the capacitance of the discharge capacitor in the Strobotac was increased from 1.15 to 17.15 farads at a charging potential of 800 volts, thus increasing the energy in the discharge to 5.45 joules. A control box attached to the Strobotac trigger input jack was made with circuitry such that a series of trigger pulses could be sent to the Strobotac. The maximum number of pulses allowed was 8, and any of the 8 pulses could be selectively omitted. The time interval between pulses could be varied from 5 milliseconds to 1 second. This control box also activated the camera motor drive. Opening a switch opened the camera shutter, and after a set time delay (to allow time for the damping of vibrations), the flash sequence took place. Then, by closing the switch the shutter was closed and the film was advanced.

4. The design of a stereoptical photographic system and method to measure the particle positions. A stereoscopic camera attachment, also known as a stereo reflector, was designed to enable a single camera to obtain a stero-pair of images simultaneously. The basic configuration adopted for the design of the stereo reflector consisted of a four-mirror arrangement very similar to that used in the Wheatstone stereoscope.[10]

5. The design of a position marker to be used in dark-field illumination for the alignment of the optical system. A length of glass optical waveguide, with a core diameter of 0.0020 cm attached to an x,y,z micropositioner, was used to create a point source of light, with known position with respect to the rotatable end-faces.

A photograph of the experimental apparatus is shown in Figure 1. The details of the design and operation of this system and of the data acquisition method are described in Appendix A. The analysis used to calculate the coordinates of a particle from its image location on a pair of stereophotographs is described in Appendix B.

IV. RESULTS

Flow Survey

The position (subject to the qualifications stated in Section III) of the surface separating the Proudman-Taylor cells associated with the top and bottom counterrotating end-faces was observed and recorded for the test conditions listed in Table 1.

Dimensional analysis was used to correlate and help interpret the results of the survey of the characteristics of the flow within floating columns when induced by counterrotating end-faces. The combined action of gravity, inertia, viscous and surface tension forces determines the velocity fields within the isothermal floating zone systems under study. Combining this knowledge with the application of dimensional analysis establishes a convenient set of six independent dimensionless variables which determine the flow field:

- Bond Number, $N_B = \frac{\rho g a_1 \ell}{\sigma}$
- Reynolds Number, $N_R = \frac{\rho a_1^2 \omega_1}{\mu}$
- Weber Number, $N_W = \frac{\rho a_1^3 \omega_1^2}{\sigma}$
- $\frac{a_2}{a_1}$
- $\frac{\ell}{a_1}$
- $\frac{\omega_1}{\omega_2}$

where:

σ = surface tension coefficient of the liquid (dyne/cm),

ρ = density of the liquid (g/cm^3),

μ = dynamic viscosity of the liquid (dyne-sec/cm^2),

g = gravitational constant (cm/sec^2),

ω_1 = angular velocity of lower end-face (rad/sec),

ω_2 = angular velocity of upper end-face (rad/sec),

ℓ = length of liquid column (cm),

a_1 = radius of liquid column at lower end-face (cm), and

a_2 = radius of liquid column at upper end-face (cm)

Flow behavior for only a limited set of the dimensionless moduli were investigated. The flow characteristics within a short cylinder ($\ell/a_i = 1$ and $a_1/a_2 = 1$) under conditions of counterrotation were examined in more detail than others. The short cylinder was chosen to reduce the relative distortion of the shape of the column due to the effects of gravity and, in addition, to provide an approximate low Bond number simulation of a lower gravity field acting on a larger prototype system. It follows that the position of the separating plane under the limiting conditions specified can be given by

$$\frac{\Delta}{h} = f(\frac{\omega_1}{\omega_2}, N_B, N_W, N_R)$$

where

Δ = distance of the flow-separating plane from the geometric midplane of the cylindrical column. By convention, Δ is positive for the flow-separating plane above the midplane and negative when it is below the midplane;

$h = \ell/2$ = half length (or half height) of the column.

Results of selected tests which are characteristic of all follow.

Figure 2 shows the results of tests 20 through 24 on the displacement of the flow-separating surface from the midplane of a water column having a radius of 0.127 cm and a half-height-to-radius ratio of 0.5, with the rotary speed of one end-face fixed at 1, 2, 5, 10, and 20 rev/sec. Δ/h is plotted versus the ratio of the fixed speed of one end-face to the varying speed of the other, which is greater and in counterrotation. The top half of the figure illustrates data obtained with the top end-face speed fixed; the bottom half illustrates results with the bottom end-face speed fixed. In either case, the plane of separation moved toward the end-face having the smaller rotary speed as the speed of one end-face was increased over the other. As the velocity ratio approached zero, $|\Delta/h|$ approached unity for low Bond number cases. Also the speed ratio corresponding to any selected non-zero value of Δ/h approached unity as the fixed speed increased. Because the test results shown in Figure 2 were all obtained at a relatively low Bond number, the displacements of the flow-separating surface were nearly symmetrical about the abscissa.

The uncertainty in the measurement of Δ/h was estimated to be ± 0.05, based on the smallest division of the rule in the microscope objective used in taking these measurements. Figure 3 shows results from two independent determinations of test number 16. The maximum difference between replicate point was 0.15; the average difference was 0.07.

The effect of increasing Bond number on the displacement of the flow-separating surface is illustrated in Figure 4. As the Bond number was increased, the static column increasingly distorted in the form of a Grecian urn, the position of the flow-separating surface at equal counterrotation was displaced upwards, and the pattern of Δ/h vs. angular velocity ratio became

increasingly unsymmetric. Also, at the same Bond number, the position of the flow-separating surface shifted monotomically upward with increasing equal counterrotation speed. For instance, in tests 16 through 19, Δ/h at $\omega_1/\omega_2 = 1.0$ increased from 0.1 to 0.4.

Figures 5 and 6 illustrate the displacement of the flow-separating surface with the decreasing angular velocity ratio that took place with an increase in Weber number at the same Reynolds number and with an increase in Reynolds number at the same Weber number, respectively.

For test number 8 on Figure 5 the surface of separation between Proudman-Taylor cells was uncharacteristically below the midplane. It was found that the rods used for this test had slightly different radii. The larger radius end-face was on top; the actual radius ratio was $a_2/a_1 = 1.02$. The larger radius at the top resulted in a greater pumping action of the top end-face in respect to the bottom and this, coupled with the change in the shape of the cylinder, drove the position of the surface of separation between cells toward the bottom end-face.

Figure 7 shows the progression of the position of the flow-separating surface with unequal counterrotation up to the onset of the first C-mode instability. The first C-mode occurred at the condition correlated by Equation (2) given in Part I, where the rotary velocity limit was that reached by either the top or bottom end-face.

In Figures 8 and 9, values of the arithmetic average of the angular velocity ratio for $|\Delta/h| = 0.65$ (this average value will be referred to as $\nabla_{.65}$), as measured in all tests in which h/a was 0.5, is plotted against the Reynolds and Weber numbers (based on the fixed and smaller end-face rotary speed) pertaining to each test. Figure 8 shows the values of all tests (1-24, except 1, 8, 11, 17, 18, and 19) for which the Reynolds number is less than 200 and the Weber number is less than 1.0. In Figure 9, the scale is changed to a maximum Reynolds number of 800 and maximum Weber number of 4.0 to show results for tests 1, 8, 11, 17, 18, and 19.

For the limiting set of circumstances, shown in Figures 8 and 9, the dimensionless functional relationship that applies reduces to:

$$\nabla_{.65}, \text{ angular velocity ratio} = f(N_R, N_W, N_B).$$

In these plots, the average values $\nabla_{.65}$ are used to reduce the influence of gravity on the result. Otherwise the separate influence of Bond number, which ranged between 0.109 and 0.436, have been neglected in this display. In any case the maximum difference between the values of the velocity ratio of corresponding to $\Delta/h = 0.65$ and $\Delta/h = -0.65$ was 9%, with the average difference being 4%. Accordingly, the assumption that the angular velocity ratio at a fixed value of h/a was a function of the Weber and Reynolds numbers only, which is inherent to the plot, is reasonable for the relatively low Bond number range tested.

Further Observations of Surface Swirls

For a column of water with end-face radii and height equal to 0.254 cm., the critical speed at which swirls first appeared under conditions of equal counterrotation was found to lie between 3.70 and 3.85 rev/sec. This range of speeds corresponds to a Reynolds number (based on the end-face radii) range of 150 to 156. The particular value in this range was found to be influenced by the shape of the column as dependent on the variations in zone volume that resulted from filling and evaporation. The lower value corresponded to the more obese columns.

Both three swirls at a 120-deg separation or two at a 180-deg separation were observed in this column for tests at Reynolds numbers ranging between 150 and 400, three swirls being the more stable state. For tests on a longer column (h/a = 0.75) made at Reynolds numbers between 150 and 400, the more stable state was found in the two swirls. At Reynolds numbers greater than approximately 400, the exact number of swirls could not be distinguished; at these high rotational speeds, the flows became visually confusing. Observations in which strobe illumination was used did not yield additional information.

For tests on a water column having end-face radii and a height of 0.127 cm, the onset of swirls occurred at equal counterrotation between 14.3 and 16.7 rev/sec. These speeds correspond to a Reynolds number range of 145 to 164. For this smaller zone, both the onset of swirls and the transition from the state of two to three swirls were more sensitively dependent on slight variations of the column shape than for the larger zone. Tests on this column and one having a h/a ratio of 0.75 gave similar results as regards the preferred number of swirls.

The centers of the swirls were observed to precess around the circumference of the column. The speed of precession was a function of the angular velocity ratio of the two end-faces. At a velocity ratio of unity, the center of the swirls do not precess, but remain fixed in space. As the speed of one of the end-faces was increased, keeping the other constant, the swirls moved toward the end-face having the smaller rotating speed; moreover, the precessing speed increased and was in the same direction as the rotation of the lower speed end-face. At a sufficiently high-speed ratio, the swirls collapsed as they encountered the Ekman layer next to the slower moving end-face.

Velocity Measurements

Velocity measurements for a column under conditions of isorotation were made in order to test the accuracy and precision of the technique on a well defined and understandable circumstance. Under these conditions, the fluid column rotates as a solid body; hence the particle pathlines are circles on a plane perpendicular to the axis of rotation and have tangential velocities proportional to radius.

Figure 10 is one of a pair of stereoscopic photographs of a water column of radius = 0.254 cm, height = 0.254 cm, under isorotation at 2.0 rev/sec. A six-flash sequence was used, with time intervals between successive flashes of .005, .005, .005, .015, and .005 second. Particle images used to obtain quantitative position and velocity data are identified. As discussed in Appendix A, direct visual interpretation of these photographs may be misleading for it is complicated by the effects of refraction at the liquid-air interface.

Figure 11 is one of a pair of stereoscopic photographs of the column shown in Figure 10, in which an incandescent lamp was used as a light source for an extended exposure (2 sec). From this photograph, the radius of the liquid column was determined as a function of the height, and these data were used to obtain a fourth-order polynomial expression of the column shape by a least squares fit executed by a computer program (as discussed in Appendix B). For this particular photograph, a typical case, the shape was described by the equation:

$$r = -1.064\,Z^4 + 4.142\,Z^3 - .1355\,Z^2 - .0667\,Z + .2576.$$

The standard deviation of the fit to the experimental data was 5 μm.

The positions of the particles identified in Figure 10 were calculated using a computer program based on the analysis described in Appendix B. Table 3 shows the calculated values of X, Y, Z, r, θ, and ω. Figure 12 is a plot of the particle positions in the X-Y plane. In this figure, arcs of radius equal to the mean value of r for all flash exposures of each particle are shown, as well as the standard deviation about the mean values. The standard deviation for these six particles ranged between 7 and 26 μm, the average value being 11 μm. The uncertainty intervals for X, Y, Z, r, and θ, calculated by error analysis (see Appendix B), are shown in Table 4. The average value of Δr calculated for these particles is $\pm$ 17 μm. Hence, the deviation of the particle positions from a circle is due to the propagation of the random error in the measurement of the particle positions on the negatives.

Note the proximity between particles number 1 and 2 on Figure 12. The average of the distance between these two particles for the four flash exposures was 54 $\pm 2\mu$m. The particles used in this experiment ranged in diameter from 30 to 45 μm. These two particles must then be clumped together. Computing the vector between these two particles indicated that the two particles were traveling as a dumbbell with its axis oriented almost parallel to the Z axis. This case serves to illustrate that the resolution of the photographs is better than 54 μm.

The mean of 19 measured values of ω is 1.95 rev/sec with a standard deviation of 0.14. This mean value is within 2.5% of the known value of 2.00 rev/sec.

Velocity measurements for a water column of radius = 0.254 cm, height = 0.254 cm, under equal counterrotation of 2.5 rev/sec were also made. This circumstance corresponds to test 14 (see Table 1). For this test, the rotary speed of the end-faces was below that necessary for swirls to appear and, therefore, an axisymmetric flow field was expected. A six-flash sequence was used, with time intervals between successive flashes of 0.020, 0.020, 0.020, 0.060 and 0.020 second. The calculated values of position and velocity are shown in Table 5. Figure 13 is a plot of the particle positions in the r-Z plane and in the X-Y plane.

The data presented in Figure 13 indicate that the flow follows a simple Proudman-Taylor cellular pattern. The particle path lines wrap on surfaces having the approximate form of toroids associated with the ring vortices induced by the top and bottom counterrotating end-faces. The dotted line shown is the position of the surface of separation between cells. Although the number of data points in the top cell is very limited, they are consistent with the cell pattern described and the cell separation plane shown.

Motion Picture Film

High-speed moving pictures were taken of the circulation within rotating, floating zones as revealed by the motion of tracer particles. A steady high-intensity halogen lamp in a dark-field arrangement and a 16 mm Ariflex camera operating at 45 frames per second were used for the filming. A bellows focusing attachment and a 105 mm focal length Micro-Nikon lens provided a magnification of 1.0. Kodak Tri-X reversal film was used.

The edited film runs for 20 minutes and shows a water column of 0.254-cm radius and 0.254-cm height under conditions of isorotation, single-end rotation, and counterrotation. Highlights of the film include:

- Part I first shows the column under isorotation at 2, 5, and 10 rev/sec.
- Then, starting at an isorotational rate of 20 rev/sec, the speed of isorotation was increased up to failure in the first C-mode at 43 rev/sec.
- Part II shows the circulation patterns with top-end rotation of 2 and 10 rev/sec, followed by a sequence starting with the column at rest and gradually increasing the speed of the top-end through the first C-mode up to failure at the 2nd C-mode.
- Part III shows results for equal counterrotation at 2, 5, and 10 rev/sec. At 5 and 10 rev/sec surface swirls are present. The next segment shows the column at equal counterrotation starting at 20 rev/sec and thereafter with gradually increasing speeds up to the maximum speed of the motors (45 rev/sec). Under these conditions the column does not fail.

The last four segments of the film show the circulation patterns with unequal counterrotation:

- First, with the bottom-end rotating at 2 rev/sec and the top-end speed gradually increasing from 2 to 20 rev/sec, then decreasing to 2 rev/sec.
- A second segment shows the counterpart with the top-end fixed at 2 rev/sec and the bottom end varying from 2 to 20 rev/sec and then back to 2 rev/sec. These conditions nearly correspond to those of test 13 of the flow survey (see Table 1).
- The conditions shown on the last two segments of the film correspond exactly to those of test 16 of the flow survey. For these conditions swirls are present and the film illustrates the characteristics of the swirls already discussed.

V. CONCLUSIONS AND RECOMMENDATIONS

A method for making quantitative measurements of the velocity distributions within small, floating columns of liquid using a low Bond number simulation of low-gravity conditions and optical-tracer particles has been developed to the status of proven utility. A survey of the flow fields in cylindrical, isothermal liquid columns induced by equal and unequal counterrotation of its end-faces has been made to provide a background of information for the further experimental and analytical investigations needed to make the float zone process fully understandable and predictable. The results of the flow survey revealed the general nature of flows that must be predicted by developing analytical constructions and, of particular interest, they showed the existence of three-dimensional flows in an axisymmetric geometry and driving condition.

The velocity measurement technique should now be applied more widely to the purposes for which it was developed. Until now, the theoretical predictions of the behavior of floating fluid zones and the experiments on them have not been tied together in a rigorous and unambiguous manner, due, in part, to the limitations of both. This situation should — and can — be rectified in a cooperative program of experimentation and theoretical analysis. The velocity measurement technique should be utilized to provide a data base against which the predictive methods being developed with NASA's support can be tested and improved in an interactive program.

Experimentation should be extended to the quantitative examination of flow fields within heated zones. Moreover, the present capabilities should be expanded by the development of a method for extracting the most amount of information on the flow field from photographic records of a limited number of particle streaks. The method for extrapolation and interpolation of velocity data on a few particles should incorporate the physical principles of conservation of mass and angular momentum that prevail and be implemented by computer calculation. Finally, minor modifications to the configuration and method of mounting the parts of the optical system should be made in order to make the measurement system easier to use in extensive application.

REFERENCES

1. Carruthers, J.R., and Grasso, M., "Studies of Floating Liquid Zones in Simulated Zero Gravity," J. Appl. Phys., Vol. 43, No. 2, 1972.

2. Chun, Ch.-H., and Wuest, W., "A Micro-gravity Simulation of the Marangoni Convection," Acta Astronautica, Vol. 5, 1978.

3. Chun, Ch.-H., and Wuest, W., "Experiments on the Transition from the Steady to the Oscillatory Marangoni Convection of a Floating Zone under Reduced Gravity Effect," IAF-78-202, presented at 29th I.A.F. Congress, Dubrovnik/Yugoslavia, 1979.

4. Chun, Ch.-H., and Wuest, W., "Flow Phenomena in Rotating Floating Zones with and without Marangoni Convection." 3rd European Symposium Materials Sciences in Space, ESA SP-142, 1979.

5. Schwabe, D., Scharmann, A., Presser, F., and Deder, R., "Experiments on Surface Tension Driven Flow in Floating Zone Melting," J. Crystal Growth, Vol. 43, 1978.

6. Schwabe, D., Scharmann, A., and Presser, F., "Steady and Oscillatory Marangoni Convection in Floating Zones under 1-g," 3rd European Symposium, Materials Sciences in Space, ESA SP-142, 1979.

7. Schwabe, D., and Scharmann, A., "Some Evidence for the Existence and Magnitude of a Critical Marangoni Number for the Onset of Oscillatory Flow in Crystal Growth Melts," J. Crystal Growth, Vol. 46, 1979.

8. Fowle, A.A., et al., "Float-Zone Processing in a Weightless Environment," NASA CR-2768, 1976.

9. Fowle, A.A., Wang, C.A., and Strong, P.F., "Experiments on the Stability of Conical and Cylindrical Liquid Columns at Low Bond Numbers," 3rd European Symposium, Materials in Space, ESA SP-142, 1979.

10. *Applied Optics and Optical Engineering* (Kingslake, R., Ed.), Academic Press, Vol. II, 1965, p. 89.

TABLE 1

TEST CONDITIONS FOR THE FLOW SURVEY

Test No.	Fluid	a (cm)	h/a	ω fixed (rev/sec)	N_B (based on ω fixed)	N_W (based on ω fixed)	N_R (based on ω fixed)
1	Silicone Oil (3 C.S.)	.127	.50	3	.369	.034	10.1
2	Silicone Oil (3 C.S.)	.127	.50	6	.369	.136	20.3
3	Silicone Oil (3 C.S.)	.127	.50	10.8	.369	.444	36.6
4	Silicone Oil (3 C.S.)	.127	.50	15	.369	.850	50.7
5	Silicone Oil (3 C.S.)	.127	.50	30	.369	3.40	101.0
6	Silicone Oil (5 C.S.)	.127	.50	5	.369	.094	10.1
7	Silicone Oil (5 C.S.)	.127	.50	10	.369	.378	20.3
8	Silicone Oil (5 C.S.)	.127	.50	25	.369	2.36	50.7
9	Silicone Oil (10 C.S.)	.127	.50	5	.370	.094	5.07
10	Silicone Oil (10 C.S.)	.127	.50	10	.370	.378	10.1
11	Silicone Oil (10 C.S.)	.127	.50	20	.370	1.51	20.3
12	Water	.254	.50	1.25	.436	.0111	50.7
13	Water	.254	.50	1.77	.436	.0278	71.7
14	Water	.254	.50	2.50	.436	.0555	101.0
15	Water	.254	.50	3.54	.436	.111	143.0
16	Water	.254	.50	5.00	.436	.222	203.0
17	Water	.254	.50	7.07	.436	.444	287.0
18	Water	.254	.50	10.00	.436	.888	405.0
19	Water	.254	.50	20.00	.436	3.55	810.0
20	Water	.127	.50	1	.109	.00111	10.1
21	Water	.127	.50	2	.109	.00444	20.3
22	Water	.127	.50	5	.109	.0278	50.7
23	Water	.127	.50	10	.109	.111	101.0
24	Water	.127	.50	20	.109	.444	203.0
25	Water	.127	.75	1	.163	.00111	10.1
26	Water	.127	.75	2	.163	.00444	20.3
27	Water	.127	.75	5	.163	.0278	50.7
28	Water	.127	.75	10	.163	.111	101.0
29	Water	.127	.75	20	.163	.444	20.3
30	Water	.127	1.00	1	.218	.00111	10.1
31	Water	.127	1.00	2	.218	.00444	20.3
32	Water	.127	1.00	5	.218	.0278	50.7
33	Water	.127	1.00	10	.218	.111	101.0
34	Water	.127	1.00	20	.218	.444	203.0
35	Water	.254	.75	2	.653	.0356	81.0

TABLE 2

PROPERTIES OF FLUIDS USED*

Fluid	Density (g/cc)	Viscosity		Surface Tension (dyne/cm)
		Kinematic (c.s.)	Dynamic (dyne-sec/cm^2)	
Distilled Water	1.00	1	0.010	72.6
Silicone Fluid	0.90	3	0.027	19.2
	0.92	5	0.046	19.7
	0.94	10	0.094	20.1

*These are nominal values at 20°C. The assumption that the liquid column is isothermal at this temperature is reasonable, for the accuracy to which calculated values of N_R, N_W and N_B are reported in Table 1.

TABLE 3

CALCULATED VALUES OF PARTICLE POSITIONS AND VELOCITY FOR ISOROTATION AT 2.0 REV/SEC

Particle No. Flash Sequence	X (cm)	Y (cm)	Z (cm)	r (cm)	θ Degrees	ω (rev/sec)
1-1	-.0424	.1158	-.0082	.1234	110.11	–
1-2	-.0348	.1171	-.0082	.1222	106.56	1.97
1-3	-.0277	.1200	-.0081	.1231	103.01	1.97
1-4	-.0203	.1224	-.0081	.1241	99.39	2.01
2-1	-.0406	.1153	-.0133	.1223	109.42	–
2-2	-.0334	.1165	-.0133	.1212	106.00	1.90
2-3	-.0284	.1178	-.0133	.1207	102.64	1.87
2-4	-.0192	.1209	-.0132	.1224	99.03	2.00
3-1	-.0123	-.1410	.0404	.1416	264.99	–
3-2	-.0203	-.1383	.0404	.1398	261.66	1.85
3-3	-.0286	-.1378	.0404	.1407	258.28	1.88
3-4	-.0364	-.1359	.0404	.1407	255.01	1.82
4-1	.0561	-.1130	.0860	.1261	296.39	–
4-2	.0491	-.1196	.0860	.1293	292.32	2.26
4-3	.0419	-.1210	.0860	.1281	289.09	1.79
4-4	.0348	-.1224	.0860	.1272	285.85	1.80
4-5	.0116	-.1287	.0361	.1292	275.13	1.98
5-1	.1246	-.1705	.0441	.2111	306.15	–
5-2	.1140	-.1825	.0440	.2152	301.99	2.30
5-3	.1027	-.1872	.0440	.2135	298.75	1.80
5-4	.0914	-.1969	.0440	.2171	294.92	2.13
6-1	.0464	.2542	-.0920	.2584	280.34	–
6-2	.0311	-.2587	-.0920	.2606	276.86	1.93
6-3	.0161	-.2600	-.0919	.2606	273.56	1.84
6-4	.0003	-.2614	-.0919	.2614	270.08	1.93

TABLE 4

RESULTS OF ERROR ANALYSIS OF SELECTED PARTICLES, BASED ON A VALUE OF THE MAXIMUM UNCERTAINTY IN THE POSITION ON THE NEGATIVES OF ± .00038 CM

Particle	ΔX (cm)	ΔY (cm)	ΔZ (cm)	Δr (cm)	$\Delta\theta$ (Deg)
1-1	.0002	.0009	.0003	.0008	.19
3-1	.0003	.0017	.0003	.0017	.13
4-4	.0003	.0017	.0003	.0016	.22
5-4	.0004	.0021	.0003	.0020	.20
6-1	.0004	.0022	.0003	.0022	.10
Mean	.0003	.0017	.0003	.0017	.17

TABLE 5

CALCULATED VALUES OF PARTICLE POSITIONS AND VELOCITY FOR EQUAL COUNTERROTATION AT 2.5 REV/SEC

Particle No. — Flash Sequence	X (cm)	Y (cm)	Z (cm)	r (cm)	θ (deg)	ω (rad/sec)	V_r (cm/sec)	V_θ (cm/sec)	V_Z (cm/sec)	|V| (cm/sec)
1-1	-0.0311	-0.0269	0.0546	0.0411	220.87	-4.05	-0.052	-0.162	0.183	0.250
1-2	-0.0323	-0.0237	0.0583	0.0401	216.22	-4.04	-0.009	-0.162	0.173	0.237
1-3	-0.0343	-0.0211	0.0618	0.0402	211.59	-3.12	-0.013	-0.126	0.161	0.205
1-4	-0.0358	-0.0190	0.0650	0.0405	208.01	-3.59	-0.048	-0.156	0.172	0.237
1-5	-0.0418	-0.0117	0.0753	0.0434	195.66	-2.60	-0.103	-0.118	0.125	0.200
1-6	-0.0444	-0.0100	0.0778	0.0455	192.68	–	–	–	–	–
2-1	-0.0814	-0.1118	0.0861	0.1383	233.95	-7.95	0.244	-1.099	0.077	1.12
2-2	-0.1015	-0.1009	0.0880	0.1432	224.84	-7.40	0.461	-1.059	0.080	1.16
2-3	-0.1227	-0.0903	0.0896	0.1524	216.36	–	–	–	–	–
3-1	-0.0430	-0.0105	-0.0054	0.0443	193.67	0.65	-0.096	0.028	-0.167	0.194
3-2	-0.0410	0.0105	-0.0087	0.0423	194.42	2.15	-0.076	0.088	-0.169	0.205
3-3	-0.0391	0.0119	-0.0121	0.0408	196.89	0.99	-0.079	0.038	-0.191	0.210
3-4	-0.0373	-0.0121	-0.0159	0.0392	198.02	–	–	–	–	–
4-1	-0.0808	0.0272	-0.0058	0.0852	161.38	2.40	-0.200	0.195	-0.158	0.321
4-2	-0.0781	0.0222	-0.0090	0.0812	164.13	2.17	-0.145	0.170	-0.195	0.297
4-3	-0.0762	0.0181	-0.0129	0.0783	166.62	2.09	-0.162	0.157	-0.206	0.308
4-4	-0.0737	0.0143	-0.0170	0.0751	169.01	–	–	–	–	–
5-1	0.0895	0.0835	-0.0110	0.1224	43.02	2.78	0.305	0.323	-0.131	0.463
5-2	0.0805	0.0839	-0.0136	0.1163	46.20	–	–	–	–	–
6-1	0.1091	0.0830	0.0004	0.1371	37.25	2.48	-0.377	0.322	-0.147	0.517
6-2	0.0991	0.0835	0.0033	0.1295	40.09	–	–	–	–	–
7-1	0.0497	0.1481	0.0044	0.1562	251.47	2.54	-0.414	0.377	-0.082	0.566
7-2	0.0398	-0.1425	0.0060	0.1480	254.39	2.64	-0.298	0.375	-0.082	0.486
7-3	0.0309	0.1386	0.0077	0.1420	257.41	2.42	-0.350	0.328	-0.104	0.490
7-4	0.0230	-0.1330	0.0097	0.1350	260.19	–	–	–	–	–
8-1	0.1798	0.0483	0.0028	0.1862	[illegible]	2.34	0.366	0.418	0.067	0.559
8-2	-0.1704	-0.0545	0.0014	0.1789	197.73	–	–	–	–	–
9-1	0.1925	-0.0249	0.0004	0.1940	187.37	2.62	0.248	0.496	0.050	0.557
9-2	-0.1860	-0.0341	0.0014	0.1891	190.38	–	–	–	–	–
10-1	-0.0533	0.2432	0.0265	0.2489	257.64	5.73	-0.064	1.418	0.109	1.42
10-2	0.0050	-0.2464	-0.0244	0.2476	264.20	5.77	0.105	1.416	0.076	1.42
10-3	0.0034	0.2455	-0.0228	0.2456	270.81	5.25	0.267	1.318	0.044	1.35
10-4	0.0298	-0.2491	-0.0219	0.2506	276.83	5.20	0.138	1.276	0.050	1.28
10-5	0.1022	-0.2201	0.0189	0.2426	294.91	4.94	0.062	1.192	0.049	1.19
10-6	0.1227	-0.2078	0.0179	0.2414	300.57	–	–	–	–	–
11-1	-0.0871	0.0987	-0.0486	0.1316	131.45	5.59	0.034	0.733	-0.255	0.778
11-2	-0.0981	0.0888	-0.0537	0.1323	137.84	5.71	0.070	0.755	-0.238	0.811
11-3	-0.1087	0.0779	-0.0594	0.1337	144.38	–	–	–	–	–
12-1	0.0265	-0.1184	-0.0923	0.1213	282.60	7.60	0.139	0.943	-0.167	0.968
12-2	0.0451	-0.1156	-0.0956	0.1241	291.31	8.35	0.250	1.078	-0.147	1.116
12-3	0.0663	-0.1108	-0.0985	0.1291	300.88	8.02	0.454	1.108	-0.150	1.207
12-4	0.0889	-0.1057	-0.1016	0.1281	310.07	–	–	–	–	–
13-1	0.1424	-0.1217	-0.0944	0.1873	319.49	10.25	0.355	1.99	0.060	2.02
13-2	0.1704	-0.0935	-0.0931	0.1944	331.23	12.08	0.103	2.37	0.133	2.38
13-3	0.1898	-0.0506	-0.0905	0.1964	345.08	10.58	0.173	2.11	0.166	2.13
13-4	0.1997	-0.0098	-0.0872	0.1999	357.20	–	–	–	–	–

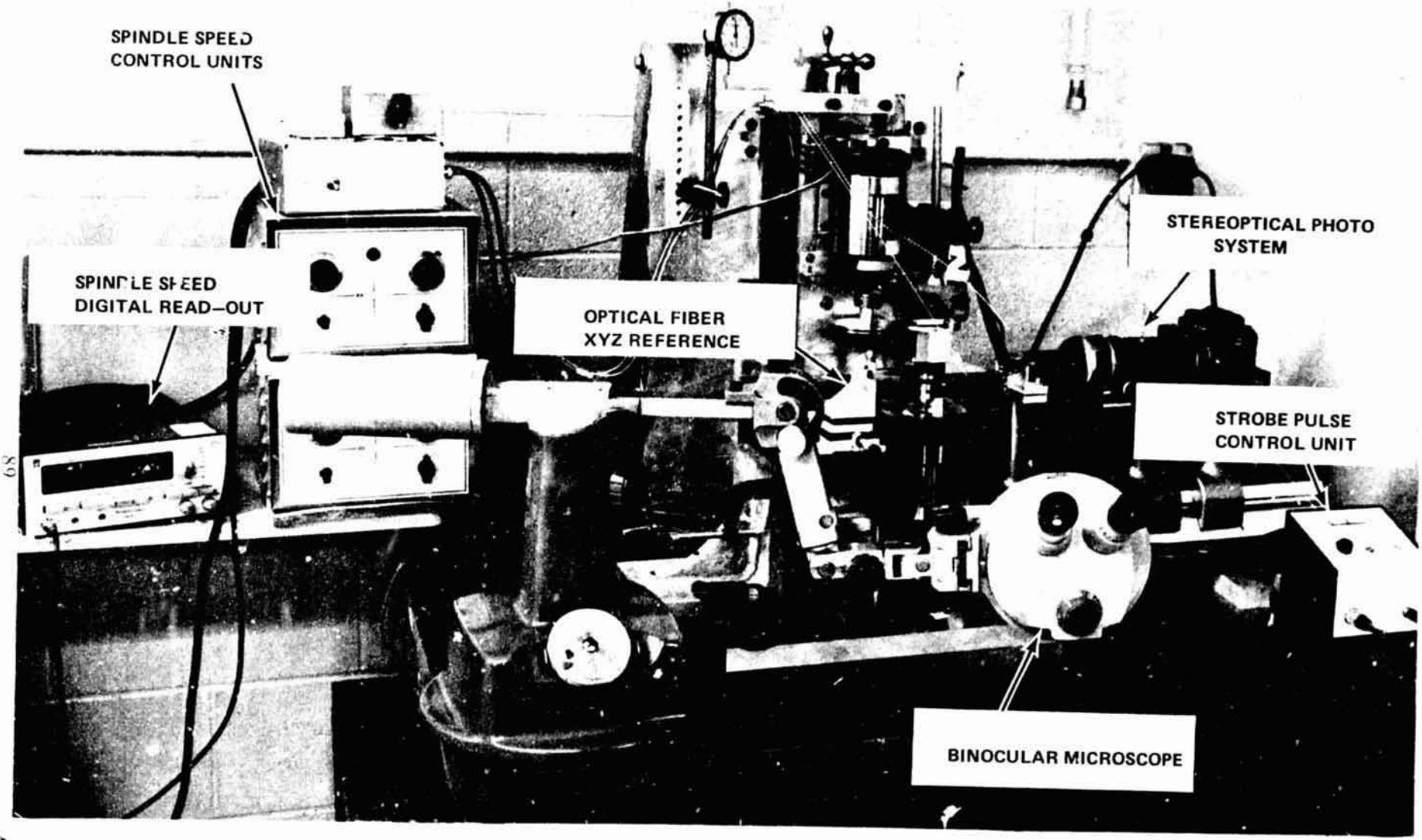

FIGURE 1 EXPERIMENTAL SET-UP FOR INVESTIGATION OF FLOW WITHIN FLOATING ZONES

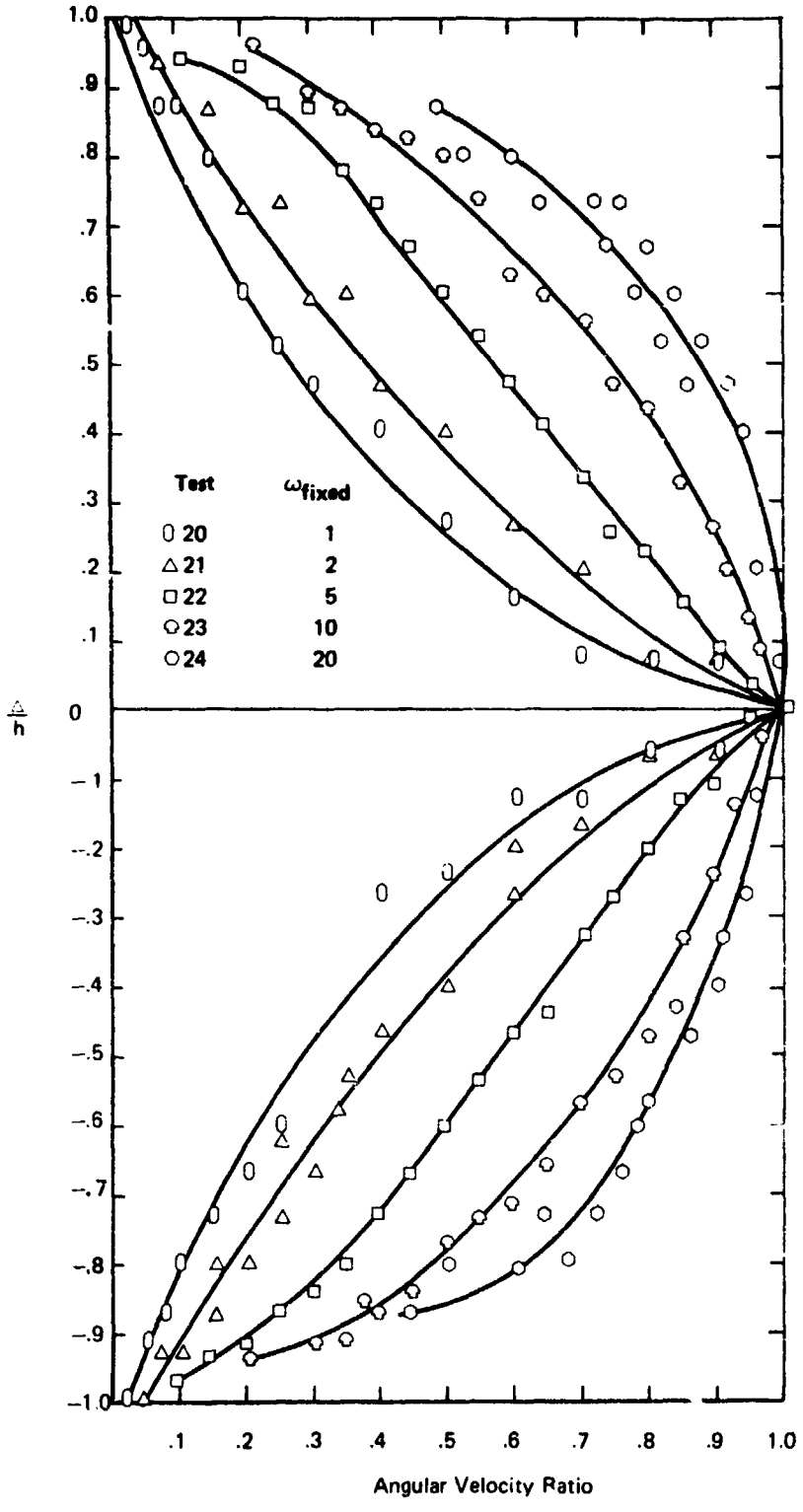

FIGURE 2 EFFECT OF FIXED ANGULAR VELOCITY ON $\frac{\Delta}{h}$ AS A FUNCTION OF ANGULAR VELOCITY RATIO

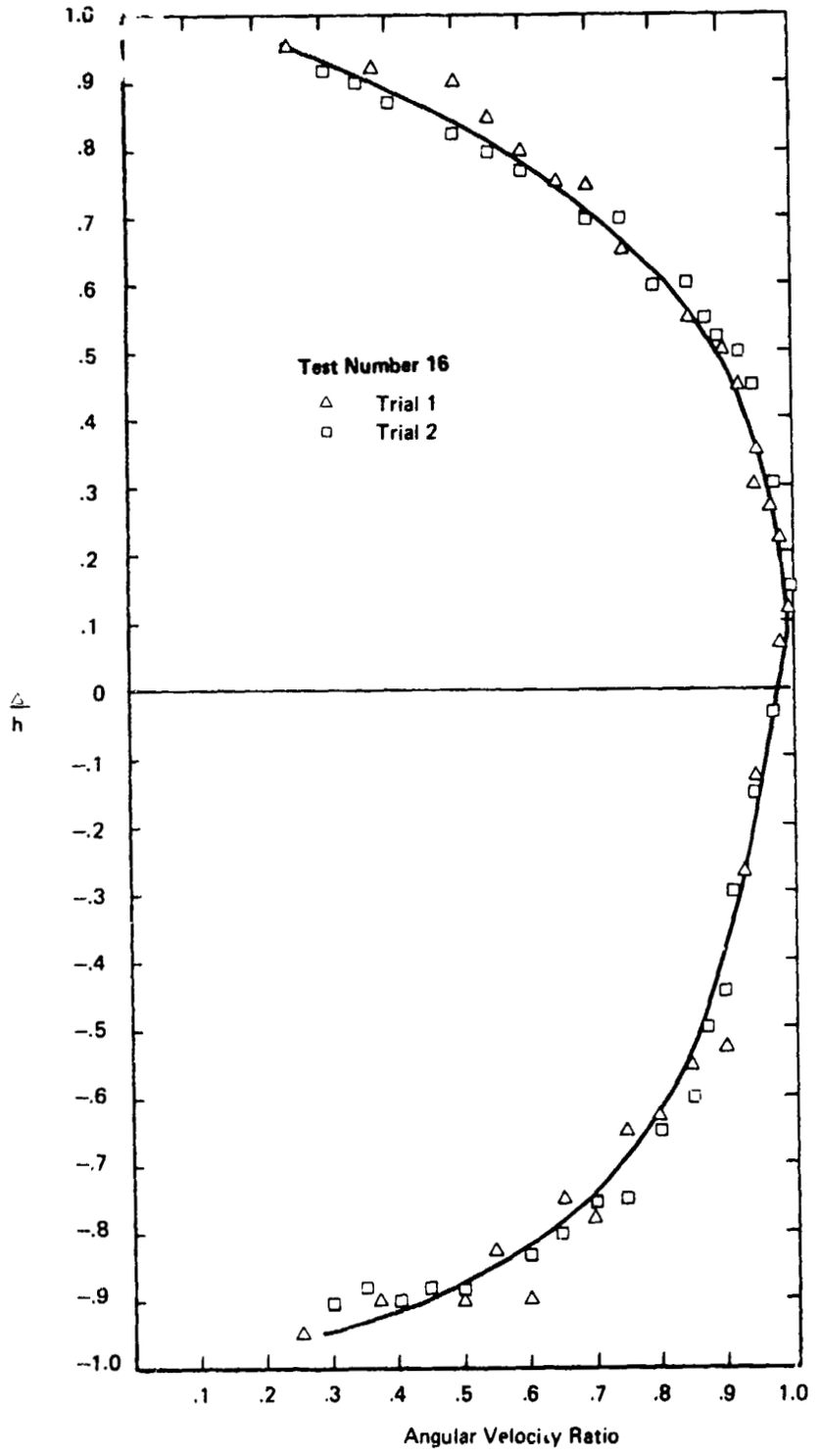

FIGURE 3 REPRODUCIBILITY OF THE MEASUREMENT OF $\frac{\Delta}{h}$ AS A FUNCTION OF ANGULAR VELOCITY RATIO

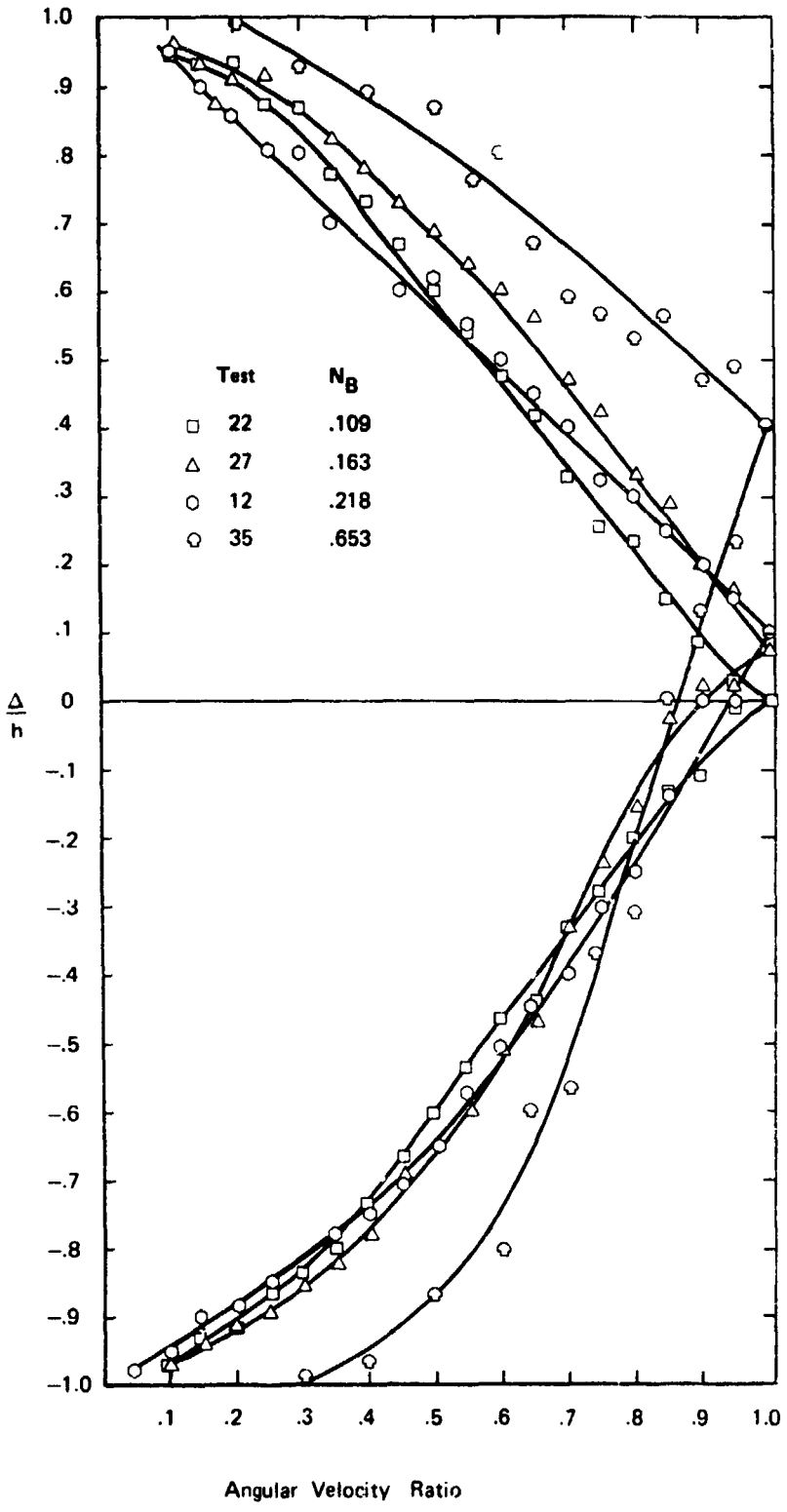

FIGURE 4 EFFECT OF BOND NUMBER ON $\frac{\Delta}{h}$ AS A FUNCTION OF ANGULAR VELOCITY RATIO

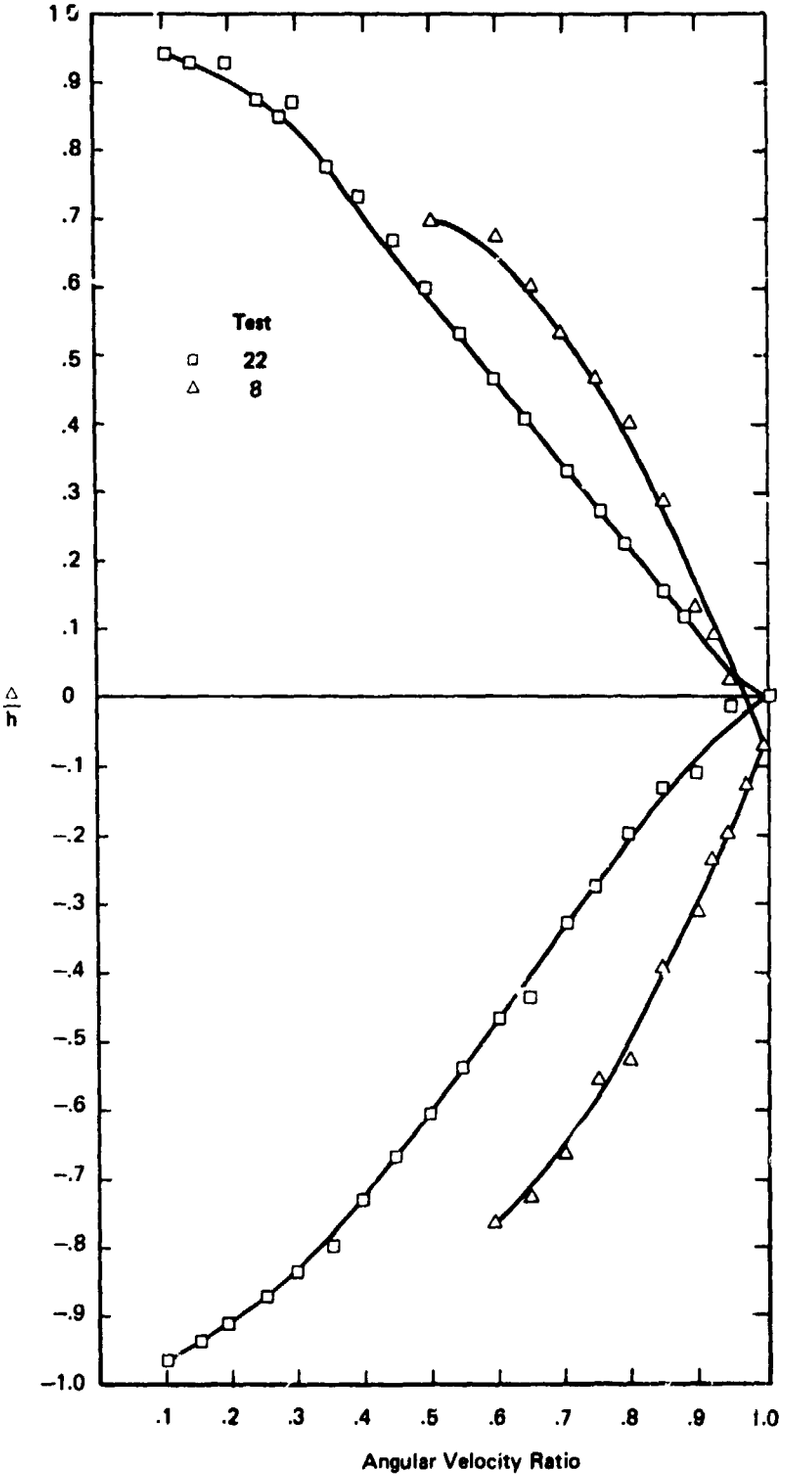

FIGURE 5 EFFECT OF WEBER NUMBER ON $\frac{\Delta}{h}$ AS A FUNCTION OF ANGULAR VELOCITY RATIO, AT A CONSTANT REYNOLDS NUMBER

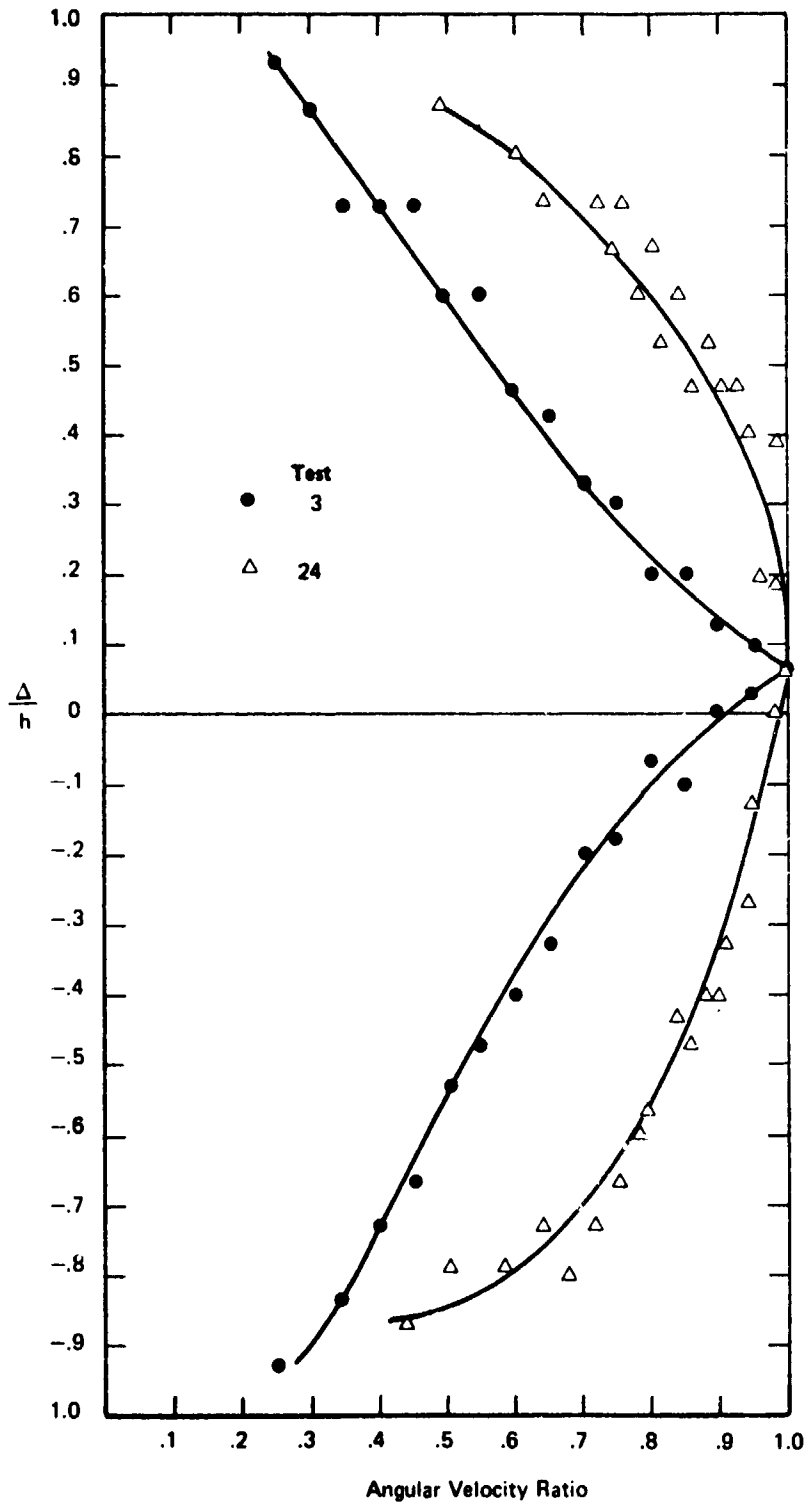

FIGURE 6 EFFECT OF REYNOLDS NUMBER ON $\frac{\Delta}{h}$ AS A FUNCTION OF ANGULAR VELOCITY RATIO, AT A CONSTANT WEBER NUMBER

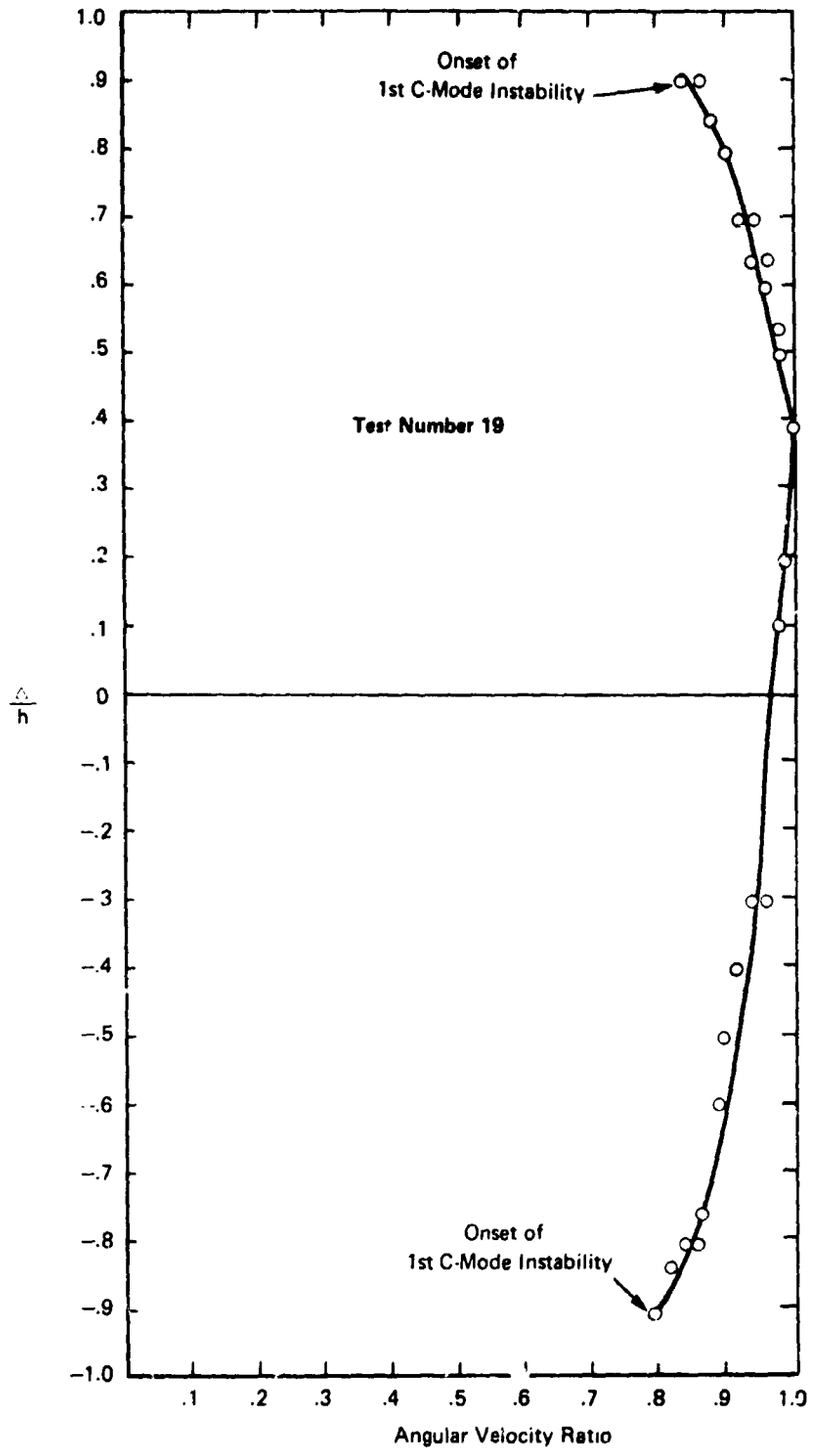

FIGURE 7 $\frac{\Delta}{h}$ AS A FUNCTION OF ANGULAR VELOCITY RATIO FOR CONDITIONS APPROACHING THE 1ST C-MODE INSTABILITY

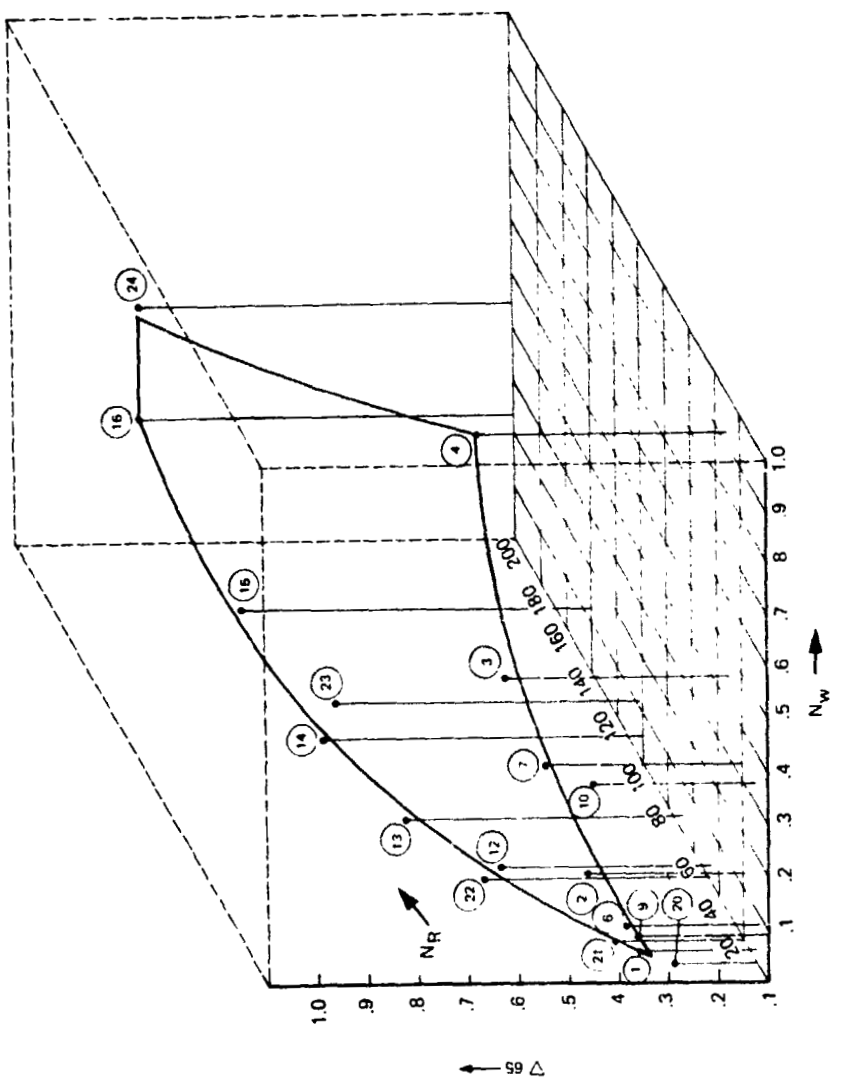

FIGURE 8 PLOT OF ∇ .65 AS A FUNCTION OF REYNOLDS AND WEBER NUMBERS FOR TESTS 1, 2, 3, 4, 6, 7, 9, 10, 12, 13, 14, 15, 16, 20, 21, 22, 23, AND 24

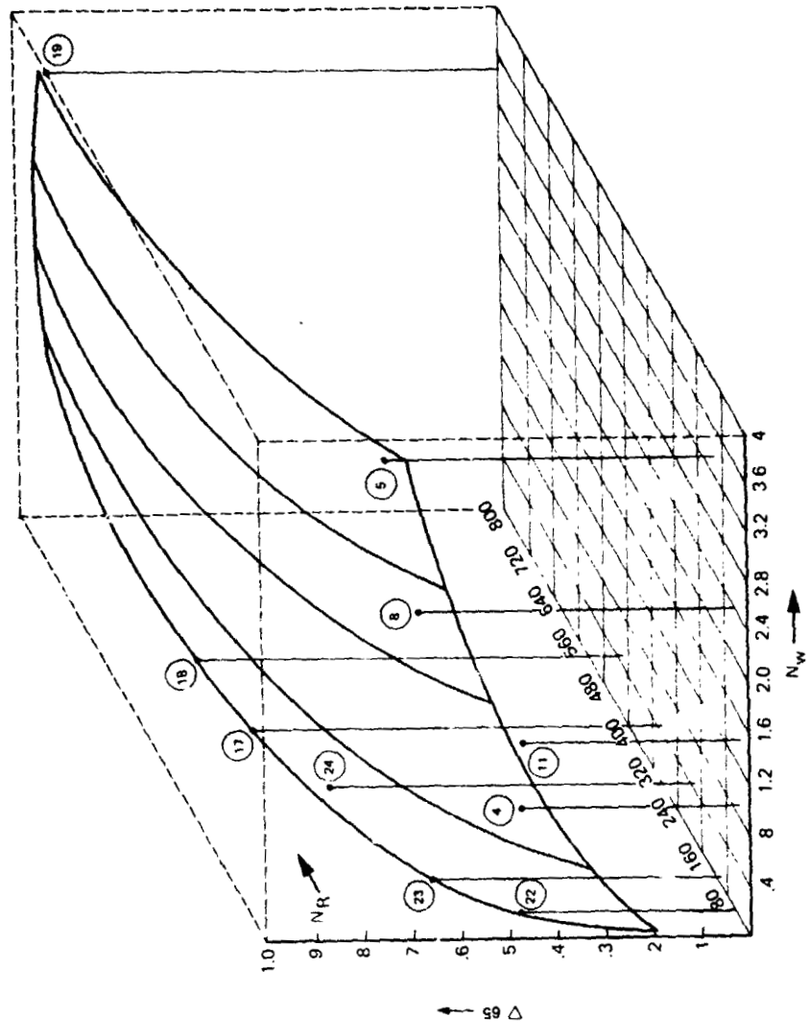

FIGURE 9 PLOT OF ∇ .65 AS A FUNCTION OF REYNOLDS AND WEBER NUMBERS FOR TESTS 4, 5, 8, 11, 17, 18, 19, 20, 22, 23, AND 24

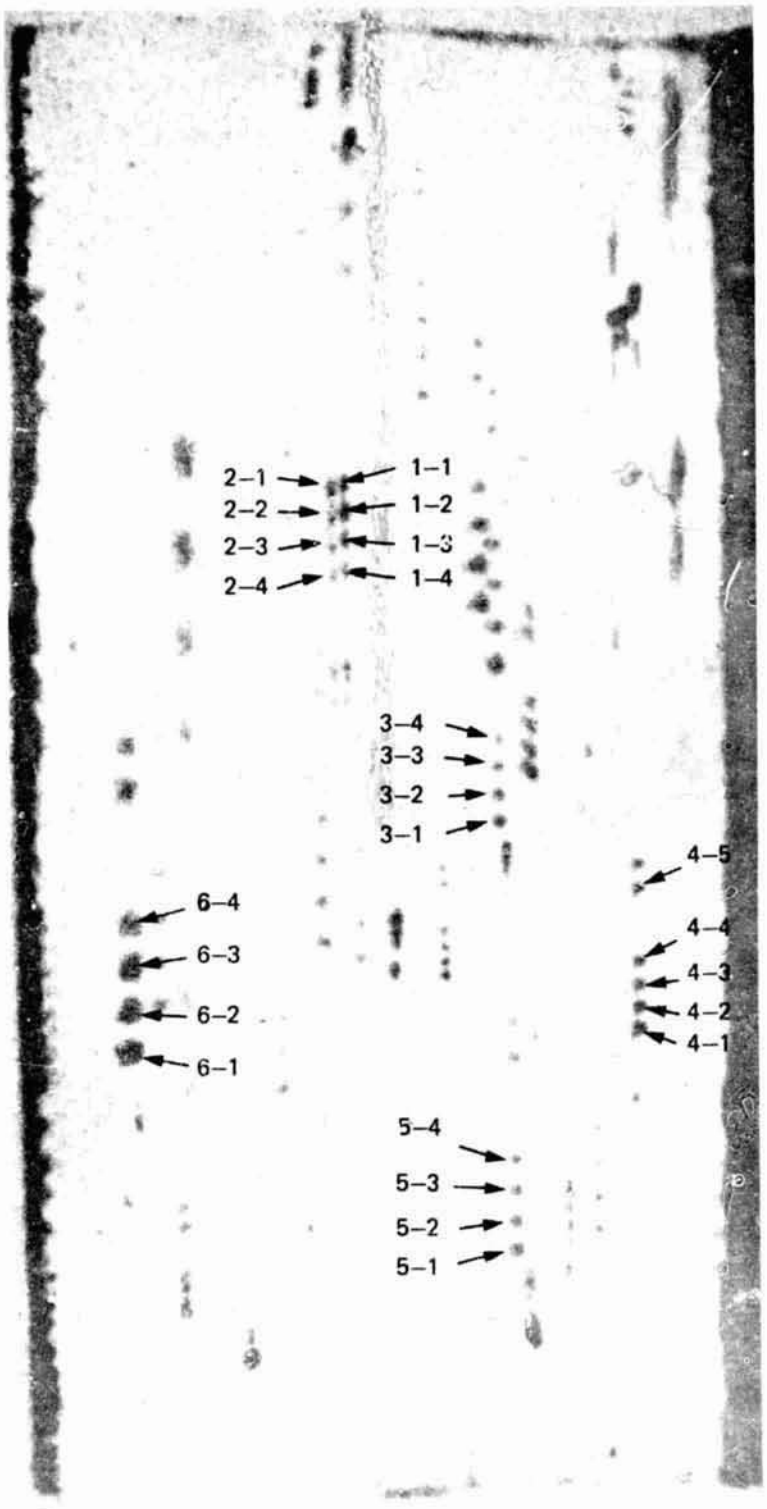

FIGURE 10 ONE OF A STEREOPAIR OF PHOTOGRAPHS FOR ISOROTATION AT 2.0 REV/SEC

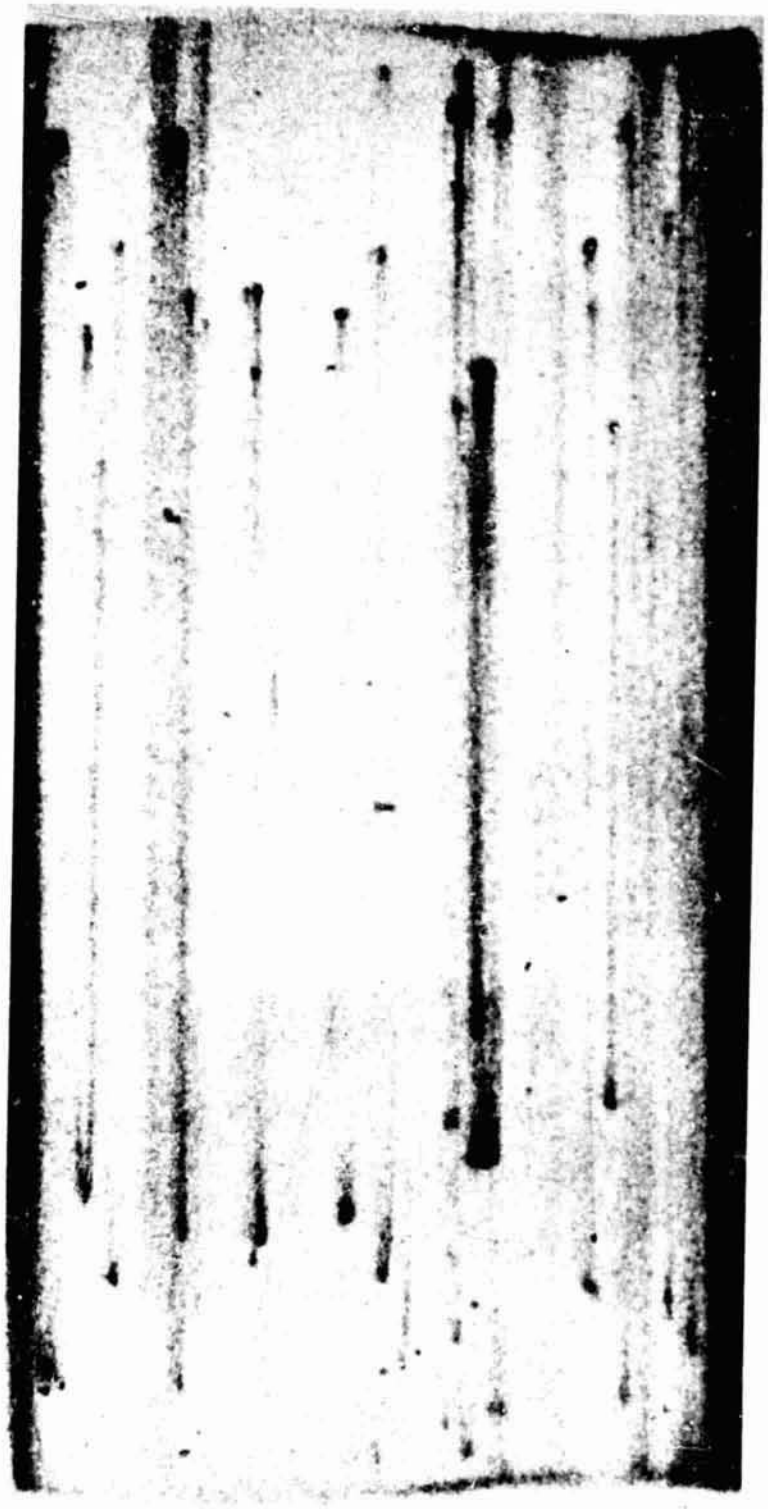

FIGURE 11 PHOTOGRAPH USED TO MEASURE THE SHAPE OF THE FREE SURFACE OF THE COLUMN

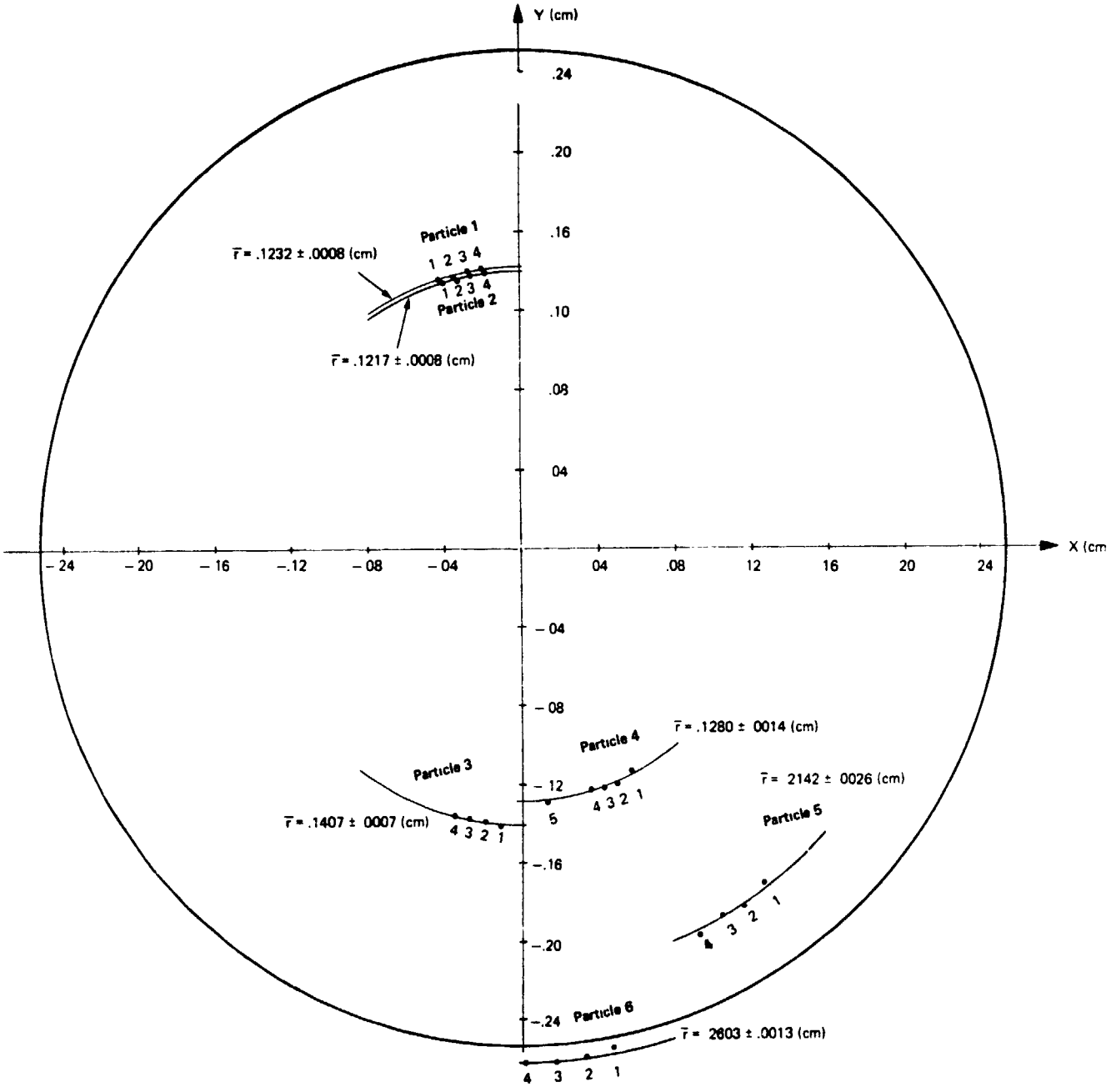

FIGURE 12 PLOT OF CALCULATED VALUES OF PARTICLE POSITION FOR ISOROTATION AT 2.0 REV/SEC

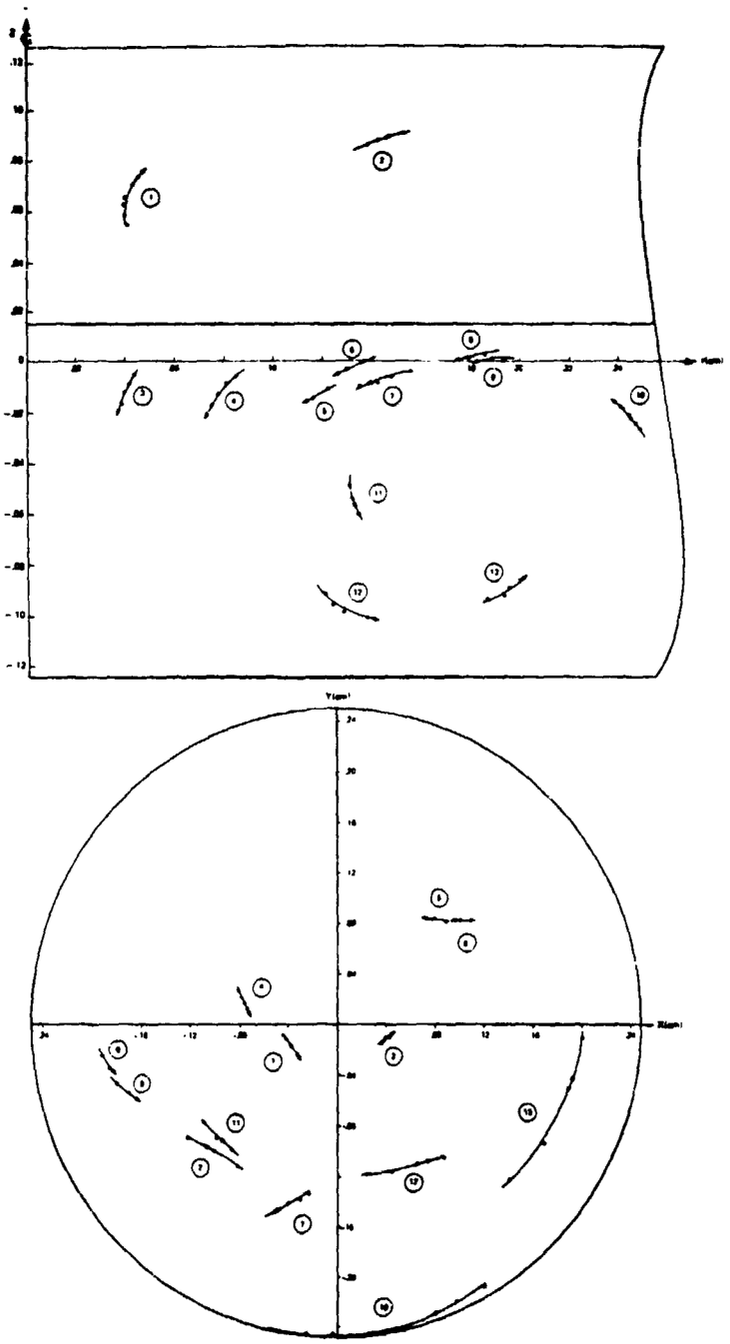

FIGURE 13 PLOT OF CALCULATED VALUES OF PARTICLE POSITION FOR EQUAL COUNTERROTATION AT 2.5 REV/SEC

APPENDIX A

DESIGN CONSIDERATIONS FOR A STEREOPTICAL SYSTEM AND A METHOD FOR TAKING VELOCITY MEASUREMENTS

DESIGN

The design of the stereoptical system is illustrated in Figure A-1. The basic principle adopted for the design of the stereo-reflector is a four-mirror arrangement very similar to that used in the Wheatstone stereoscope.[1]

The stereo-reflector consists of plane mirrors m_1, m_3, and m_4. The two outer mirrors, m_1 and m_2, are arranged at an angle less than 45 deg to the axis of the lens. Between those two mirrors, the inner pair is positioned so that the reflecting surfaces are at right angles to each other and at a 45-deg angle to the axis of the lens. The inner vertical edges of m_3 and m_4 meet on the optical axis and, as a result, each of the two mirrors occupies one half of the field of view.

A "left-eye" view of the subject is formed by rays, such as L, which after reflection at the surface of m_1 are then reflected in the direction of the lens by m_3. The image is brought to focus at ℓ. Likewise, a "right-eye" view is formed by rays, such as R, which after reflection by the mirrors m_2 and m_4 are brought to focus at r.

The images r and ℓ can be thought of as being formed by two cameras rotated by an angle ϕ_1 and ϕ_2 to the left and right of the optical axis, as shown by the dotted lines. The positions of the two virtual cameras and the actual camera are related by the following geometrical relationships:

$$\phi_1 = 2(\theta_1 - 45°) - \alpha_1 \qquad \text{(A-1)}$$

and

$$\phi_2 = 2(\theta_2 - 45°) - \alpha_2 \cdot \qquad \text{(A-2)}$$

where

ϕ_1 = the angle between the optical axis of camera 1 and the y-axis of the object coordinate system,

θ_1 = the angle between the plane of mirror m_1 and the perpendicular to the optical axis of the actual camera, and

α_1 = the angle between ray L and the optical axis of the actual camera.

---

(1) Applied Optics and Optical Engineering (Kingslake, R. ed.), Academic Press, Vol. II., 1965, p. 89.

A similar nomenclature with subscript 2 applies to ray R:

$$\alpha_1 = \tan^{-1} \frac{d_1}{FL} \tag{A-3}$$

$$\alpha_2 = \tan^{-1} \frac{d_2}{FL} \tag{A-4}$$

where

d_1 = the distance from the center of the image at ℓ to the center of the film plane,

d_2 = the distance from the center of the image at r to the center of the film plane,

FL = the film-to-lens conjugate distance,

OL = the object-to-lens conjugate distance.

Assuming the camera lens is thin, then:

$$FL = (1 + M)f \tag{A-5}$$

$$FO = \left(\frac{1 + M}{M}\right)f \tag{A-6}$$

where

M = magnification, and

f = the focal length of the lens.

The first step in the design of the system is the selection of values of f and M. Both theoretical and practical considerations must be taken into account. Some of the theoretical aspects of photographing a small particle in dark-field illumination have been treated in detail in previous work.[2] For smooth spherical particles illuminated by light coming from one direction, assuming that the light can be treated as consisting of plane waves and that it is scattered isotropically by the particle, the camera lens will produce a diffraction pattern of the glint of light it receives from the particle. If this diffraction pattern is the classical Airy disk, the diameter of the central disk is given by:

$$D_\alpha = 2.44\lambda F \tag{A-7}$$

where

λ = the wavelength of the light, and

F = the f-number or relative aperture of the lens.

(2) Fowle, A.A., et al., Float Zone Processing in a Weightless Environment, NASA CR-2768, 1976.

The F-number or relative aperture of the lens is defined as:

$$F = \frac{f}{D} \tag{A-8}$$

where

f is the focal length, and

D is the diameter of the aperture.

In macrophotography, the f-number is defined as either:

$$F = \frac{(1+M)f}{D} \text{ or } \frac{f(1+M)}{MD}, \tag{A-9}$$

whichever is smaller. This formulation represents the so-called bellows correction.

The diameter of the resolution element, ΔX, in the object plane is found by dividing the diameter of the resolution element at the image by the magnification M. Thus:

$$\Delta X = \frac{D_\alpha}{M} = 2.44\lambda \left(\frac{F}{M}\right). \tag{A-10}$$

The depth of field, calculated by geometrical optics, is given by:

$$\Delta Y = 2.44\lambda\left(\frac{F}{M}\right)^2. \tag{A-11}$$

Equations (A-10) and (A-11) show that the depth of field and the size of the resolution element in the object plane depend only on the ratio F/M (for light of a given wavelength). We would like ΔX to be small (high resolution) and ΔY to be large (large depth of field), but these are conflicting requirements.

In practice, the higher limit of the F-number is determined by the following parameters: particle size, particle reflectivity, energy output of the illumination system, and film speed. The ease with which the images can be enlarged and accurate measurement of particle position be made is an added consideration that must be taken into account in choosing the magnification.

Taking all the above factors into account resulted in the following design specifications:

- a 105-mm, f/4 Micro-Nikkor lens,
- M = 0.80,
- F = 24.7,
- Nickel-coated, hollow-glass spheres 30-45 μm in diameter,
- Xenon flash apparatus consisting of a modfied General Radio Company, type 1531-A Strobomer, with discharge energy of 5.48 joules, and
- Kodak Plus-X 125 ASA film.

For these conditions, adequate contrast, a depth of field of 0.13 cm (on the order of the radius of the liquid column), a resolution of 42 μm (of the order of the particle diameter), and an image size of 0.2 by 0.4 cm which could be enlarged to useful size with a microscope at 20X were achieved.

The design specifications of the stereo reflector were tailored to the specific value of f-105 mm and M=0.80. A schematic diagram of the device is shown in Figure A-2. For mirrors m_1 and m_2, 25.0 mm square, first-surface mirrors (Melles-Griot #02 MPG 001) were used. A right-angle prism (Melles-Griot #01 ORS 020/011) with silvered legs was used for mirrors m_3 and m_4. Machined parts were used to hold the two mirrors and the prism in place. Four sets of these parts were made; they are interchangeable and provide angles θ_1 and θ_2 of 51, 53, 55, and 57 deg. These correspond to convergence half angles of 8.0, 12.0, 16.0, and 20.0 deg., respectively, for f=105 mm and M=0.80.

The following procedure was followed in aligning the system for making quantitative measurements:

Step 1 — The alignment of the two plexiglass rods is verified, with minor adjustments made if necessary;

Step 2 — The X, Y, Z, micropositioner is calibrated such that the position of the end of the optical fiber is known with respect to the center of the end-faces;

Step 3 — The magnification is set by adjusting the bellows attachment and measured from photographs of a scale;

Step 4 — The camera is aligned on the optical bench, such that the optical axis passes through the center of the column and is orthogonal to the coordinate system of the micropositioner; and

Step 5 — The stereoreflector is aligned such that both stereo images are in focus and $d_1 = d_2$.

The system can then be used to obtain stereoscopic photographs of the liquid column from which quantitative measurements can be made.

IMAGE INTERPRETATION

In interpreting the image of particles within the liquid column, refraction effects at the water-air interface must be taken into account. Figure A-3 shows the effects of refraction at the front surface of a water column. The positions of particles within the column are significantly distorted by refraction; only particles very close to the front surface of the column are not affected. Particles in the zone labeled "shadow zone" in Figure A-3 will be invisible to the observer, and worse still, the very existence of this shadow zone will not manifest itself to the observer at all. Rays emitted by particles in the zone labeled "double image zone" will emerge near the edge of the cylinder, giving the impression that the contents of the entire cylinder are in view. For particles in this zone, we see a double image.

Figure A-4 shows the overlap between the shadow zones and double image zones for the two cameras at a convergence half angle of 12 deg, focussed about the center of a liquid column of radius = 0.127 cm. Also shown are the areas of best focus for each camera for a depth of field of $\pm\Delta Y$ = 0.13 cm. The result is 14 distinct zones in the liquid column that must be taken into

account in interpreting a stereoscopic pair of particle images within the water column. This makes the visual interpretation of the stereo photographs a rather difficult task. The areas for which useful information can be obtained within the liquid column are 1, 2, 3, and 4 as labeled in Figure A-4.

DATA EXTRACTION

An Opto-Metric Tools Model 1041 toolmaker's microscope was used to make measurements directly on the 35 mm negatives. The negative is mounted on a glass slide which is then aligned, such that the X ane Z directions on the negative are parallel to the X and Y directions of the microscope as shown schematically in Figure A-5.

Since the camera is focussed about the center of the column, and the optical axis passes through the center, the outline of the column will exhibit no parallax (assuming the shape of the column is axi-symmetric. Therefore, the edge can be used to determine the radius as a function of the height. These data are used in correcting the calculations of particle positions for the effects of refraction. This is discussed in Appendix B.

Measurement of the position of the particle images is made as follows. Referring to Figure A-5, one sees that the origin of the film coordinate system is determined by:

$$X_o = \frac{|a - b|}{2} + a \qquad \text{(A-12)}$$

and

$$Z_o = \frac{|c - d|}{2} + d \ . \qquad \text{(A-13)}$$

The coordinates of point e are determined by:

$$X_e = X_o - e_x \qquad \text{(A-14)}$$

and

$$Z_e = e_x - Z_o \ . \qquad \text{(A-15)}$$

where

a, b, c, d, e_x, e_z are positions expressed in the microscope table coordinate system.

The reproducibility in the determination of the location of a single point using the toolmaker's microscope is ±.00005 in. (±1.3 μm). The maximum uncertainty in the measured value of X_e and Z_e is three times the value of the uncertainty in the position of a single point or ±3.8 μm.

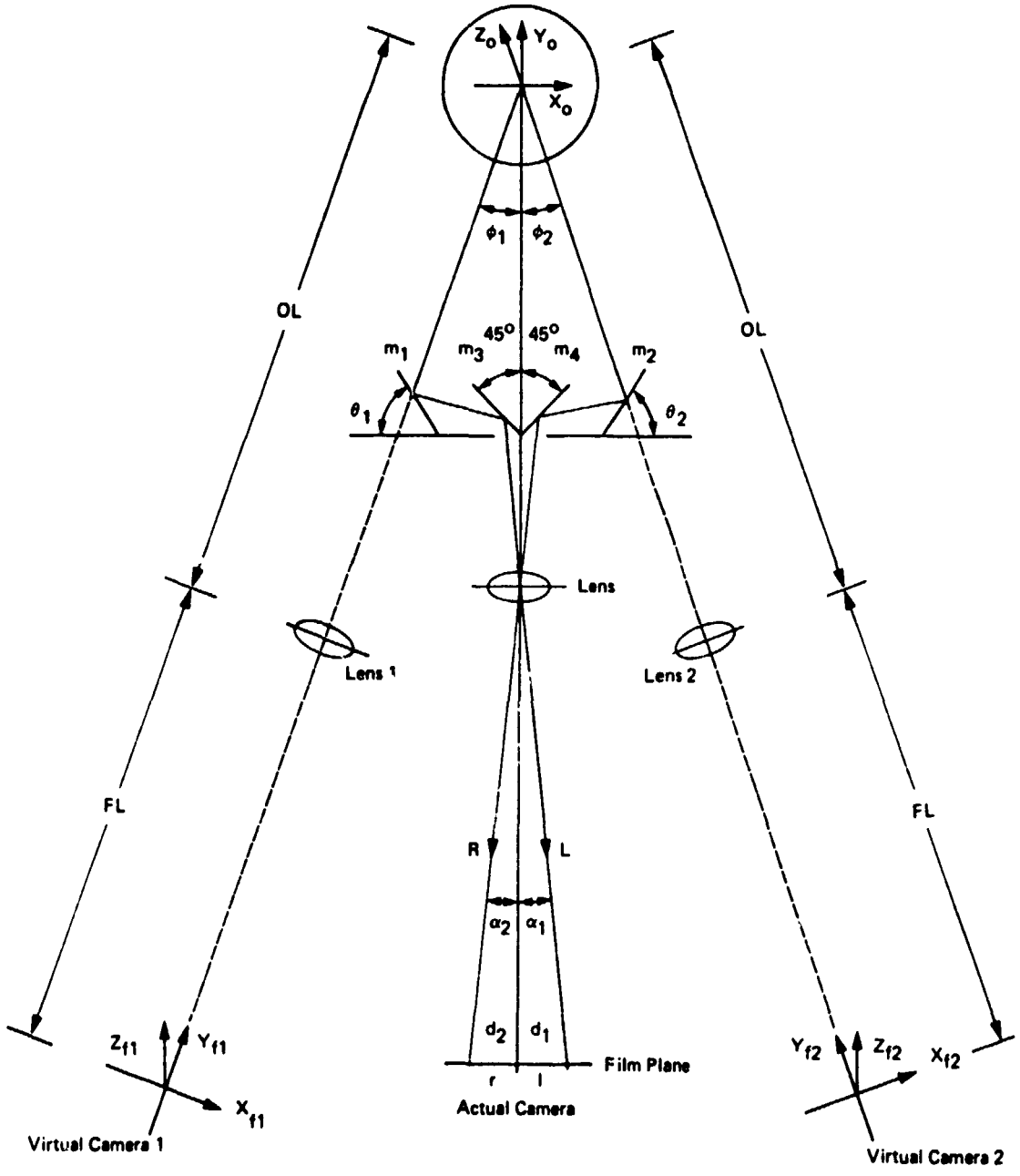

FIGURE A-1 SCHEMATIC DIAGRAM OF STEREOPTICAL PHOTOGRAPHIC SYSTEM

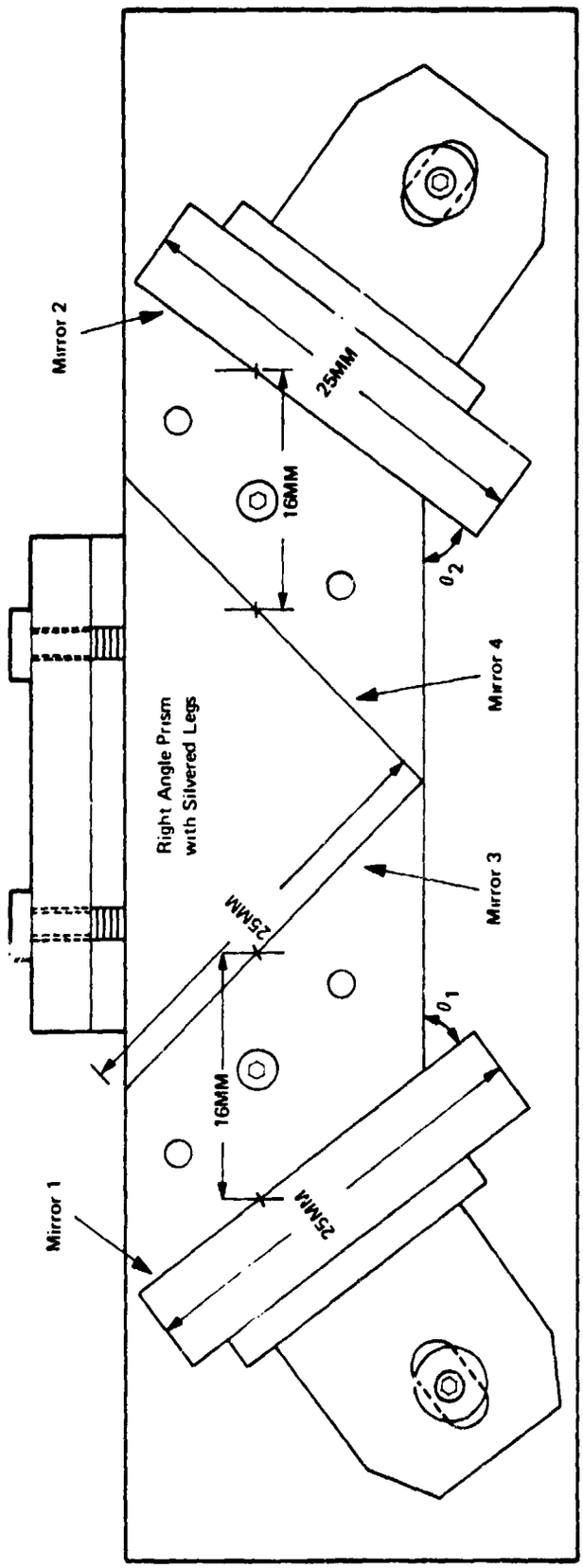

FIGURE A-2 STEREO REFLECTOR CONFIGURATION

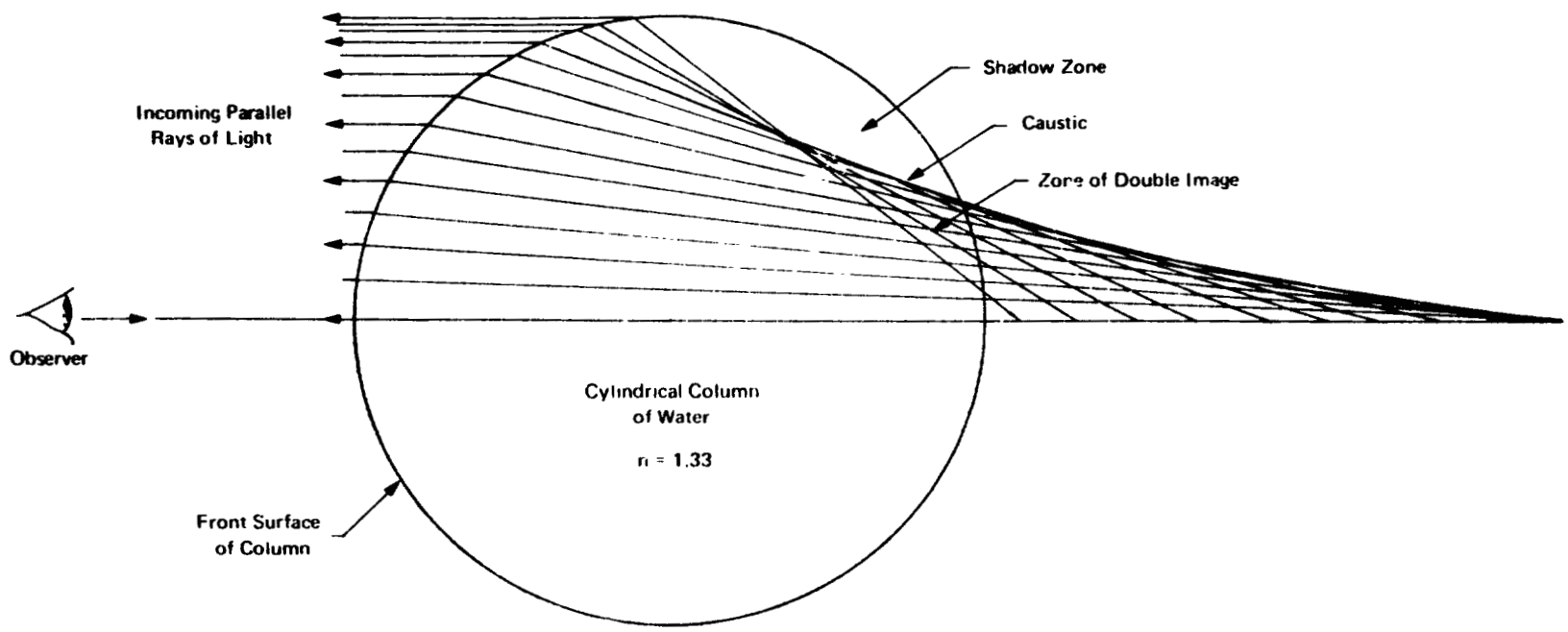

FIGURE A-3 CONSTRUCTION SHOWING THE REFRACTED RAYS OF LIGHT WITHIN A CYLINDRICAL COLUMN OF WATER

Camera 1 \ Camera 2	In Focus	Out of Focus	Double Image	Shadowed
In Focus	1	3	–	8
Out of Focus	2	4	7	11
Double Image	–	6	10	13
Shadowed	5	9	12	14

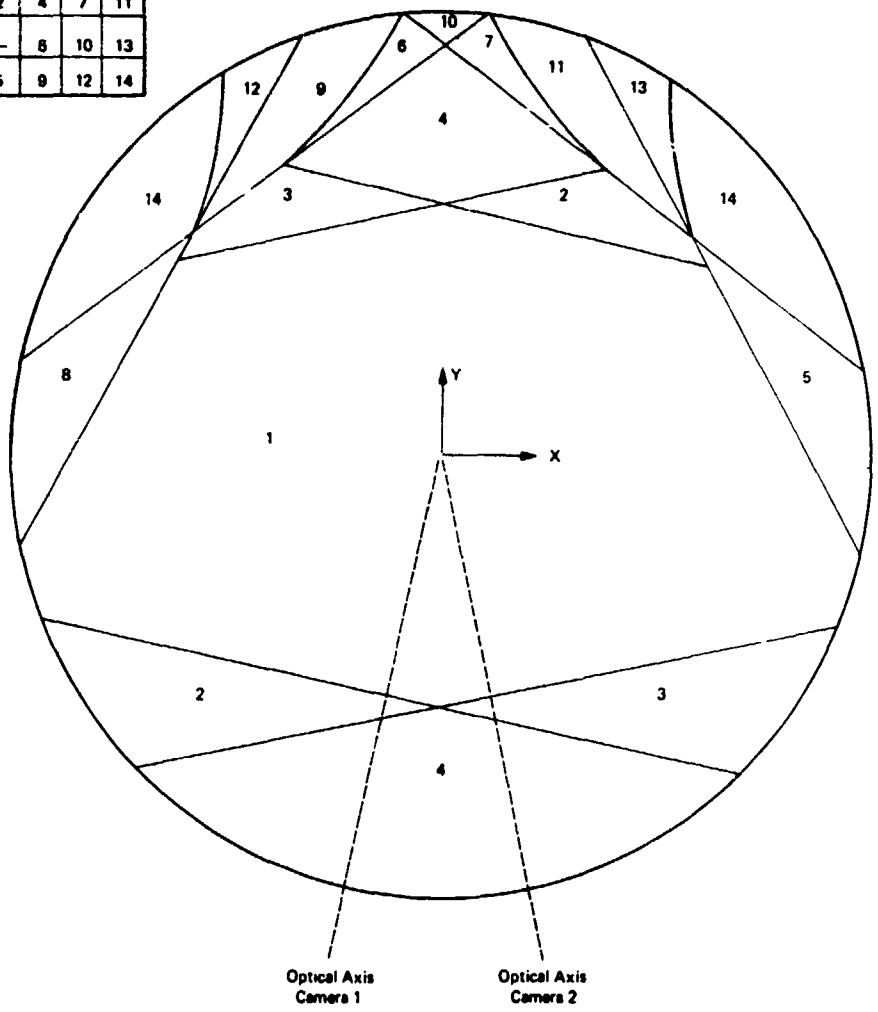

FIGURE A-4 CONSTRUCTION SHOWING ZONES OF DIFFERENT PARTICLE IMAGE QUALITY WITHIN A CYLINDRICAL COLUMN OF WATER

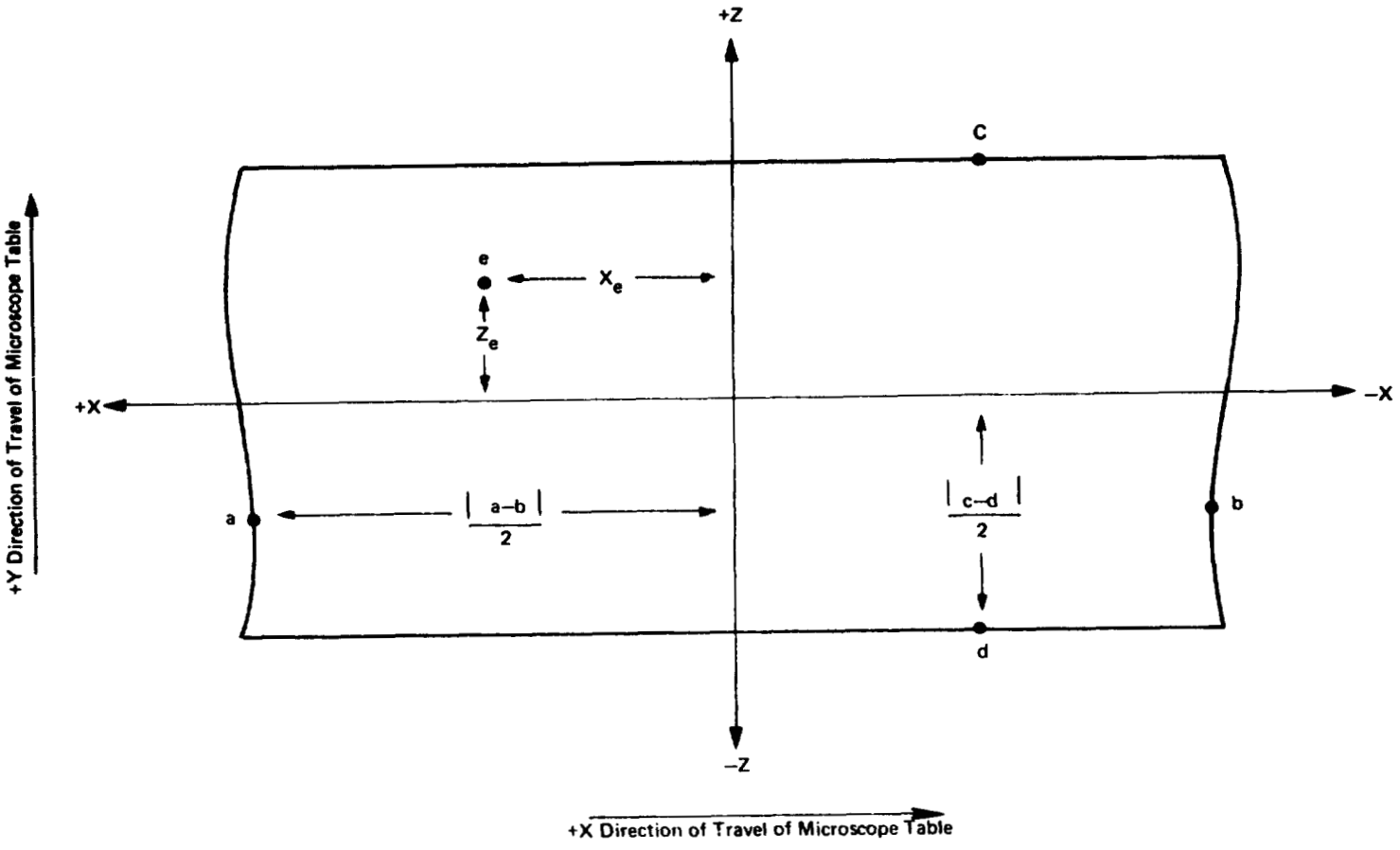

FIGURE A-5 ILLUSTRATION OF THE MEASUREMENT OF PARTICLE POSITION ON THE STEREOSCOPIC NEGATIVES

APPENDIX B

CALCULATION OF PARTICLE POSITION AND VELOCITY

METHOD

The position of a particle in the liquid column is determined from its location on a pair of stereoscopic photographic images. The analysis is based on ray traces in the optical system shown in Figure B-1. For each stereoscopic pair, a ray is traced starting at the image position, passing through the center of the lens. The points of intersection of each ray with the surface of the liquid column is then found, and by applying Snell's Law, the directions of the refracted rays are obtained. The points of closest approach between the two refracted rays are determined and their midpoint taken to be the position of the particle.

Three co-ordinate systems are used in the analysis: the object coordinate system and two film plane coordinate systems (f_1 and f_2), as shown in Figure B-1.

A ray of arbitray lenth originating at a point on film planes f_1 and f_2 can be written as:

$$\vec{P}_1 = \vec{b}_{01} + \hat{p}_1 s_1 \qquad \text{(B-1)}$$

$$\vec{P}_2 = \vec{b}_{02} + \hat{p}_2 s_2 \qquad \text{(B-2)}$$

where

$\vec{b}_{01}$ = base of ray expressed in object coordinates,

$\hat{p}_1$ = direction of the ray (unit vector), and

s_1 = length of the ray.

The nomenclature follows similarly for subscript 2.

The position of a point on the film plane is transformed from film plane to object co-ordinates by the following rotaion and translation equations:

$$\vec{b}_{01} = R_1 \vec{b}_{f1} + \vec{T}_1 \qquad \text{(B-3)}$$

$$\vec{b}_{02} = R_2 \vec{b}_{f2} + \vec{T}_2 \qquad \text{(B-4)}$$

where

$\vec{b}_{o1}$ = base of ray in object coordinates,

$\vec{b}_{f1}$ = base of ray in film plane coordinates,

R_1 = rotation maxtrix from the film 1 coordinate system to the object coordinate system, and

$\vec{T}_1$ = origin of the film coordinate system expressed in the object coordinate system.

The nomenclature follows similarly for subscript 2.

By substituting the coordinate values of b_{f1}, R_1, and T_1 into Equation (B-3), it can be rewritten as:

$$\vec{b}_{o1} = \begin{pmatrix} \cos\phi_1 & -\sin\phi_1 & 0 \\ \sin\phi_1 & \cos\phi_1 & 0 \\ 0 & 0 & 1 \end{pmatrix} \begin{pmatrix} x_1 \\ 0 \\ z_1 \end{pmatrix} + \begin{pmatrix} -(FL+OL)\sin\phi_1 \\ -(FL+OL)\cos\phi_1 \\ 0 \end{pmatrix} \quad \text{(B-5)}$$

Similarly substituting the values of b_{f2}, R_2, and T_2 into Equation (B-4), it can be rewritten as:

$$\vec{b}_{o2} = \begin{pmatrix} \cos\phi_2 & \sin\phi_2 & 0 \\ -\sin\phi_2 & \cos\phi_2 & 0 \\ 0 & 0 & 1 \end{pmatrix} \begin{pmatrix} x_2 \\ 0 \\ z_2 \end{pmatrix} + \begin{pmatrix} (FL+OL)\sin\phi_2 \\ -(FL+OL)\cos\phi_2 \\ 0 \end{pmatrix} \quad \text{(B-6)}$$

Carrying out the matrix multiplication and addition yields:

$$\vec{b}_{o1} = \begin{pmatrix} x_1\cos\phi_1 - (FL+OL)\sin\phi_1 \\ x_1\sin\phi_1 - (FL+OL)\cos\phi_1 \\ z_1 \end{pmatrix} \quad \text{(B-7)}$$

$$\vec{b}_{o2} = \begin{pmatrix} x_2\cos\phi_2 + (FL+OL)\sin\phi_2 \\ -x_2\sin\phi_2 - (FL+OL)\cos\phi_2 \\ z_2 \end{pmatrix} \quad \text{(B-8)}$$

Rays $\vec{L}_1$ and $\vec{L}_2$, originating at the vectors $\vec{b}_{o1}$ and $\vec{b}_{o2}$, must pass through the center of the thin lens. These rays in the object coordinate systems are:

$$\vec{L}_1 = \begin{pmatrix} -OL\sin\phi_1 \\ -OL\cos\phi_1 \\ 0 \end{pmatrix} \quad \text{(B-9)}$$

$$\vec{L}_2 = \begin{pmatrix} OL \sin \phi_2 \\ -OL \cos \phi_2 \\ 0 \end{pmatrix} \tag{B-10}$$

The unit direction vectors for rays $\vec{P}_1$ and $\vec{P}_2$ are:

$$\hat{p}_1 = \frac{\vec{L}_1 - \vec{b}_{01}}{|\vec{L}_1 - \vec{b}_{01}|} \tag{B-11}$$

$$\hat{p}_2 = \frac{\vec{L}_2 - \vec{b}_{02}}{|\vec{L}_2 - \vec{b}_{02}|} \tag{B-12}$$

The next step is to find the point of intersection of rays $\vec{P}_1$ and $\vec{P}_2$ with the surface of the liquid column.

Due to the effect of gravity, the shape of the column is not quite cylindrical. The radius of the distorted column is a function of the height (z) and is described by the following equation:

$$r = f(z) = a_n z^n + a_{n-1} z^{n-1} + \ldots + a_1 z + a_0 \tag{B-13}$$

where

r = radius,
z = height, and
a's = regression coefficients of a least squares fit to experimental data.

The surface of the distorted liquid column is described by the equation:

$$g(x,y,z) = x^2 + y^2 - [f(z)]^2 = 0. \tag{B-14}$$

Substituting the ray Equation (B-1) into Equation (B-14) yields the expression:

$$g(\vec{P}_1) = \left[\vec{b}_{01x} + \hat{p}_{1x} s\right]^2 + \left[\vec{b}_{01y} + \hat{p}_{1y} s\right]^2 - \left[f(\vec{b}_{01s} + \vec{p}_{12} s)\right]^2 \tag{B-15}$$

Equation (B-15) is of the general form g(s) = 0 and can be solved by iteration using Newton's method, which states:

$$s_{i+1} = s_i - \frac{g(s_i)}{g'(s_i)} \tag{B-16}$$

This is repeated until $\left|\frac{g(s_{i+n})}{g'(s_{i+n})}\right| < \epsilon$.

As g(s) is a continuous single-valued function of X, Y, and Z, its first derivative can be expressed by:

$$g'(s) = \frac{\partial g}{\partial x}\frac{dx}{ds} + \frac{\partial g}{\partial y}\frac{dy}{ds} + \frac{\partial g}{\partial f}\frac{df}{dz}\frac{dz}{ds} \qquad \text{(B-17)}$$

Differentiating Equation (B-15) yields:

$$\frac{\partial g}{\partial x} = 2\left[\vec{b}_{01x} + \hat{p}_{1x}\, s\right] \qquad \text{(B-18)}$$

$$\frac{dx}{ds} = \hat{p}_{1x} \qquad \text{(B-19)}$$

$$\frac{\partial g}{\partial y} = 2\left[\vec{b}_{01y} + \hat{p}_{1y}\, s\right] \qquad \text{(B-20)}$$

$$\frac{dy}{ds} = \hat{p}_{1y} \qquad \text{(B-21)}$$

$$\frac{dg}{df} = -2f(z) \qquad \text{(B-22)}$$

$$\frac{df}{dz} = na_n z^{n-1} + n\text{-}1a_{n-1} z^{n-2} + \ldots + a_1 \qquad \text{(B-23)}$$

$$\frac{dz}{ds} = \hat{p}_{12} \qquad \text{(B-24)}$$

To calculate a first approximation of s to be used in Newton's method, we find where the ray intersects a right circular cylinder of radius R whose surface is described by the equation:

$$x^2 + y^2 - R^2 = 0 \qquad \text{(B-25)}$$

Substituting the ray Equation (B-1) into Equation (B-25) yields the expression:

$$[\vec{b}_{01x} + \vec{p}_{1x}\, s]^2 + [\vec{b}_{01y} + \vec{p}_{1y}\, s]^2 - R^2 = 0 \quad . \tag{B-26}$$

Multiplying out gives:

$$[(\hat{p}_{1x})^2 + (\hat{p}_{1y})^2]s^2 + [(\vec{b}_{01x}\,\hat{p}_{1x}) + (\vec{b}_{01y}\,\hat{p}_{1y})]s + [(\vec{b}_{01x})^2 + (\vec{b}_{01y})^2] - R^2 = 0 \quad . \tag{B-27}$$

Equation (B-27) is quadratic in s and can be solved explicitly. This result is then used as an initial value in Newton's method.

In practice, the iteration is repeated until $|g(s)/g'(s)| < .0001$ cm; the final value of s calculated was then substituted into the ray Equations (B-1) and (B-2) to obtain the points of intersection $\vec{p}_{1i}$ and $\vec{p}_{2i}$. The normal to the surface of the liquid column is then calculated:

$$\hat{n} = \frac{\nabla g}{|\nabla g|} = \frac{1}{\sqrt{\left(\frac{\partial g}{\partial x}\right)^2 + \left(\frac{\partial g}{\partial y}\right)^2 + \left(\frac{\partial g}{\partial z}\right)^2}} \left(\frac{\partial g}{\partial x}, \frac{\partial g}{\partial y}, \frac{\partial g}{\partial z}\right) \tag{B-28}$$

The normal for the surface of Equation (B-14) is:

$$\hat{n} = \frac{1}{\sqrt{x^2 + y^2 + [f(z)f'(z)]^2}} \; ((x_1 y_1 - f(z)f'(z)) \quad . \tag{B-29}$$

The ray is refracted as it passes into the liquid. The unit vector $\hat{q}$ of the refracted ray can be determined by applying Snell's Law, which states that the incident ray $\hat{p}$, the normal $\hat{n}$, and the refracted ray $\hat{q}$ lie on the same plane, and

$$n_1 \sin\theta_1 = n_2 \sin\theta_2 \tag{B-30}$$

where

n_1, n_2 are the refractive indices of the two media:
θ_1 = the angle between $\hat{p}$ and $\hat{n}$, and
θ_2 = the angle between $\hat{q}$ and $\hat{n}$.

The term $\hat{q}$ can be expressed in terms of its components relative to $\hat{n}$ and $\hat{w}$, where $\hat{w}$ is the unit tangent vector lying in the plane defined by the incident and refracted rays (plane of incidence):

$$\hat{q} = -\hat{n}\cos\theta_2 + \hat{w}\sin\theta_2 \tag{B-31}$$

where

$$\hat{w} = \hat{n} \times \hat{v} \text{ and } \hat{v} = \frac{\hat{p} \times \hat{n}}{\sin \theta_1} \tag{B-32}$$

is the normal to the plane of incidence.

Hence:

$$\hat{w} = \frac{1}{\sin \theta_1} \left[\hat{n} \times (\hat{p} \times \hat{n})\right]$$

$$w = \frac{1}{\sin \theta_1} \left[(\hat{n} \cdot \hat{n})\, \hat{p} - (\hat{p} \cdot \hat{n})\hat{n}\right]$$

$$w = \frac{1}{\sin \theta_1} \left[\hat{p} + \hat{n} \cos \theta_1\right] \tag{B-33}$$

Substituting (B-33) into (B-31) yields

$$\hat{q} = \hat{n} \cos \theta_2 + \frac{\sin \theta_2}{\sin \theta_1} \left[\hat{p} + \hat{n} \cos \theta_1\right]$$

$$= \hat{n} \left[\frac{\cos \theta_1}{n_2} - \cos \theta_2\right] + \frac{\hat{p}}{n_2} \tag{B-34}$$

Note that

$$\cos \theta_1 = -\hat{n} \cdot \hat{p} \tag{B-35}$$

$$\cos \theta_2 = \sqrt{1 - \sin \theta_2} \tag{B-36}$$

$$\sin \theta_2 = \frac{\sin \theta_1}{n_2} = \frac{-1}{n_2} \left|\hat{n} \times \hat{p}\right| \tag{B-37}$$

$\hat{q}$ can then be calculated by combination of Equations (B-34) through (B-37).

The refracted rays can be expressed as:

$$\vec{Q}_1 = \vec{p}_{1i} + \hat{q}_1\, t_1 \tag{B-38}$$

$$\vec{Q}_2 = \vec{p}_{2i} + \hat{q}_2\, t_2 \tag{B-39}$$

where t_1 and t_2 are the length of the rays.

The next step is to find the value of t_1^* and t_2^* for which the distance D between the two rays is a minimum. The distance D is calculated as:

$$D = \sqrt{(\vec{Q}_1 - \vec{Q}_2) \cdot (\vec{Q}_1 - \vec{Q}_2)} \tag{B-40}$$

Substituting Equations (B-38) and (B-39) yields:

$$D = \sqrt{(\vec{p}_{1i} + \hat{q}_1 t_1 - \vec{p}_{2i} - \hat{q}_2 t_2) \cdot (\vec{p}_{1i} + \hat{q}_1 t_1 - \vec{p}_{2i} - \hat{q}_2 t_2)} \quad \text{(B-41)}$$

Differentiating Equation (B-41) with respect to t_1 and t_2 yields:

$$\frac{\partial D}{\partial t_1} = \hat{q}_1 \cdot (\vec{p}_{1i} + \hat{q}_1 t_1 - \vec{p}_{2i} - \hat{q}_2 t_2) \quad \text{(B-42)}$$

$$\frac{\partial D}{\partial t_2} = -\hat{q}_2 \cdot (\vec{p}_{1i} + \hat{q}_1 t_1 - \vec{p}_{2i} - \hat{q}_2 t_2) \quad \text{(B-43)}$$

Letting the derivatives equal zero gives two equations with two unknowns, t_1^* and t_2^*:

$$(\hat{q}_1 \cdot \hat{q}_1) t_1^* - (\hat{q}_1 \cdot \hat{q}_2) t_2^* = \hat{q}_1 \cdot (\vec{p}_{1i} - \vec{p}_{2i}) \quad \text{(B-44)}$$

$$-(\hat{q}_1 \cdot \hat{q}_2) t_1^* + (\hat{q}_2 \cdot \hat{q}_2) t_2^* = \hat{q}_2 \cdot (\vec{p}_{1i} - \vec{p}_{2i}) \quad \text{(B-45)}$$

Letting:

$$(\hat{q}_1 \cdot \hat{q}_1) = a_1 \quad \text{(B-46)}$$

$$-(\hat{q}_1 \cdot \hat{q}_2) = a_2 \quad \text{(B-47)}$$

$$(\hat{q}_2 \cdot \hat{q}_2) = a_3 \quad \text{(B-48)}$$

$$\hat{q}_1 \cdot (\vec{p}_{1i} - \vec{p}_{2i}) = b_1 \quad \text{(B-49)}$$

$$\hat{q}_2 \cdot (\vec{p}_{1i} - \vec{p}_{2i}) = b_2 \ , \quad \text{(B-50)}$$

we can write:

$$a_1 t_1^* + a_2 t_2^* = b_1 \quad \text{(B-51)}$$

$$a_2 t_1^* + a_3 t_2^* = b_2 \quad \text{(B-52)}$$

Solving these two equations gives values for t_1^* and t_2^*:

$$t_1^* = \frac{b_1 a_3 - b_2 a_2}{a_1 a_3 - (a_2)^2} \quad \text{(B-53)}$$

and

$$t_2^* = \frac{b_2 a_1 - b_1 a_2}{a_1 a_3 - (a_2)^2} \quad \text{(B-54)}$$

Substituting the values of t_1^* and t_2^* into Equations (B-38) and (B-39) yields the value of the two points of closest approach $\vec{Q}_1^*$ and $\vec{Q}_2^*$ and the position of the particle in the liquid column is:

$$(X,Y,Z) = \frac{1}{2}(\vec{Q}_1^* + \vec{Q}_2^*) \tag{B-55}$$

where $\vec{Q}_1^*$ and $\vec{Q}_2^*$ are expressed in terms of their object coordinate system.

The particle positions are also calculated in cylindrical coordinates:

$$r = [x^2 + y^2]^{1/2} \tag{B-56}$$

and

$$\theta = \tan^{-1}\frac{y}{x} \quad . \tag{B-57}$$

ACCURACY

To calculate the uncertainty in the results X, Y, Z, r, and θ, we express the results as a function of the independent input variables x_1, x_2, z_1, and z_2:

$$X = f(x_1, x_2) \tag{B-58}$$

$$Y = f(x_1, x_2) \tag{B-59}$$

$$Z = f(z_1, z_2) \tag{B-60}$$

$$r = f(x_1, x_2) \tag{B-61}$$

$$\theta = f(x_1, x_2) \tag{B-62}$$

The uncertainty intervals ΔX, ΔY, ΔZ, Δr and $\Delta\theta$ are calculated by the following expressions:

$$\Delta X = \left[\left(\frac{\partial x}{\partial x_1}\,\delta x_1\right)^2 + \left(\frac{\partial x}{\partial x_2}\,\delta x_2\right)^2\right]^{1/2} \tag{B-63}$$

$$\Delta Y = \left[\left(\frac{\partial y}{\partial x_1}\,\delta x_1\right)^2 + \left(\frac{\partial y}{\partial x_2}\,\delta x_2\right)^2\right]^{1/2} \tag{B-64}$$

$$\Delta Z = \left[\left(\frac{\partial z}{\partial z_1}\,\delta z_1\right)^2 + \left(\frac{\partial z}{\partial z_2}\,\delta z_1\right)^2\right]^{1/2} \tag{B-65}$$

$$\Delta r = \left[\left(\frac{\partial r}{\partial x_1}\,\delta x_1\right)^2 + \left(\frac{\partial r}{\partial x_2}\,\delta x_2\right)^2\right]^{1/2} \qquad \text{(B-66)}$$

$$\Delta \theta = \left[\left(\frac{\partial \theta}{\partial x_1}\,\delta x_1\right)^2 + \left(\frac{\partial \theta}{\partial x_2}\,\delta x_2\right)^2\right]^{1/2} \qquad \text{(B-67)}$$

Equations (B-63) through (B-67) were solved numerically using the computer program to calculate the results, while varying each of the four input variables by a differential amount equal to 4μm, which amount corresponds to the reproducibility of the measurement of a point on a negative using the toolmaker's microscope. The results of applying this method to the measurement of velocities in a case of a column rotating in isorotation is presented in Table B-1.

TABLE B-1

RESULTS OF ERROR ANALYSIS OF SELECTED PARTICLES,
BASED ON A VALUE OF THE MAXIMUM UNCERTAINTY
IN THE POSITION ON THE NEGATIVES OF ± .00038 CM

Particle	ΔX (cm)	ΔY (cm)	ΔZ (cm)	Δr (cm)	$\Delta\theta$ (Deg)
1-1	.0002	.0009	.0003	.0008	.19
3-1	.0003	.0017	.0003	.0017	.13
4-4	.0003	.0017	.0003	.0016	.22
5-4	.0004	.0021	.0003	.0020	.20
6-1	.0004	.0022	.0003	.0022	.10
Mean	.0003	.0017	.0003	.0017	.17

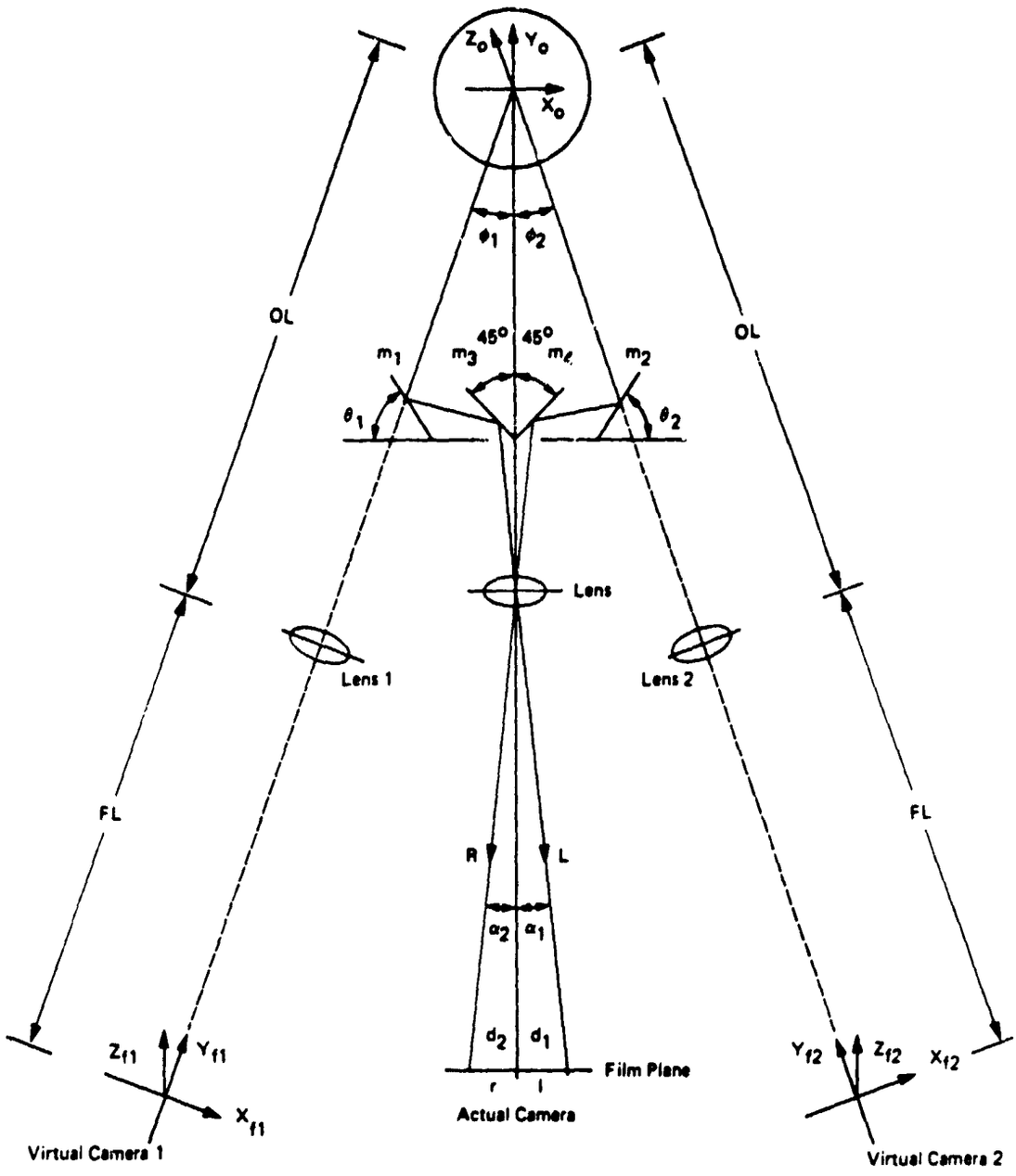

FIGURE B-1 SCHEMATIC DIAGRAM OF STEREOPTICAL PHOTOGRAPHIC SYSTEM